Argonne National Laboratory

REACTOR DEVELOPMENT PROGRAM
PROGRESS REPORT

December 1970

ARGONNE NATIONAL LABORATORY
9700 South Cass Avenue
Argonne, Illinois 60439

REACTOR DEVELOPMENT PROGRAM
PROGRESS REPORT

December 1970

Robert B. Duffield, Laboratory Director
Robert V. Laney, Associate Laboratory Director

Division	Director
Applied Physics	R. Avery
Chemical Engineering	R. C. Vogel
EBR-II Project	M. Levenson
Engineering and Technology	S. A. Davis
Materials Science	P. G. Shewmon
Reactor Analysis and Safety	W. R. Simmons

Report coordinated by
M. Weber and V. G. Trice, Jr.

Issued January 19, 1971

FOREWORD

The Reactor Development Program Progress Report describes current activities, technical progress, and technical problems in the program at Argonne National Laboratory sponsored by the USAEC Division of Reactor Development and Technology. Organized in accordance with the AEC's budget and reporting classifications, the report is published monthly. Not all projects are reported every month, but a running account of each project is maintained in the series of reports.

The last six reports
in this series are:

June 1970	ANL-7705
July 1970	ANL-7726
August 1970	ANL-7737
September 1970	ANL-7742
October 1970	ANL-7753
November 1970	ANL-7758

REACTOR DEVELOPMENT PROGRAM

Highlights of Project Activities for December 1970

EBR-II

(The reactor has been shut down since November 14, 1970, to carry out the annual program of reactor maintenance and modifications, and to define the precise cause of the noise in the intermediate heat exchanger and take corrective action.)

Interim postirradiation examination of element BF-11 after a calculated total burnup of 4.38 at. % showed no evidence of cladding fracture, even though appreciable diametral strain had occurred. This element is the test element in the experiment in Subassembly X078 on limitations on cladding for driver fuel. The element has been reassembled for further irradiation.

ZPR-3

A series of three critical configurations, Assemblies 63A, B, and C, has been constructed in ZPR-3 in support of the EBR-II program. All were alike in reflector and blanket, the principal variation being in the relative disposition of the simulated 37-pin and 19-pin mixed-oxide driver elements. Characterization included measurements of reaction rate, neutron spectrum, and gamma-ray intensity distribution.

Following these measurements, ZPR-3 was shut down, to be placed in standby, on December 15. The facility thus completed more than 15 years of fast-reactor research involving over 8300 startups.

ZPR-6

Using four thin-walled flow counters containing thin deposits of the fissionable isotopes, simultaneous counting procedures yielded the fission ratios of ^{238}U, ^{235}U, and ^{240}Pu relative to ^{239}Pu. The measurements were made in Assembly 7, the large plutonium reference assembly for the Demonstration Reactor Benchmark Program.

ZPR-9

Experimental measurements of shutdown margin in the range from \$1 to \$30 subcritical have been carried out in Assembly 26, the FTR-3 reactor. To this end, concurrent measurement by several laboratories used inverse kinetics, source multiplication, neutron-noise frequency analysis, asymmetric source, and polarity spectral-analysis techniques. Results are being analyzed.

With the completion of the FTR-3 program, the reactor was unloaded and preparations made for assembling the FTR Engineering Mockup Critical (EMC) in ZPR-9.

ZPPR

ENDF/B data and a Monte Carlo code were used in a computer run involving 10,000 neutron histories to evaluate the neutron multiplication factor in the two-zoned Assembly 2 of the Demonstration Reactor Benchmark Program. Averaging 52.5 collisions per history, the calculation had a probable error in k of 0.0067.

Comparison of calculated and measured fission ratios for the current ZPPR loading indicate the possibility of a consistent error in the ^{235}U fission cross section.

Preanalysis in anticipation of future Assembly 2 experiments has been carried out in the areas of fission-rate calculation, establishment of recommended kinetics parameters, and mixed-oxide pin substitutions.

TABLE OF CONTENTS

TABLE OF CONTENTS

TABLE OF CONTENTS

vii

Listing of the
ANL Reactor Development Program Projects
in 189a Order

189a No.	Reported This Month	189a Title	RDT Branch
02-005		Oxide Fuel Studies	RT-FM
02-009		General Fast Reactor Physics	RT-PH
02-010	x	Fast Critical Experiments--Theoretical Support--Idaho	RT-PH
02-011		Fast Critical Experiments--Experimental Support--Idaho	RT-PH
02-012		Fast Critical Experiments--Industrial Appointments	RT-PH
02-013	x	Fast Critical Experiments--Experimental Support--Illinois	RT-PH
02-015		Planning and Evaluation of FFTF Critical Assembly Experiments	RT-PH
02-019		Production of Materials for ZPR Experiments	RE-FE
02-020		ZPR Materials Procurement	RE-FE
02-021	x	On-line Monitoring and Sampling for Sodium Systems	RT-CC
02-024		Instrumentation Development for Instrumented Subassembly	PE-IC
02-025	x	FFTF Instrumentation Development	PE-IC
02-026	x	Core Component Test Loop (CCTL)	RE-CD
02-035		LMFBR Program Office	PM-LP
02-036		EBR-II Program Management	PM-EB
02-038		System Design Descriptions	PE-LS
02-045		Equipment--Fuel Related	RE-FH
02-046		New Subassemblies and Experimental Support	RE-CD
02-048		Instrumented Subassemblies	RE-CD
02-051		Coolant Chemistry	RT-CC
02-053		Experimental Irradiation and Testing	RT-FM
02-061		Nuclear Instrument Test Facility	PE-IC
02-063		Materials-Coolant Compatibility	RT-CC
02-065		Procedures, Planning, and Scheduling	PE-LS
02-068		Systems Engineering	PE-LS
02-073		Fuel and Hardware Procurement	RE-FE
02-075		Reactor Operations	PE-LS
02-076		Fuel Cycle Facility Operations	RE-FE
02-079		Studies and Evaluations for RDT Program Analysis Branch	PA-PA
02-081		Theoretical Reactor Physics	RT-PH
02-082	x	Cross-section Measurements	RT-PH

189a No.	Reported This Month	189a Title	RDT Branch
02-083		Burnup Analysis and Fission Yields for Fast Reactors	RT-PH
02-084		Determination of Nuclear Constants	RT-PH
02-085		Reactor Code Center	RT-PH
02-086		Behavior of Reactor Materials	RT-FM
02-087	x	Chemistry of Irradiated Fuel Materials	RT-FM
02-088		Thermodynamics of Carbide Fuel	RT-FM
02-091	x	In-reactor Creep Studies	RT-FM
02-092	x	Nondestructive Testing Research and Development	RT-FM
02-094	x	High-temperature Properties of Ceramic Fuels	RT-FM
02-096	x	Instrumentation and Control	RT-ST
02-097	x	Heat Transfer and Fluid Flow	RT-ST
02-099	x	Engineering Mechanics	RT-ST
02-112	x	Accident Analysis and Safety Evaluation	NS-FS
02-114	x	Coolant Dynamics	NS-FS
02-115		Core Structural Safety	NS-FS
02-116		Fuel-element Failure Propagation	NS-FS
02-117	x	Fuel Dynamics Studies in TREAT	NS-FS
02-119		High-temperature Physical Properties and Equation-of-state of Reactor Materials	NS-FS
02-120		Fast Reactor Safety Test Facility Study	NS-FS
02-121		1000-MWe Safety Analysis Study Subcontracts	NS-FS
02-122	x	TREAT Operations	NS-RD
02-126		Reactor System and Containment Structural Dynamic Response	NS-FS
02-131		EBR-II In-core Instrument Test Facility	PE-IC
02-133		NDT Measurement of Effective Cold Work in Cladding Tubes	RT-FM
02-134	x	Fast Critical Experiments--Theoretical Support--Illinois	RT-PH
02-137	x	Nonmetallic Impurity Interactions in Sodium-Metal Systems	RT-CC
02-138		Neutron-detector Channel Development	PE-IC
02-144	x	Reactor Analysis, Testing, and Methods Development	RE-CD
02-145		Metal Driver Fuel Development and Application	RE-FE
02-148	x	Operation with Failed Fuel	RE-CD
02-150		Hot Fuel Examination Facilities	PE-FH
02-151	x	Characterization of Irradiation Environment	RE-CD
02-156	x	Sodium Impurity Analysis and Control	RT-CC

189a No.	Reported This Month	189a Title	RDT Branch
02-157	x	LMFBR Fuel Materials Preparation--U/Pu Nitrates to Oxides	RT-FR
02-158		LMFBR Fuel Fabrication--Analyses and Continuous Processing	RT-FR
02-159	x	LMFBR Reprocessing--Plutonium Isolation	RT-FR
02-162		Thermophysical Properties of Reactor Fuels	RT-FR
02-164	x	Fuel-Coolant Interactions	NS-FS
02-165		Post-accident Heat Removal	NS-FS
02-166		Thermal-plume Dispersion Studies	NS-EE
02-173	x	Molten Metal Decladding of LMFBR Fuels	RT-FR
02-175	x	Physical and Chemical Studies--Molten Fuel, Cladding, and Coolant	RT-FR
02-178		ZPR-6 and -9 Operations and Maintenance	RT-PH
02-179	x	Fast Critical Facilities Experiments and Evaluation-- Illinois	RT-PH
02-180		ZPPR and ZPR-3 Operations and Maintenance	RT-PH
02-181	x	Fast Critical Facilities Experiments and Evaluation-- Idaho	RT-PH
02-182		LMFBR Fuel Management Studies	RT-FR
02-184		Mass/Energy Balance of the Great Lakes	NS-ES
02-185		Lake Circulation Model Development	NS-EE
02-186		1000-MWe Contract Management, Technical Review, and Evaluation	PE-LM
02-191		Disposal of EBWR Fuel	RD-AB
02-194		Surveillance and Failure Evaluation of Experimental Fuel Irradiations	RT-FM
02-195		Scram System Study	PE-LS
02-197		TREAT Improvement Studies	PM-EB
02-200		Conceptual Design Study of FFTF Vessel Head-cavity System	RE-CD
02-201		Utilization of EBR-II in the Development of Sodium Technology	RT-CC
02-509	x	Sodium Chemistry and Radioactive Contaminant Behavior	RT-CC
02-526	x	In-pile Stainless Steel Swelling and Mechanical Behavior	RT-FM
02-528		Plant Dynamics and Control Analysis	PE-IC
02-530		Operation of Data Acquisition System (DAS)	PE-IC

I. LIQUID METAL FAST BREEDER REACTORS

A. Fuel Development

1. Fuel Cladding and Structure

a. In-pile Stainless Steel Swelling and Mechanical Behavior (189a 02-526)

(i) Neutron Simulation Studies Using 4-MeV Dynamitron (A. Taylor)

Last Reported: ANL-7758, pp. 1-4 (Nov 1970).

Four samples of annealed Type 304 stainless steel were irradiated at approximately 500°C under the conditions specified in Table I.A.1. The $^{58}Ni^+$ irradiations constitute the first set of irradiations performed at ANL using the heavy-ion source in the Dynamitron. While operating experience is being gained, the voltage of the machine will be raised progressively toward 4.0 MV.

TABLE I.A.1. Ion Irradiations of Type 304 Stainless Steel Specimens

Sample Number	Ion	Energy, MeV	Mean Ion Flux, $cm^{-2} sec^{-1}$	Ion Fluence, cm^{-2}
1120-1	$^1H^+$	1.27	1×10^{15}	1×10^{19}
1201-1	$^{58}Ni^+$	3.0	8.6×10^{12}	$\sim 3.5 \times 10^{16}$
1201-2	$^{58}Ni^+$	3.0	4×10^{12}	5×10^{16}
1202-1	^{58}Ni	3.5	2.2×10^{12}	4.5×10^{16}

B. Physics Development

1. Theoretical Reactor Physics

a. Fast Critical Experiments--Theoretical Support--Idaho (189a 02-010)

(i) Supplementary Analytical Interpretation of Integral Data (R. G. Palmer)

Last Reported: ANL-7758, pp. 13-15 (Nov 1970).

(a) Preanalysis of ZPPR Assembly 2 (A. P. Olson and R. G. Palmer)

(1) Central Fission Ratios. Central fission ratios for uranium and plutonium isotopes have been calculated from 2-D diffusion theory in R-Z geometry for ZPPR Assembly 2. (See Progress Report for July 1970, ANL-7726, pp. 11-16.) Since the fission-ratio experiments will be performed in a radial-traverse access hole located at Z = 8.89 cm, the calculated fission ratios shown in Table I.B.1 were obtained for a central point at this axial position. Neutron cross sections were obtained from the 27-group ZPPR Assembly 2 Cross Section Library. (See Progress Report for April-May 1970, ANL-7688, p. 7.) Energy self-shielded, spatially weighted cross sections were used in the flux calculations. Foil cross sections were energy self-shielded at infinite dilution for ^{233}U, ^{234}U, and ^{236}U and at homogeneous atom density for ^{235}U, ^{238}U, ^{239}Pu, ^{240}Pu, and ^{241}Pu.

TABLE I.B.1. Central Fission Ratios in ZPPR Assembly 2

| Isotope | Fission Ratio | |
	Relative to U-235	Relative to Pu-239
U-233	1.384	1.606
U-234	0.1309	0.1520
U-235	1.000	1.161
U-236	0.04043	0.04692
U-238	0.01866	0.02166
Pu-239	0.8616	1.000
Pu-240	0.1584	0.1839
Pu-241	1.298	1.506

(2) Oxide Pin Zones. It is planned to make zone substitutions of mixed oxide pins in sodium-filled calandria for the present plate-loaded drawers in ZPPR Assembly 2 in order to study the effects of geometry on the measured data. Some one-dimensional zone calculations have been made in cylindrical geometry using the appropriate MC^2-CALHET cell weighted 27-group cross sections for the plates and pins. Central pin zones of 21, 37, and 69 drawers (equivalent circular radii of 14.58, 19.34, and 26.43 cm) extending the whole core length were calculated using 1-D diffusion-theory and perturbation-theory ARC modules. A single axial buckling value was used for simulating the axial leakage. The results are summarized in Table I.B.2, the base case being the normal plate core. The results apply only to the inner-core region of the two-zone ZPPR Assembly 2.

TABLE I.B.2. 1-D Calculations for Mixed-oxide Pin Zones in ZPPR Assembly 2

	Reference Core	14-cm Pin Zone	19-cm Pin Zone	26-cm Pin Zone
k_{eff}	0.9871	0.9866	0.9863	0.9855
Denominator of perturbation integral (in units of 10^{16})	6.3552	6.4463	6.4743	6.5051
Central worth of ^{239}Pu, 10^{-1} $(\Delta k/k)/kg$	0.4453	0.4323	0.4282	0.4236
Central worth of ^{23}Na, 10^{-2} $(\Delta k/k)/kg$	-0.1207	-0.1179	-0.1172	-0.1164
Central worth of ^{238}U, 10^{-2} $(\Delta k/k)/kg$	-0.2843	-0.2985	-0.2951	-0.2914
Central value of $\bar{\sigma}_f$ ^{239}Pu, barns	1.8720	1.8994	1.8781	1.8758
Central value of $\bar{\sigma}_f$ ^{238}U	0.0484	0.04248	0.04252	0.04255
Central value of $\bar{\sigma}_c$ ^{238}U	0.3390	0.3468	0.3489	0.3463

Reasonable spectral equilibration at the center of the 19.34-cm-radius pin zone is indicated by the central cross sections. The close agreement between the worths in the plate and pin zones is surprising, particularly for the sodium worth which is sensitive to spectral differences, but further inspection of the real and adjoint spectra shows cancellation of positive and negative differences over the whole energy range.

(3) <u>Kinetics Parameters Calculations</u>. A series of calculations of kinetics parameters in ZPPR Assembly 2 has been performed to establish recommended values for use in reduction of experimental data. Another rationale for this series was to compare the results obtained from 1-D and 2-D diffusion codes with those from a 2-D transport code.

Table I.B.3 summarizes the results from six calculational methods. Further details about these calculations are:

Column 1   The cross sections supplied to MACH 1 were homogeneously self-shielded for a composition similar to the inner-core zone of ZPPR-2.

Columns 2-4   Neutron cross sections came from the Cross Section Library for ZPPR Assembly 2. CALHET-weighted, heterogeneously self-shielded cross sections were used. The mesh spacings, region boundaries, and atom densities were identical in these three runs. (See Progress Report for April-May 1970, ANL-7688, pp. 20-27.)

The DOT 2-D transport calculations were run in the S_4 approximation.

Columns 5 and 6   Neutron cross sections were as in columns 2-4. The number of mesh points was unchanged (19 in Z-direction, 30 in R-direction), but the axial mesh spacings were

TABLE I.B.3. Descriptions of Calculational Models, with Calculated Kinetics Parameters for ZPPR-2

Reactor Configuration	2566 ℓ Core 50/50	2372 ℓ Core 50/50, Loading 74 (to June 8/70) 1/4" Na in I.C.			2376 ℓ Core 50/50, Loading 77 (from June 22/70) 1/2" Na in I.C.	
Flux Code	MACH 1 (1D)	ARCSTP007 (2D)	ARCSTP007 (2D)	DOT (2D Transport)	ARCSTP007 (2D)	DOT (2D Transport)
β Code	MACH 1	PERT V	ARCSTP007	ARCSTP007	ARCSTP007	ARCSTP007
ℓ_p, 10^{-7} sec	4.9500	5.5561	5.4671	5.4553	5.5963	5.5780
β	0.0031718	0.0032258	0.0032061	0.0031955	0.0031880	0.0031800
Ih per %Δk/k	1026.82	997.90	1010.61	1014.18 1015.14[a]	1012.58 1013.33[a]	1014.96 1015.67[a]
β x Ih per %Δk/k	3.257	3.219	3.240	3.241 3.243[a]	3.228 3.230[a]	3.228 3.230[a]
β Data	Keepin, Fast Fission Tables 4-7,4-14	Keepin, β_i/β, Table 4-7[1](Fast) n/F, Table 4-14 (Thermal)	Keepin, Fast Fission Table 4-7			
λ Data	Keepin, Fast Fission Table 4-7	Keepin, Fast Fission, 24 λ_i Table 4-7	6 λ_i	6 λ_i 24 λ_i, Table 4-7		

[a]Uses 24 λ_i-values, Keepin Table 4-7 (Fast Fission).

changed to correspond to radial-traverse access holes, and the radial mesh spacings were made more uniform. The geometry and atom densities used in this pair of calculations correspond to the current loading of Assembly 2. (See Progress Report for July 1970, ANL-7726, pp. 11-16.)

The ARC System calculations of β_{eff} use the same set of six λ_i's for each fissile isotope in the reactor, a restriction imposed by computer storage limitations. (The Idaho IBM/360 does not have a drum-storage device.) The values of β_{eff} and prompt-neutron lifetime do not depend upon the values of λ_i and are thus not affected by this approximation. However, the Ih per %Δk/k conversion factor is dependent on the decay constants. Consequently, an auxiliary program has been written for the SEL-840MP which uses the β_i and ℓ_p values from ARCSTP007, along with the appropriate decay constants for each isotope as obtained from Keepin,* Table 4-7. The difference in the conversion factor is small, as seen in Table I.B.3.

The differences between the various sets of effective parameters are obviously small and constitute a negligible contribution to the overall measurement uncertainty. The two best sets of results are those in columns 4 and 6 of Table I.B.3 (from 2-D transport fluxes), using 24 λ_i values. Table I.B.4 contains recommended values of the kinetics parameters, some of which come from column 6 of Table I.B.3, to be used in all kinetics calculations for either version of Assembly 2. For completeness, Table I.B.5 contains results from column 4 of Table I.B.3.

(ii) ZPR Heterogeneity Methods Development (R. G. Palmer)

Last Reported: ANL-7758, p. 15 (Nov 1970).

(a) VIM-I Monte Carlo Code (F. L. Fillmore)

A computer run having 10,000 neutron histories was made for the VIM-I heterogeneous model of the ZPPR-2 critical assembly 50/50 reference core. The Cross Section Library is based on the ENDF/B Version I (1968) data. Some of the results are presented in Table I.B.6.

The convergence on k obtained with 10,000 histories is not as good as desired. About 40,000 histories should give a probable error of about 0.003, which is more acceptable. However, since the Cross Section Library that was used does not include the effect of self-shielding

---

*G. R. Keepin, Physics of Nuclear Kinetics, Addison-Wesley (1965).

TABLE I.B.4. Recommended Effective Kinetics Parameters for ZPPR Assembly 2

Group, i	λ_i	$(\beta_{eff})_i$	Isotope
1	0.0132	1.8796×10^{-5}	
2	0.0321	2.0396×10^{-4}	
3	0.139	2.3809×10^{-4}	^{238}U
4	0.358	5.8014×10^{-4}	
5	1.41	3.3633×10^{-4}	
6	4.02	1.1211×10^{-4}	
7	0.0127	2.6055×10^{-6}	
8	0.0317	1.5266×10^{-5}	
9	0.115	1.3236×10^{-5}	^{235}U
10	0.311	2.9242×10^{-5}	
11	1.40	9.1818×10^{-6}	
12	3.87	1.8712×10^{-6}	
13	0.0129	1.8473×10^{-6}	
14	0.0313	1.6251×10^{-5}	
15	0.135	1.0931×10^{-5}	^{240}Pu
16	0.333	2.1581×10^{-5}	
17	1.36	8.1527×10^{-6}	
18	4.04	1.6442×10^{-6}	
19	0.0129	5.7489×10^{-5}	^{239}Pu
20	0.0311	4.3649×10^{-4}	
21	0.134	3.3328×10^{-4}	plus
22	0.331	5.1510×10^{-4}	
23	1.26	1.6175×10^{-4}	^{241}Pu
24	3.21	5.4745×10^{-5}	

Total β_{eff} = 0.003180

Prompt lifetime, $\ell_p = 5.578 \times 10^{-7}$

Inhours per %$\Delta k/k$ = 1015.7

TABLE I.B.5. Calculated Effective Kinetics Parameters for ZPPR Assembly 2 50/50 Version[a]

Group, i	λ_i	$(\beta_{eff})_i$	Isotope
1	0.0132	0.19150×10^{-4}	
2	0.0321	0.20795×10^{-3}	
3	0.139	0.24269×10^{-3}	^{238}U
4	0.358	0.59153×10^{-3}	
5	1.41	0.34293×10^{-3}	
6	4.02	0.11431×10^{-3}	
7	0.0127	0.25829×10^{-5}	
8	0.0317	0.15104×10^{-4}	
9	0.115	0.13127×10^{-4}	^{235}U
10	0.311	0.29010×10^{-4}	
11	1.40	0.91088×10^{-5}	
12	3.87	0.18563×10^{-5}	
13	0.0129	0.18994×10^{-5}	
14	0.0313	0.16718×10^{-4}	
15	0.135	0.11244×10^{-4}	^{240}Pu
16	0.333	0.22204×10^{-4}	
17	1.36	0.83881×10^{-5}	
18	4.04	0.16917×10^{-5}	
19	0.0129	0.56908×10^{-4}	
20	0.0311	0.43233×10^{-3}	^{239}Pu
21	0.134	0.33004×10^{-3}	
22	0.331	0.51023×10^{-3}	plus
23	1.26	0.16022×10^{-3}	^{241}Pu
24	3.21	0.54228×10^{-4}	

Total β_{eff} = 0.0031955

Prompt lifetime, $\ell_p = 5.45528 \times 10^{-7}$

Inhours per %$\Delta k/k$ = 1015.14

[a] Data applicable to runs up to and including Run 143, June 8, 1970.

TABLE I.B.6. ZPPR Results Using
ENDF/B Version I Data

Total number of histories	10,000
k	1.0002
Probable error	±0.0067
Running time (CPU), min	43.2
Collisions per history	52.5
Computer core requirement	550 K

on the unresolved resonances, it was decided that making a longer run at this time was not appropriate. The effect of self-shielding the unresolved resonances should lead to an increase in k of about 0.5%, and the probable error obtained in the present run is close to this value.

A longer run will be made when the VIM-I Library based on the ENDF/B Version II data is received from L. B. Levitt of Atomics International. This library will include unresolved resonance self-shielding.

b. Fast Critical Experiments--Theoretical Support--Illinois (189a 02-134)

(i) Supplementary Analytical Interpretation of Integral Data (C. E. Till)

Last Reported: ANL-7737, pp. 11-12 (Aug 1970).

(a) Analysis of Doppler Measurements for ^{238}U in ZPR-3 Assembly 51 (P. H. Kier)

The UO_2 small-sample Doppler measurements (see Progress Report for June 1968, ANL-7460, pp. 20-21) in ZPR-3 Assembly 51 have been analyzed. The calculated and experimental results are compared in Table I.B.7. P-16 is the central matrix location, P-10 is a matrix location that is in the core and adjacent to the inner reflector, and P-12 is a matrix location that is in the core and between P-10 and P-16.

TABLE I.B.7. Comparison of Measured and Calculated Doppler Effect
for the UO_2 Sample in ZPR-3 Assembly 51,
Reactivity in Ih

Matrix Location	Temperature Change, °K	Experimental ρ	Calculated[a] ρ	C/E
P-16	293→500	-0.1315 ± 0.0053	-0.1070	0.814
	293→1100	-0.3857 ± 0.0054	-0.2786	0.722
P-12	293→500	-0.0846 ± 0.0058	-0.0786	0.929
	293→1100	-0.2258 ± 0.0057	-0.2076	0.919
P-10	293→500	-0.0728 ± 0.0044	-0.0903	1.240
	293→1100	-0.1989 ± 0.0037	-0.2478	1.245

[a]Period/reactivity conversion factor = 1104 Ih/%ρ.

(See Progress Report for January 1968, ANL-7419, pp. 10-14.) Table I.B.7 indicates that there are appreciable discrepancies between the measured and calculated Doppler effects.

The Doppler effect for the sample in the central matrix location, P-16, was obtained from a 29-group, two-dimensional perturbation calculation in R-Z geometry. In the diffusion calculations, from which the real and adjoint flux distributions were obtained, the reactor was represented with the sample, oscillator drawer, and nickel filter as separate regions. In obtaining the period/reactivity conversion factor of 1104 Ih/%ρ, the two-dimensional real and adjoint flux distributions were used.

In the creation of the 29-group cross-section set, several prescriptions were used to generate isotopic cross sections. Cross sections for uranium in the sample at the three temperatures were from MC^2 problems* with pin geometry. In these MC^2 runs, the fine-group fluxes from the MC^2 run used to derive the cross sections for the core were used to collapse to the broad-group cross sections. Thus the uranium cross sections in the sample have resonance self-shielding and were based on the assumption that the gross spectrum was identical with that in the core. For the core, the cross sections derived from an MC^2 run were modified by an auxiliary code to account for resonance self-shielding and by plate disadvantage factors obtained from S_{16} transport calculations. Cross sections for the reflector zones were obtained from separate homogeneous MC^2 runs in which there was assumed to be no leakage of neutrons.

To obtain the Doppler worths of the sample for the off-center matrix locations, P-10 and P-12, it was assumed that the change in cross section of uranium in the sample with temperature and the relative flux perturbation in the vicinity of the oscillator drawer are independent of the matrix position at which the measurement took place. Then the relative magnitude of the Doppler worth of the sample at the three locations is dependent upon the real and the adjoint flux distributions in the assembly when it is unperturbed by the presence of the sample. Hence, the calculated Doppler effect for the sample at the offcenter matrix locations were obtained from the Doppler effect at matrix position P-16 and the relative magnitudes of the Doppler effect as obtained from one-dimensional perturbation calculations that used fluxes for the circularized assembly whose transverse height was adjusted to achieve criticality.

(ii) ZPR Heterogeneity Method Development

Not previously reported.

---

*B. J. Toppel, A. L. Rago, and D. M. O'Shea, MC^2, A Code to Calculate Multigroup Cross Sections, ANL-7318 (June 1967).

(a) MC^2-2 Support (B. A. Zolotar)

To provide a convenient and reliable method of obtaining a set of group cross sections for use in the analysis of ZPR lattices, a set of heterogeneity algorithm recommendations has been formulated for use in the new MC^2-2 Code.

In the resonance region, the plate absorption cross section for ZPR cells will be calculated by multiplate equivalence theory basing the Dancoff factor on the two-sided E_3 formulation of Meneghetti.[*] The calculation will be designed to allow the user to perform many different resonance self-shielding calculations in one MC^2-2 run to cover each absorber plate condition. For cases in which it would be deemed desirable to perform more accurate resonance calculations, the RABBLE[**] technique will be included as an optional module to be used in the resolved resonance range.

The code will include the capability to calculate the spatial flux distribution through the cell. Two alternatives will be available, the discrete-ordinate transport method and the Storrer-Khairallah integral-transport perturbation method.[†] Fluxes from either method will be used in a flux-weighting procedure to obtain cell-homogenized cross sections.

2. Experimental Reactor Physics

a. Fast Critical Experiments--Experimental Support--Illinois (189a 02-013)

(i) Maintenance of Support Techniques and Facilities

Last Reported: ANL-7558, pp. 15-19 (Nov 1970).

(a) Measuring Reaction Rates in Heterogeneous Fast-reactor Cells (G. S. Stanford, C. E. Till, W. R. Robinson, and E. F. Bennett)

Measurements of the reaction rates in the cell constituents are among the more readily interpretable of the measurements made on fast critical assemblies. The information is directly related to the

---

[*]D. Meneghetti, "Calculational Studies of Sodium-void Reactivity Variations due to Thin Slab Heterogeneities in Fast Critical Assemblies," Proc. International Conference on Fast Critical Assemblies and Their Analysis, October 10-13, 1966, ANL-7320, pp. 377-386.

[**]P. H. Kier and A. A. Robba, RABBLE, A Program for Computation of Resonance Absorption in Multiregion Reactor Cells, ANL-7326 (Apr 1967).

[†]F. Storrer et al., Heterogeneity Calculations for Fast Reactors by a Perturbation Method, Nucl. Sci. Eng. 24, 153 (1966).

neutron balance and is valuable for diagnosing areas of uncertainty in cross sections and calculational methods. Although in reactor analysis the reaction rates generally enter as ratios, to determine those ratios the measurements of the individual reaction rates must usually be absolute. Since absolute measurements tend to be plagued by unsuspected systematic errors, agreement between independent methods is important.

To examine the status of various methods for measuring reaction rates in fast critical assemblies, several such methods were used in recent measurements on ZPR-3 and -9. The available methods fall into four general categories, which are (in order of decreasing spatial resolution): foils, solid-state track recorders (SSTR's), radiochemistry, and fission counters. Here in-cell methods for measuring fission rates in fissionable isotopes and capture rates in ^{238}U will be discussed.

The primary data from activated foils consist usually of relative counting rates, which must be reduced to an absolute basis by means of some form of calibration. Several independent calibration methods are available. Except for threshold reactions, there is the standard thermal-calibration technique, involving the irradiation in a thermal-neutron flux of foils similar to the ones irradiated in the fast assembly. Accuracies approaching ±1% can be obtained.

For the fission reactions, one can calibrate the foils by positioning some of them against the face of an absolute fission counter located somewhere in the fast assembly during the irradiation.

Relative capture rates in ^{238}U foils can be determined by counting the 100-keV X-ray gamma-ray coincidences resulting from the decay of ^{239}Np. (See R. Sher, Gamma-Gamma Coincidence Method for Measuring Resonance Escape Probability in U-238 Lattice, Nucl. Sci. Eng. 7, 479f (1960); also H. Seufert and D. Stegemann, A Method for Absolute Determination of ^{238}U Capture Rates in Fast Zero-Power Reactors, Nucl. Sci. Eng. 28, 277-285 (1967).) Calibration can be accomplished both by the thermal calibration technique, and by counting, along with the foils, a calibrated ^{243}Am source. At present, however, full application of the latter technique to thick foils has been prevented by the lack of an accurate correction for self-absorption of the 100-keV radiation by the foil.

The SSTR technique* is potentially useful for making absolute fission-rate measurements in heterogeneous reactor cells; its usefulness will increase when automatic track counting becomes available.**

*R. Gold, R. J. Armani, and J. H. Roberts, Absolute Fission Rate Measurements with Solid-State Track Recorders, Nucl. Sci. Eng. 34, 13-32 (1968).
**C. E. Cohn, R. Gold, and T. W. Pienias, A Computer-Controlled Microscope for Scanning Fission-Track Plates, Trans. Am. Nucl. Soc. 12(1), 68 (1969).

Radiochemical analysis[*] can be used to determine fission rates, and capture in ^{238}U, in rather large pieces of material, yielding volume-average results. Reproducibility is approximately ±3%.

Because of their size and construction, fission counters-- either solid-state or gas-ionization--are unsuitable for detecting intracell fine structure. However, they can provide absolute fission rates, and can indicate cell-averaging values if the geometry is suitable. Also, as mentioned above, they can be used for absolute calibration of fission foils.

Except for the SSTR and ^{243}Am techniques, which need some further development, agreement between the various methods has in general been satisfactory, when suitable precautions are taken. This is indicated in Table I.B.8, which gives results obtained in two heterogeneous assemblies.

TABLE I.B.8. Reaction-rate Ratios (per Atom) by Different Methods

| | Assembly 24 (Uranium Fuel) | | Assembly 55 (Plutonium Fuel) | | |
	c^{28}/f^{25}	f^{28}/f^{25}	c^{28}/f^{49}	f^{28}/f^{49}	f^{49}/f^{25}
Thermal Calibration	0.1325 ± 0.002	---	0.1415 ± 0.002	---	0.902 ± 0.02
Radiochemistry	0.1281 ± 0.005	0.01814 ± 0.0006	0.1394 ± 0.005	0.01939 ± 0.0006	---
Fission Chambers	---	0.01914 ± 0.0006	---	0.02047 ± 0.0006	0.909 ± 0.01
$\frac{^{238}U\ Radiochemistry}{^{239}U\ Fission\ Chamber}$	0.1310 ± 0.004	0.01831 ± 0.0006	---	---	---
$\frac{^{238}U\ Radiochemistry}{^{239}Pu\ Fission\ Chamber}$	---	---	0.1393 ± 0.004	0.01953 ± 0.0006	---

3. ZPR-6 and -9 Operations and Analysis

a. Fast Critical Facilities Experiments and Evaluation--Illinois (189a 02-179)

(i) Clean Critical Experiments (R. A. Lewis)

Last Reported: ANL-7758, pp. 19-20 (Nov 1970).

(a) Fission Ratios in ZPR-6 Assembly 7. Four thin-walled Kirn-type[**] fission-flow counters placed near the center of the core were used to measure fission rates in ^{239}Pu, ^{240}Pu, ^{235}U, and ^{238}U. Each

---

[*]R. J. Armani, "Absolute Determination of Fission Rates in U-235 and U-238 and Capture Rates in U-238 by Radiochemical Techniques," Proc. IAEA Symposium on Standardization of Radionuclides, Vienna, Austria, October 1966, IAEA, Vienna (1967), p. 613.

[**]F. S. Kirn, An Absolute Fission Counter, ANS Second Winter Meeting (1957).

counter was loaded in a regular fuel drawer in a 2-in. cavity 6 in. from the axial reactor midplane, so that the fission foil was located $7\frac{1}{8}$ in. from the drawer front (axial reactor midplane). The drawer location of each detector is given in Table I.B.9. All fission foils contained thin (~ 20-$\mu g/cm^2$) deposits of the fissioning isotope. The fission ratios obtained from several sets of simultaneous count rates are listed in Table I.B.9.

TABLE I.B.9. Fission Ratios Relative to ^{239}Pu in ZPR-6 Assembly 7

Detector Drawer Location				
Reactor Half[a]	Column	Row	Fission Foil in Counter	Fission Ratios,[b] per atom
M	19	24	^{239}Pu	1.0000
M	22	27	^{238}U	0.0215 ± 0.0002
M	25	27	^{240}Pu	0.1850 ± 0.0027
M	27	24	^{235}U	1.0474 ± 0.0227

[a] M denotes movable half.

[b] Fission ratios have been corrected for fission fragment low-energy spectrum cut-off, position relative to ^{239}Pu detector, and count rates due to contaminating fissioning isotopes on each foil.

The fission ratios have been corrected for the fission-fragment low-energy spectrum cutoff by using a flat extrapolation from the valley between the alpha and fission-fragment pulse-height distributions to the zero-energy channel. All detectors, except the ^{240}Pu detector, were located the same distance from the core center. A small correction factor ($\sim 1.0\%$) was computed for the ^{240}Pu fission rate with the 1-D diffusion code MACH-1 and the cross sections described in ZPR-TM-27.* The fission rates recorded for each foil were also corrected for counts from other fissioning isotopes present on the foil deposit. In every case, this correction was small ($< 1.0\%$), except for the ^{240}Pu foil, for which 8% of the fissions were due to isotopes other than ^{240}Pu. The weights of the fissioning isotopes present on each foil were determined by Armani** using an alpha-counting technique.

*J. E. Marshall, L. G. LeSage, and E. M. Bohn, Pre-Analysis of ZPR-6 Assembly 7, ZPR-TM-27 (1970).

**R. J. Armani, "Preparation of Pu-239 and Pu-240 Isotopes for Capture-to-Fission Measurements in the Experimental Boiling Water Reactor," Reactor Physics Division Annual Report: July 1, 1966 to June 30, 1967, ANL-7310, pp. 379-380 (Jan 1968).

The uncertainties in the fission ratios given in Table I.B.9 include, in order of importance, contributions from the uncertainties in weights of isotopes on the foils, count rates, and the fission fragment low-energy spectrum cutoff loss.

(ii) Mockup Critical Experiments (J. W. Daughtry)

(a) ZPR-9 Studies (R. B. Pond)

Last Reported: ANL-7753, pp. 14-17 (Oct 1970).

The shutdown margin experiments in Assembly 26, FTR-3, have been completed. The measurements ranged from approximately \$1.00 subcritical to \$30.00 subcritical. Concurrent measurements were made by ANL using inverse-kinetics, source-multiplication, and neutron-noise techniques; by ORNL using neutron-noise and asymmetric-source techniques; and by the University of Washington using polarity spectral analysis. The results of these measurements are currently being analyzed by the respective groups.

Assembly 26 is currently being unloaded as the FTR-3 experimental program is completed. Fuel unloading has been completed and nonfuel materials are presently being unloaded and cleaned in preparation for loading the FTR Engineering Mockup Critical (EMC) into ZPR-9.

4. ZPPR and ZPR-3 Operations and Analysis

a. Fast Critical Facilities Experiments and Evaluation--Idaho (189a 02-181)

(i) Clean Critical Experiments (P. I. Amundson)

Last Reported: ANL-7758, p. 23 (Nov 1970).

(a) ZPPR Assembly 2 (R. E. Kaiser)

The studies of the effects of different calculational procedures for the determination of β_{eff} have been completed, and a set of effective kinetics parameters has been chosen. (See Sect. I.B.1.a(i)(a)(1).) The differences between values obtained for the first 50/50 core and those obtained for the core as it exists currently were on the order of 0.1% or less for β_{eff} and Ih per %Δk/k, so that it was decided to use the same values in all data reduction on the 50/50 core. These values are ℓ_p = 5.578 x 10^{-7} sec, β_{eff} = 0.003180, and Ih per %Δk/k = 1015.7. All previous experiments using this data are currently being reanalyzed, and the results will be presented in subsequent reports.

Experimental determinations of fission ratios in the inner core have been completed, with the results shown in Table I.B.10. The measurements were made using foils of the respective isotopes placed back-to-back with a ^{235}U foil in a spherical chamber. The chamber was positioned 3 in. back from the interface, in approximately the same position that the traverse tube had been, to allow for better comparison of these measurements with counter traverses, etc.

TABLE I.B.10. Fission Ratio Measurements
Relative to ^{235}U in ZPPR Assembly 2

Ratio	Measurement	Calculation	C/E
U-233/U-235	1.446 ± 0.022	1.384	0.957
U-234/U-235	0.1492 ± 0.0023	0.1309	0.878
U-236/U-235	0.0443 ± 0.0007	0.4043	0.912
U-238/U-235	0.0201 ± 0.0004	0.01866	0.929
Pu-239/U-235	0.9372 ± 0.0142	0.8616	0.919
Pu-240/U-235	0.1704 ± 0.0026	0.1584	0.929

Calculated values were obtained (see Sect. I.B.1.a(i)(a)(1)) for the ratios measured, and the comparison appears to indicate the possibility of some consistent error in the ^{235}U cross sections, especially as the ratios quoted on a ^{239}Pu basis are in very good agreement with the calculations, as seen in Table I.B.11.

TABLE I.B.11. Fission Ratios Relative to
^{239}Pu in ZPPR Assembly 2

Ratio	Measurement[a]	Calculation	C/E
U-233/Pu-239	1.543 ± 0.033	1.606	1.041
U-234/Pu-239	0.1592 ± 0.0034	0.1520	0.955
U-235/Pu-239	1.067 ± 0.014	1.1607	1.088
U-236/Pu-239	0.0473 ± 0.0010	0.0469	0.992
U-238/Pu-239	0.0215 ± 0.0005	0.02166	1.008
Pu-240/Pu-239	0.1818 ± 0.0047	0.1839	1.011

[a]Based on data relative to ^{235}U.

(ii) <u>Mockup Critical Experiments</u> (W. P. Keeney, R. O. Vosburgh and D. Meneghetti)

Last Reported: ANL-7758, pp. 24-25 (Nov 1970).

(a) <u>Experimental Status</u>. The experimental program in support of the EBR-II Project has been completed. Assembly 63B was

loaded to critical after a proton-recoil neutron-spectrum measurement was made at a subcritical loading, simulated element-substitution worths were measured, and two sets of radial traverses in different geometries were made. Assembly 63C was then installed in the reactor, and a set of radial reaction rate traverses made.

The experiments were concluded December 11, and the unloading of the reactor is now in progress.

(b) Errata

(1) Traverse Data Assemblies 60, 61, and 62. Some of the traverse data published in previous monthly reports for Assemblies 60 through 62 have been incomplete in the titles in the error column. All errors published in all of these ZPR-3 traverse data are in percent. Also, footnotes for the axial traverses failed to appear in some instances. "The zero position is the core center, which lies on the axis, 0.53 in. from the ZPR-3 midplane, in Half No. 1. The positive positions are those in Half 1, traversing from the core center toward the top axial reflector."

(2) Foil Irradiations Assemblies 60 and 61
(D. W. Maddison)

A computer coding error resulted in incorrect values for the ^{238}U(n,f) reaction being reported for ZPR-3, Assemblies 60 and 61. (See Tables I.B.10 and I.B.11 of Progress Report for August 1970, ANL-7737.) The correct values are presented in Table I.B.12.

(c) Experimental Results, Assembly 63A

(1) Reaction-rate Traverses. Horizontal reaction-rate traverses with ^{235}U, ^{238}U, and ^{10}B counters were made in Assembly 63A (see Progress Report for November 1970, ANL-7758) through the P row of the reactor. These data are graphed in Figs. I.B.1-I.B.3.

(2) Thermoluminescent Gamma Dosimeter and Foil Irradiations. The TLD data are being processed and will be published later with a description of the experiment. The foil-irradiation data are being processed by Chemical Engineering (CEN) and will be reported by the EBR-II Project.

(d) Assembly 63B

(1) Description of the Assembly. The reference loading for Assembly 63B (Fig. I.B.4) is listed in Table I.B.13. Reflectors and blanket are identical to Assembly 63A. Publication of the available k_{ex} awaits the calculation of the final β values for the as-built assembly.

TABLE I.B.12. Corrected Values for ^{238}U Fission
for ZPR-3, Assemblies 60 and 61

Location	Assy.	^{238}U(n,f) reaction rate (per hr-g)	Relative error	Absolute Error
A-5	60	3.2605×10^{10}	.93%	2.89%
A-4	60	3.0224×10^{10}	1.04%	2.93%
A-2	60	3.2221×10^{10}	.79%	2.85%
A-1	60	3.4756×10^{10}	.88%	2.87%
A-10	60	1.4810×10^{10}	1.55%	3.14%
A-9	60	1.5211×10^{10}	1.20%	2.99%
A-7	60	1.8417×10^{10}	1.18%	2.98%
A-6	60	2.0846×10^{10}	.88%	2.87%
A-13	60	1.9274×10^{9}	4.51%	5.27%
A-12	60	2.3807×10^{9}	6.14%	6.72%
A-11	60	3.0544×10^{9}	2.19%	3.50%
F-1	60	3.2279×10^{10}	1.03%	2.92%
F-2	60	1.6077×10^{10}	3.04%	4.09%
F-3	60	9.4019×10^{9}	1.07%	2.93%
A-107	61	3.1757×10^{10}	2.25%	3.54%
A-3	61	3.0537×10^{10}	1.47%	3.10%
A-102	61	3.1195×10^{10}	1.41%	3.08%
A-101	61	3.4309×10^{10}	1.70%	3.22%
A-106	61	1.6271×10^{10}	3.90%	4.76%
A-8	61	1.5757×10^{10}	2.15%	3.48%
A-105	61	1.8862×10^{10}	1.79%	3.27%
A-104	61	2.0630×10^{10}	2.44%	3.66%
A-111	61	3.5119×10^{9}	2.88%	3.97%
A-112	61	3.2923×10^{9}	5.51%	6.15%
A-113	61	2.6699×10^{9}	6.18%	6.76%
F-11	61	3.2595×10^{10}	2.25%	3.54%
F-12	61	1.6748×10^{10}	6.79%	7.32%
F-13	61	1.3117×10^{10}	2.30%	3.58%
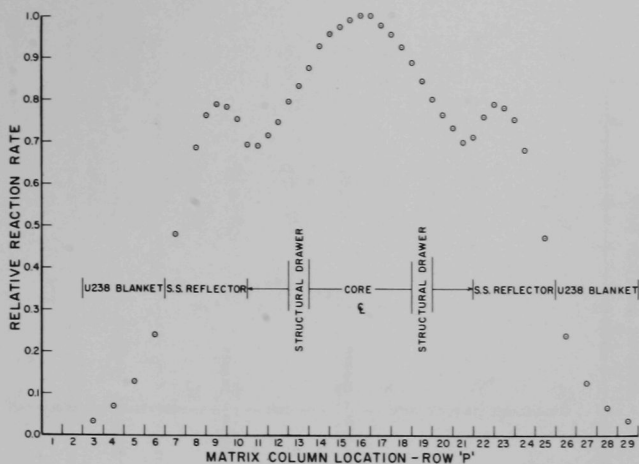
Fig. I.B.1. Horizontal ^{235}U Counter Traverse, P Row,
Assembly 63A. ANL Neg. No. ID-103-A2165.
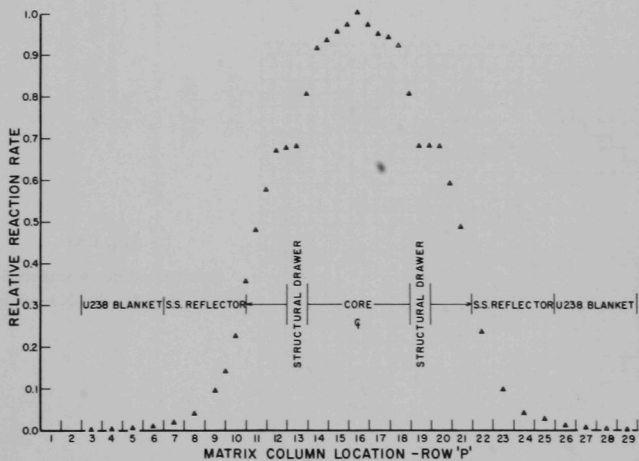
Fig. I.B.2. Horizontal ^{238}U Counter Traverse, P Row,
Assembly 63A. ANL Neg. No. ID-103-A2166.
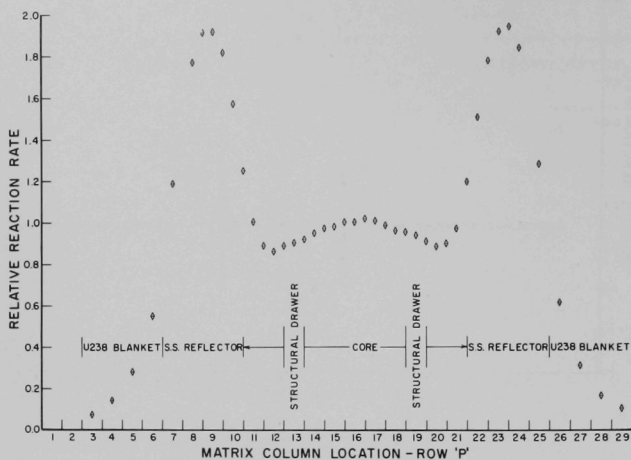
Fig. I.B.3. Horizontal ^{10}B Counter Traverse, P Row,
Assembly 63A. ANL Neg. No. ID-103-A2163.
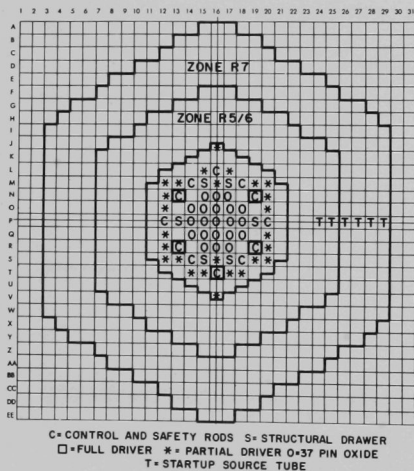
Fig. I.B.4

Reference Core, Assembly 63B.
ANL Neg. No. ID-103-A2207.

C = CONTROL AND SAFETY RODS   S = STRUCTURAL DRAWER
□ = FULL DRIVER   * = PARTIAL DRIVER   O = 37 PIN OXIDE
T = STARTUP SOURCE TUBE

TABLE I.B.13. Fissile Mass in Reference Loading
of ZPR-3 Assemblies 63B and 63C

Drawer Type	63B (63-35)			63C (63-54)		
	Number Loaded[a]	Fissile Mass, kg		Number Loaded	Fissile Mass, kg	
		^{235}U	^{239}Pu[b]		^{235}U	^{239}Pu[b]
Partial ^{235}U Driver	25	33.691	---	20	26.953	---
Full ^{235}U Driver	30	82.258	---	39	106.936	---
Full ^{235}U Driver (half matrix tubes)[c]	6	16.567	---	7	19.328	---
19-pin Oxide	0	---	---	8	7.096	3.443
37-pin Oxide	21	37.254	9.038	8	14.192	3.443
EBR-II Control/Safety	7	13.113	---	7	13.113	---
ZPR-3 Control/Safety	5	9.356	---	5	9.356	---
Structural	6	---	---	6	---	---
Total	100	192.239	9.038	100	196.974	6.886

[a]In each half of ZPR-3.

[b]Includes ^{241}Pu.

[c]The half drawers are loaded such that a pair is equal to one core drawer plus one radial reflector drawer. The plates in these half drawers are loaded horizontally.

(2) Experimental Results Assembly 63B

(A) Proton-recoil Neutron-spectrum Measurement.
The data from the proton-recoil neutron-spectrum measurement at the center of the simulated 37-pin oxide element zone are now being processed.

(B) Radial Reaction-rate Traverses. Two sets of radial reaction-rate traverses with ^{235}U, ^{238}U, and ^{10}B counters were made in Assembly 63B. The first set was measured with the P row loaded as in Fig. I.B.4. The P row was modified by placing a simulated structural element in P-16 and simulated full driver elements in P-13 and P-19 for the second set of traverses. These data are being processed.

(C) Worth of Simulated Elements. The worths of simulated structural and 37-pin oxide elements in P-11 and simulated structural and full driver elements in P-16 and a simulated full driver element in P-13 were measured. The analysis of these data will be completed when the as-built β values are available.

(e) Assembly 63C

(1) Description of the Assembly. The reference loading for Assembly 63C, Fig. I.B.5, is listed in Table I.B.13. No changes in reflectors or blanket were made in the transition to Assembly 63C. Publication of the available k_{ex} awaits the calculation of the final β values for the as-built assembly.

(2) Radial Reaction-rate Traverses. Radial reaction-rate traverses through the P row with ^{235}U, ^{238}U, and ^{10}B counters were made. These data are being processed.

C = CONTROL AND SAFETY RODS S = STRUCTURAL DRAWER
□ = FULL DRIVER ＊ = PARTIAL DRIVER O = 37 PIN OXIDE
♦ = 19 PIN OXIDE T = STARTUP SOURCE TUBE

Fig. I.B.5. Reference Core, Assembly 63C.
ANL Neg. No. ID-103-A2208.

(f) Foil-activation Measurement Results, Assembly 62
(D. W. Maddison)

Activation measurements of heterogeneity effects involving nine different neutron reactions were made in the same six matrix positions as in Assemblies 60 and 61. Complete sets of measurements were made at the core center, on the core side of the core-radial blanket interface, and in the radial blanket. Partial measurements were made in three other positions. The matrix

locations of the foils are the same as for Assemblies 60 and 61. (See Figs. I.A.25 of ANL-7688 and I.B.23-I.B.26 of ANL-7737, noting that Position 1-M-11 is completely within the core region for Assembly 62 and also the subsequent reflector changes.) Table I.B.14 gives the corresponding packet identification for each of the three assemblies; Table I.B.15 presents the activation results for Assembly 62.

TABLE I.B.14. Corresponding Foil-packet Identification for ZPR-3, Assemblies 60, 61, and 62

Corresponding Packets Located in Identical Matrix Positions		
Assembly 62	Assembly 61	Assembly 60
A-201	A-101	A-1
A-202	A-102	A-2
A-205	A-3	A-4
A-204	A-107	A-5
A-206	A-104	A-6
A-109	A-105	A-7
A-110	A-8	A-9
A-208	A-106	A-10
A-211	A-111	A-11
A-212	A-112	A-12
A-213	A-113	A-13
F-21	F-11	F-1
F-22	F-12	F-2
F-23	F-13	F-3

TABLE I.B.15. Absolute Reaction Rates for ZPR-3, Assembly 62

Drawer	Foil Location	Reaction	Reaction Rate (per hr-g)	Relative Error, %	Absolute Error, %
1-Q-15	A-204	$^{235}U(n,f)$	3.270×10^{11}	1.32	3.07
		$^{238}U(n,f)$	2.284×10^{10}	3.47	4.41
		$^{238}U(n,\gamma)$	3.440×10^{10}	1.21	2.99
		$^{27}Al(n,\alpha)$	3.107×10^{8}	3.16	4.18
		$^{58}Ni(n,p)$	2.526×10^{10}	0.84	2.86
		$^{197}Au(n,\gamma)$	6.203×10^{10}	0.52	2.78
		$^{186}W(n,\gamma)$	2.461×10^{10}	1.20	2.99
		$^{115}In(n,n')$	2.995×10^{10}	0.74	2.83
		$^{115}In(n,\gamma)$	1.020×10^{11}	4.41	5.19
	A-205	$^{235}U(n,f)$	3.241×10^{11}	2.01	3.39
		$^{238}U(n,f)$	1.861×10^{10}	5.55	6.19
		$^{238}U(n,\gamma)$	3.376×10^{10}	1.26	3.01
		$^{27}Al(n,\alpha)$	2.909×10^{8}	4.51	5.27
		$^{58}Ni(n,p)$	2.367×10^{10}	0.86	2.87
		$^{197}Au(n,\gamma)$	6.460×10^{10}	0.61	2.80
		$^{186}W(n,\gamma)$	2.444×10^{10}	1.04	2.93
		$^{115}In(n,n')$	2.966×10^{10}	0.73	2.83
		$^{115}In(n,\gamma)$	1.015×10^{11}	1.80	3.27

TABLE I.B.15 (Contd.)

Drawer	Foil Location	Reaction	Reaction Rate (per hr-g)	Relative Error, %	Absolute Error, %
1-Q-15	A-202	^{235}U(n,f)	3.163×10^{11}	1.46	3.10
		^{238}U(n,f)	2.171×10^{10}	1.74	3.24
		^{238}U(n,γ)	3.500×10^{10}	1.27	3.01
		^{27}Al(n,α)	3.082×10^{8}	4.93	5.64
		^{58}Ni(n,p)	2.455×10^{10}	1.11	2.95
		^{197}Au(n,γ)	6.445×10^{10}	0.61	2.80
		^{186}W(n,γ)	2.534×10^{10}	0.88	2.87
		^{115}In(n,n')	2.827×10^{10}	0.76	2.84
		^{115}In(n,γ)	1.006×10^{11}	1.01	2.91
	A-201	^{235}U(n,f)	3.199×10^{11}	1.97	3.37
		^{238}U(n,f)	2.221×10^{10}	3.06	4.10
		^{238}U(n,γ)	3.506×10^{10}	0.86	2.86
		^{27}Al(n,α)	3.271×10^{8}	3.25	4.25
		^{58}Ni(n,p)	2.640×10^{10}	0.79	2.85
		^{197}Au(n,γ)	6.312×10^{10}	0.61	2.80
		^{186}W(n,γ)	2.427×10^{10}	1.25	3.01
		^{115}In(n,n')	3.413×10^{10}	8.00	8.45
		^{115}In(n,γ)	1.084×10^{11}	1.62	3.18
1-Q-11	A-208	^{235}U(n,f)	2.209×10^{11}	1.24	3.00
		^{238}U(n,f)	1.023×10^{10}	1.85	3.30
		^{238}U(n,γ)	2.941×10^{10}	0.84	2.86
		^{27}Al(n,α)	1.619×10^{8}	3.54	4.48
		^{58}Ni(n,p)	1.234×10^{10}	1.13	2.96
		^{197}Au(n,γ)	7.959×10^{10}	0.48	2.78
		^{186}W(n,γ)	4.110×10^{10}	0.88	2.87
		^{115}In(n,n')	1.491×10^{10}	0.79	2.84
		^{115}In(n,γ)	9.550×10^{10}	1.18	2.98
	A-110	^{235}U(n,f)	2.166×10^{11}	1.49	3.11
		^{238}U(n,f)	1.027×10^{10}	2.57	3.75
		^{238}U(n,γ)	2.348×10^{10}	1.95	3.36
		^{27}Al(n,α)	1.432×10^{8}	6.44	7.00
		^{58}Ni(n,p)	1.213×10^{10}	0.94	2.89
		^{197}Au(n,γ)	6.388×10^{10}	0.56	2.79
		^{186}W(n,γ)	2.616×10^{10}	1.50	3.12
		^{115}In(n,n')	1.502×10^{10}	0.84	2.86
		^{115}In(n,γ)	8.741×10^{10}	2.79	3.91
	A-109	^{235}U(n,f)	2.290×10^{11}	2.64	3.80
		^{238}U(n,f)	1.053×10^{10}	2.24	3.53
		^{238}U(n,γ)	2.373×10^{10}	0.59	2.80
		^{27}Al(n,α)	1.819×10^{8}	3.23	4.23
		^{58}Ni(n,p)	1.439×10^{10}	1.69	3.22
		^{197}Au(n,γ)	5.897×10^{10}	0.50	2.78
		^{186}W(n,γ)	2.365×10^{10}	0.82	2.85
		^{115}In(n,n')	1.840×10^{10}	1.10	2.95
		^{115}In(n,γ)	8.672×10^{10}	2.50	3.71
	A-206	^{235}U(n,f)	2.388×10^{11}	2.22	3.52
		^{238}U(n,f)	1.450×10^{10}	2.84	3.95
		^{238}U(n,γ)	2.365×10^{10}	0.55	2.79
		^{27}Al(n,α)	2.145×10^{8}	3.51	4.45
		^{58}Ni(n,p)	1.635×10^{10}	0.84	2.86
		^{197}Au(n,γ)	5.446×10^{10}	0.61	2.80
		^{186}W(n,γ)	2.151×10^{10}	1.65	3.19
		^{115}In(n,n')	1.950×10^{10}	2.12	3.46
		^{115}In(n,γ)	7.437×10^{10}	5.04	5.73

TABLE I.B.15 (Contd.)

Drawer	Foil Location	Reaction	Reaction Rate (per hr-g)	Relative Error, %	Absolute Error, %
1-Q-9	A-213	^{235}U(n,f)	2.382×10^{11}	1.68	3.21
		^{238}U(n,f)	1.539×10^{9}	2.75	3.88
		^{238}U(n,γ)	6.024×10^{10}	0.48	2.78
		^{27}Al(n,α)	1.853×10^{7}	10.70	11.05
		^{58}Ni(n,p)	1.293×10^{9}	3.91	4.77
		^{197}Au(n,γ)	2.291×10^{11}	0.46	2.77
		^{186}W(n,γ)	1.817×10^{11}	1.13	2.96
		^{115}In(n,n')	2.516×10^{9}	4.36	5.15
		^{115}In(n,γ)	2.149×10^{11}	1.12	2.96
	A-212	^{235}U(n,f)	2.482×10^{11}	0.92	2.88
		^{238}U(n,f)	1.745×10^{9}	7.25	7.75
		^{238}U(n,γ)	6.130×10^{10}	0.48	2.78
		^{27}Al(n,α)	2.451×10^{7}	10.11	10.47
		^{58}Ni(n,p)	1.688×10^{9}	3.41	4.37
		^{197}Au(n,γ)	2.240×10^{11}	0.45	2.77
		^{186}W(n,γ)	1.740×10^{11}	0.68	2.82
		^{115}In(n,n')	3.314×10^{9}	2.90	3.99
		^{115}In(n,γ)	2.066×10^{11}	0.61	2.80
	A-211	^{235}U(n,f)	2.502×10^{11}	1.03	2.92
		^{238}U(n,f)	2.093×10^{9}	5.02	5.72
		^{238}U(n,γ)	6.007×10^{10}	0.49	2.78
		^{27}Al(n,α)	3.256×10^{7}	9.31	9.70
		^{58}Ni(n,p)	1.856×10^{9}	6.84	7.37
		^{197}Au(n,γ)	2.164×10^{11}	0.47	2.77
		^{186}W(n,γ)	1.674×10^{11}	0.63	2.81
		^{115}In(n,n')	3.931×10^{9}	3.64	4.55
		^{115}In(n,γ)	2.048×10^{11}	1.19	2.98
1-P-16	F-21	^{235}U(n,f)	3.449×10^{11}	1.70	3.22
		^{238}U(n,f)	2.036×10^{10}	2.83	3.94
		^{238}U(n,γ)	3.467×10^{10}	0.92	2.88
		^{197}Au(n,γ)	6.250×10^{10}	0.46	2.77
1-P-11	F-22	^{235}U(n,f)	2.323×10^{11}	4.67	5.41
		^{238}U(n,f)	1.243×10^{10}	2.04	3.41
		^{238}U(n,γ)	2.625×10^{10}	1.23	2.95
		^{197}Au(n,γ)	6.155×10^{10}	0.48	2.78
1-M-11	F-23	^{235}U(n,f)	2.004×10^{11}	0.76	2.78
		^{238}U(n,f)	8.986×10^{9}	4.02	4.86
		^{238}U(n,γ)	2.422×10^{10}	0.66	2.81
		^{197}Au(n,γ)	6.546×10^{10}	0.48	2.78

C. Component Development

1. Instrumentation and Control

a. FFTF Instrumentation Development (R. A. Jaross) (189a 02-025)

Prototypes of permanent-magnet and eddy-current probe-type flowsensors are being designed, fabricated, and flowtested to establish detailed specifications and design for the FFTF permanent-magnet probe-type flowsensor, and to provide technical guidance to ensure competence in commercial fabrication of probe-type flowsensors. Supporting tests are conducted to determine radiation and long-term thermal effects on permanent-magnet materials of interest, and to study the effects of simulated fission-gas release on flowsensor response.

Flowtests and certain supporting tests are conducted in existing facilities (CCTL or CAMEL); new specialized facilities are designed and constructed, as required.

(i) In-core Flowsensors (T. P. Mulcahey)

(a) Permanent Magnet Probe-type Flowsensors (F. Verber)

Last Reported: ANL-7758, pp. 27-28 (Nov 1970).

Figure I.C.1 is a composite plot of flowsensor output signal and loop sodium flow rate versus time for the Type A-4$\frac{1}{4}$ Flowsensor (No. 1) that has been operating in the CCTL at 1100°F since July 2, 1970.
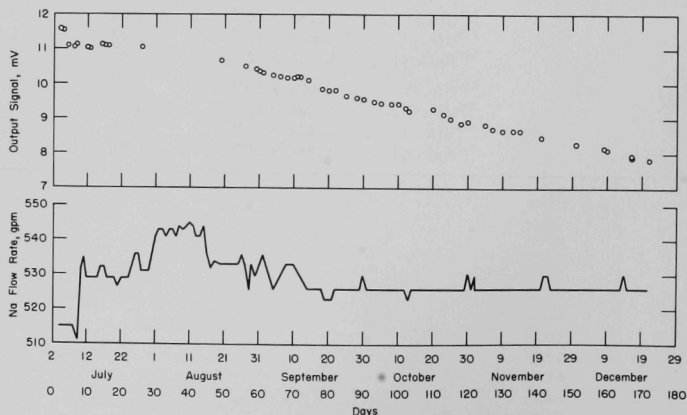

Fig. I.C.1. Operating History of Type A-4$\frac{1}{4}$ Permanent-magnet Probe-type Flowsensor in the CCTL at 1100°F

Reexamination of the data revealed that the initial output signal was ~11.6 mV, instead of 10.5 mV as reported previously. Thus after 4121 hr of operation, the signal output has decreased 32.8%, and shows no promise of leveling off.

As proposed in ANL-7753 (Progress Report for October 1970, p. 40), tests were conducted to determine whether the magnetic field produced by the permanent magnet of an A-4$\frac{1}{4}$ Flowsensor could be approximated by an electromagnet. Two electromagnets were tested. One was wound with ceramic-insulated, 0.015-in.-dia, nickel-clad silver wire, and the other with woven-glass insulated, No. 26 AWG copper wire.

As predicted, the I^2R losses in both units were prohibitive, exceeding 125 W, while yielding only ~50% of the desired flux density. These findings essentially eliminate the possibility of replacing the permanent magnet with an electromagnet for flowsensor application.

Consistent with discussions at Richland, Washington, on September 2-4, 1970, and at ANL on December 11, 1970, Fig. I.C.2 shows one concept of a perm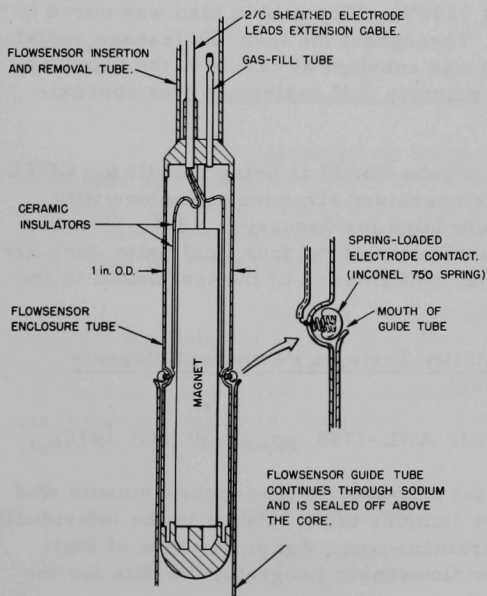anent-magnet probe-type flowsensor for operation in dry thimbles of the FFTF. The flowsensor is equipped with spring-loaded electrode contacts, and is designed for insertion and removal through a guide tube that is sealed from the sodium above the core. Insertion of the flowsensor to a position above the core permits it to sense the sodium flow velocity along the outside of the tube. Thus far, no mockup tests have been conducted to establish feasibility of the concept.

Fig. I.C.2. Concept of Permanent-magnet Flowsensor with Spring-loaded Electrode Contacts for Operation in Dry Thimble

(b) Eddy-current Probe-type Flowsensors (J. Brewer)

Last Reported: ANL-7753, pp. 40-41 (Oct 1970).

Failure of the finalized model of eddy-current probe-type sensor No. 11 has been traced to the latest procedure for heat-curing the

respective ceramic insulation used on the coils. During fabrication, the coils are wound with gold wire insulated with Secon D. Simultaneously, a second insulation, Ceramabond 503, is wound into the coil in liquid form. Ceramabond 503 cures in air at 250-1000°F; Secon D final cures at 1500-1550°F in an unspecified atmosphere. The coils on EC probes prior to No. 11 were cured in air up to 1550°F. This resulted in surface oxidation of the Type 304 stainless steel sheath enclosing the probe and leads, which was suspected of affecting probe performance.

To eliminate the oxidation, Probe No. 11 was initially cured to 450°F in air (sufficient for Ceramabond 503), and final cured to 1550°F in a vacuum. At temperatures above 1200°F, the coil insulation resistance began to break down and failed completely at 1500°F. Subsequent examination revealed that both insulations had carburized. Also, the gold wire was embrittled; it broke into short lengths on being unwound from the coils. This was probably caused by grain growth at high temperature due to contamination by entrapped volatile constituents of the Secon D binder. The vendor of Secon D has advised that absence of oxygen at the high-curing temperature would cause the effects that were observed.

In an earlier oven test, a gold wire-wound bobbin (SSX-6-2) accumulated 1728 hr at 1300°F. This bobbin also was cured in air, using the earlier procedure. Throughout the test, the leakage resistance between the coils and bobbin was constant at ~1.5 MΩ, the unbalance signal also was constant, and the primary coil resistance was approximately 8.2 Ω.

Accordingly, Probe No. 11 is being rebuilt for CCTL testing, using the previous high-temperature air-cure procedure with minor revisions; completion is scheduled for January 8, 1971. In order not to delay the scheduled ANL fabrication of the four final units, they are being built without waiting for final confirmation of the test model in the CCTL.

(c) Thermal Stability Tests on Permanent Magnets (G. A. Forster)

Last Reported: ANL-7758, pp. 28-30 (Nov 1970).

The second set of magnetic-flux measurements was made on Alnico V and VIII magnet samples after 1500 hr in the individually heated, multisection, high-temperature oven. Again, because of their immediate value to the probe-type flowsensor program, the data for the Alnico VIII samples were analyzed.

Table I.C.1 lists the results in terms of percent changes from the initial magnetic field strength of each sample. Each percentage represents the average of five samples for the specific

temperature and L/D ratio shown. At both 900 and 1000°F, the field strengths continue to increase. At 1100°F, the values are holding steady after an initial increase. At 1200°F, the field strengths continue to decrease.

TABLE I.C.1. Thermal Stability of Alnico VIII
Magnets at 900-1200°F

Temp, °F	L/D Ratio	Avg Change, %	
		818 hr	1500 hr
900	1	+ 6.1	+ 7.1
	2	+ 5.1	+ 5.9
	4	+ 4.4	+ 4.6
1000	1	+14.6	+16.5
	2	+ 8.5	+10.9
	4	+ 7.7	+ 9.1
1100	1	+17.0	+16.8
	2	+11.7	+12.2
	4	+ 7.8	+ 8.3
1200	1	- 7.0	-24.5
	2	-10.2	-28.4
	4	- 6.4	-16.4

Although all these magnet samples were temperature-stabilized by cycling to 1300°F, it is evident that this procedure did not stabilize them from further decreases at 1200°F. Apparently some type of recovery occurs at 1100°F (and below) that affects the shorter magnets more than the longer ones.

Various types of high-cobalt Alnico VIII permanent magnets are being procured from three major vendors for similar tests. These include 28 magnets suitable for use in the A-4$\frac{1}{4}$ Flowsensor, and eight small cobalt-rare earth magnets. New methods of temperature stabilization will be investigated in an effort to achieve long-range thermal stability of the magnets.

(d) Magnetometer Probe-type Flowsensors (D. E. Wiegand)

Last Reported: ANL-7758, pp. 30-32 (Nov 1970).

A computer program (MAGFLOM) usable in the IBM-360 system has been written to provide operational parameters and performance data for the magnetometer flowsensor. Thus far, the program has been used to search for an optimum spacing between the field magnets.

An inflection point in the field-gradient curve at the center point between the magnets would relax the drift-off balance problem. However, no such condition was found: The field gradient at the center point increased continuously as the spacing between magnets was decreased.

Another possible optimum spacing might yield a maximum sensitivity. However, the sensitivity also increases continuously as the magnet spacing is decreased. The field gradient increase is more rapid than the sensitivity increase, so there is no optimum spacing on the basis of maximum sensitivity or minimum field gradient.

Program MAGFLOM has confirmed an important characteristic predicted earlier by a very rough analysis: With a suitable magnet-magnetometer configuration, the radius for maximum sensitivity to fluid velocity can be extended beyond the capsule sheath radius. For example, with 2-in.-long magnets spaced at 2 in. between facing poles, the radius for maximum sensitivity is 0.48 in.

MAGFLOM further shows that with 2-in. magnets spaced 2 in. apart, the sensitivity falls 20 dB below the peak value at a radius of 2.1 in. Increasing the spacing extends the radius of maximum response and reduces the rate of response fall-off with radius increase. With this configuration, it was also shown that a movement of about 0.010 in. from the neutral position of the magnetometer is required for an unbalance signal equivalent to a sodium velocity of 1 ft/sec. This value indicates that suitable dimensional stability should not be too difficult to achieve, if attention is given to possible thermal gradients in the design of the mounting arrangement.

2. Fuel Handling, Vessels, and Internals

    a.   Core Component Test Loop (CCTL) (R. A. Jaross) (189a 02-026)

The CCTL is operated, maintained, and modified to facilitate long-term tests of prototype FFTF fuel assemblies and in-core instrumentation in sodium under conditions established by the FFTF and LMFBR Programs. Technologies pertinent to sodium-loop operation (e.g., surveillance of sodium and cover-gas quality, and material compatibility, including the Type 304 loop structure) are developed and improved concurrently.

    (i)   Operation of Loop to Test Second FFTF Subassembly (F. A. Smith)

Last Reported: ANL-7758, p. 33 (Nov 1970).

As of December 22, 1970, the CCTL has completed 4342 hr of flowtesting the Mark-II FFTF fuel assembly at 1100°F and ~525 gpm.

During the reporting period, the CCTL accumulated 768 hr of flowtesting, with no downtime, for a total operating factor of 100%.

D. Systems and Plant Development

1. Sodium Technology

a. On-line Monitoring and Sampling for Sodium Systems (189a 02-021)

Argonne National Laboratory has been given the responsibility of implementing a national meter program for developing, testing, and establishing commercial availability of meters for use on FFTF and other LMFBR systems. The meters to be developed and characterized in this program consist of monitors for oxygen, carbon, and hydrogen and a leak detector for steam generators. The FFTF schedule requires commercial availability of the oxygen and carbon meters by July 1971.

(i) Oxygen-monitoring Station (J. T. Holmes and V. M. Kolba)

Last Reported: ANL-7742, p. 31 (Sept 1970).

A program has been established that is expected to result in the commercial availability of improved electrochemical oxygen meters by July 1971. In support of this program, a pumped sodium apparatus has been constructed to prooftest up to four oxygen meters, and operation of the apparatus has begun.

An important test of the effect of radiation on currently available oxygen meters is being planned for initiation at EBR-II early in 1971. Design of equipment is complete and fabrication of components for this test is under way.

A preliminary conceptual design has been developed for an on-line monitoring module containing two oxygen meters and one hydrogen meter and the associated hardware and electronics. Comments from EBR-II and FFTF on the concept are being incorporated in the detailed design.

A preliminary conceptual design has been completed for an on-line module that will be used for oxygen-meter calibration; the calibration method to be used involves the equilibration of vanadium-metal specimens in sodium, analysis of the specimens for oxygen, and determination of the oxygen content of the sodium from previously measured equilibrium constants.

Apparatus is being designed to provide for the characterization of 10 oxygen meters as part of the national meter program. The apparatus will have provisions for up to 10 meters and an on-line calibration device.

(ii) <u>Hydrogen-monitoring Station</u> (J. T. Holmes and D. R. Visser)

Last Reported: ANL-7742, p. 32 (Sept 1970).

Development work on the ANL diffusion-type hydrogen-activity meter is being continued. Either this meter, which is being given primary consideration, or the UNC electrochemical meter will serve as the on-line meter component of an oxygen-hydrogen meter module. Earlier studies with the ANL hydrogen-activity meter showed that equilibrium hydrogen pressures measured in a gas-flow system with standardized hydrogen-argon gas mixtures were approximately 25% lower than the values calculated from gas-chromatographic analyses. Recent information has indicated that the discrepancy resulted from an incorrect factor for calibrating the pressure sensor (a Varian Millitorr ion gauge) for use with hydrogen.[*] This factor has been revised, and our measured pressures are now in good agreement with results of gas-chromatographic analyses. This agreement indicates that the Millitorr gauge, when calibrated for hydrogen, possesses the potential to serve as the sensor component of the ANL hydrogen meter.

Tritium data reported by EBR-II[**] for the secondary and primary sodium systems have been used to calculate the in-sodium level of hydrogen in these systems. In the calculation, it was assumed that tritium is a radioactive tracer for hydrogen, and the tritium data were used to calculate the distribution coefficient of hydrogen between the sodium and the cover gas. Since the distribution coefficient varies with the level of hydrogen dissolved in the sodium (Sievert's law), one can determine the level of hydrogen present in the sodium from the distribution coefficient and the Sievert's-law constant for the hydrogen-sodium system.[†] The results of this analytical technique indicated that the secondary sodium at EBR-II contains 0.2-0.3 ppm of dissolved hydrogen as hydride, whereas the primary sodium contains about 0.4 ppm of hydrogen as hydride.

---

[*]The gauge is originally calibrated with nitrogen, and the factor previously used was recommended by the manufacturer. The revision of this factor is based on recent studies by K. B. Das, Boeing Development Center, Seattle, Washington (private communication).

[**]W. H. Olson, EBR-II, private communication.

[†]Calculations based on the data of S. A. Meacham et al., APDA-228 (1968).

(iii) <u>Carbon-monitoring Station</u> (J. T. Holmes and C. Luner)

Last Reported: ANL-7742, pp. 32-33 (Sept 1970).

The meter being given primary consideration for the carbon-monitoring station is a modification of the United Nuclear Corporation (UNC) diffusion meter. A pumped-sodium loop (Test and Evaluation Apparatus, TEA) is being used to establish (1) a standard carbon probe and housing design and (2) recommended operating temperature, decarburizing gas composition, and sodium flow rate.

A new carbon-meter housing with a relatively inert (molybdenum) liner has been installed on TEA in parallel with the standard UNC carbon meter assembly, which has a stainless steel housing. A bypass sampler and a device for exposing metal specimens (iron or iron-nickel alloys) to flowing sodium have also been installed. The entire system has been tested and filled with sodium.

In experiments currently being planned, the activity of carbon in sodium will be determined from the metal specimens equilibrated with the carbon contained in the sodium, and a correlation of carbon-meter readings with the measured activities will be attempted.

(iv) <u>Detection of Leaks in Steam Generators</u> (J. T. Holmes and D. R. Vissers)

Last Reported: ANL-7742, p. 33 (Sept 1970).

The work in this program involves the evaluation of requirements for a leak detector for LMFBR steam generators and the development and prooftesting of a detection system to meet these needs. A diffusion-type hydrogen monitor is currently under development at ANL. This monitor appears to have the desired sensitivity for warning of potentially very high rates of tube wastage from water inleakage; i.e., it has the capability of detecting a 4% change in the hydrogen level at a concentration of 0.1 ppm hydrogen in sodium.

Plans are being made to supply an ANL hydrogen-meter leak detector for the Sodium Component Test Installation at the Liquid Metals Engineering Center (LMEC) for use in their test of the Atomics International "hockey stick" steam generator, scheduled for spring of 1971. Design work is also under way for a leak detection system to be installed on the secondary system at EBR-II.

b. Nonmetallic Impurity Interactions in Sodium-Metal Systems
(189a 02-137)

(i) Assessment of the Candidacy of Vanadium-Base Alloys
for Cladding LMFBR Fuels (T. F. Kassner and D. L. Smith)

Last Reported: ANL-7742, p. 34 (Sept 1970).

The corrosion of vanadium in liquid sodium has been in-
vestigated under the well-defined hydrodynamic conditions produced by
the rotating-disk sample geometry at temperatures between 450 and 700°C.
Corrosion-rate data obtained under conditions in which the linear corrosion
rate is a function of both velocity and oxygen concentration in sodium have
been reported previously. (See Progress Reports for June and September
1970, ANL-7705, pp. 55-56, and ANL-7742, p. 34.)

These data have been used in the convective-diffusion model
for mass transport to a disk to obtain values for the diffusion coefficient of
oxygen in liquid sodium. The vanadium corrosion rates were related to the
diffusional flux of oxygen to the disk by the stoichiometric relation V +
$\underline{O}_{Na}$ = VO for the vanadium monoxide corrosion product. The diffusion
coefficient of oxygen in liquid sodium from these measurements ranged
from 10^{-6} cm^2/sec at 500°C to 10^{-5} cm^2/sec at 700°C. Although the data
are encompassed by the lower limit of the range of values commonly ob-
served in liquid-metal systems, an extrapolation to lower temperatures re-
sults in unreasonably low values. Further interpretation may resolve the
problem; the results will be given in a topical report now in preparation.
No further experimental work is planned.

E. Experimental Breeder Reactor No. II--Research and Development

1. Reactor Analysis, Testing, and Methods Development (189a 02-144)

    a. Nuclear, Thermal, and Hydraulic Surveillance

        Last Reported: ANL-7753, pp. 61-73 (Oct 1970).

        (i) Noise Analysis on the EBR-II intermediate Heat Exchanger (C. C. Price and J. R. Karvinen)

        Shortly after detection of audible noise from the intermediate heat exchanger (IHX) on November 14 (see p. 55 of Progress Report for November 1970, ANL-7758), an accelerometer was mounted on a thermocouple well in the secondary sodium inlet pipe of the IHX. Noise was recorded at 62.5, 50, 40, 30, 20, 10, and 0 MWt as the reactor was shut down. The amplitude of the recorded noise peaks decreased with decreasing flow rate of secondary sodium.

        Before the discovery of the noise in the IHX, the outlet of the secondary-system heat exchanger was monitored several times as part of the signature-analysis program. Sufficient data were taken to provide reasonable assurance that the noise originating in the IHX on November 14 was not present before August 21, 1970.

        In more-extensive tests on November 17, two accelerometers and a microphone were used. One accelerometer was mounted on a bolt screwed into a thermocouple well in the inlet pipe for secondary sodium. The other was used to monitor other points along the inlet and outlet pipes. The microphone pickup was attached to the access portion of the drain pipe in the IHX inlet pipe. The primary-system pump operated at 100% of full flow, and the flow of secondary sodium was decreased in a manner corresponding to operation at 50, 40, 30, 20, 10, and 0 MWt. Noise recordings were made after each change in flow.

        In another series of measurements, flow of secondary sodium was maintained at a value corresponding to 30-MWt operation and the primary-sodium flow was changed in steps from 100-75-50-33% of full flow. In these tests, the accelerometers were on the motor housing of pump No. 1 and on the access portion of the drain pipe.

        Attempts to cross-correlate the signals from the drain pipe and the secondary-sodium inlet pipe were frustrated by the complexity of transmission paths through the system and the lack of normal signature information.

Nevertheless, useful information was generated through power spectral density measurements and slowed-down noise recordings. Observations resulting from these studies include the following:

(a) The monitoring point indicating the most noise is on the drain pipe.

(b) The noise level decreases with decreasing flow of secondary sodium.

(c) The noise level of the exit pipe for secondary sodium is lower than that of the inlet pipe.

(d) No change in noise pattern was noted when the flow rate of primary sodium was varied.

Another interesting phenomenon was noted. Usually, a given noise burst was apparent in the signals from the accelerometers on both the drain pipe and inlet pipe. On a few occasions, however, bursts were evident from the signal from the exit pipe, but were either absent or significantly reduced in the signal from the drain pipe. Such behavior is illustrated in Fig. I.E.1, which shows four noise bursts. Although burst No. 1 was sensed in the signal from the inlet pipe, it was not sensed in the drain-pipe signal. Similar behavior was noted for burst No. 3. Bursts No. 2 and 4, however, were sensed by both accelerometers. Such information suggests that the noise bursts sensed in the inlet pipe were not necessarily generated by the drain pipe of the inlet pipe.
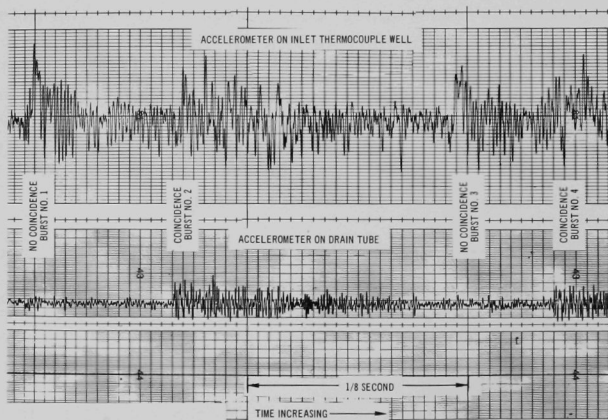

Fig. I.E.1. Noise Phenomena Recorded at Thermocouple Well and Drain Pipe of Inlet Pipe of EBR-II Intermediate Heat Exchanger

Other characteristics of the noise were noted. Whenever the noise was loudest, the repetition frequency was about 6 Hz. The noise usually remained loud for four individual bursts and then faded rapidly. On other occasions, the spacing between bursts was so small that the overall noise pattern appeared as a continuous emission. Situations between these extremes were also noted.

b.   Improved Experimental-irradiation Capability

Last Reported: ANL-7753, pp. 73-80 (Oct 1970).

(i) Measurements of Subassembly Outlet Temperatures (W. R. Wallin and F. D. McGinnis)

Melt-wire temperature monitors (see Fig. I.E.5 in Progress Report for August 1968, ANL-7487) have been successfully used to measure coolant temperatures at the outlet of subassemblies. (See Progress Report for January 1970, ANL-7661, p. 45). Table I.E.1 summarizes the results of the measurements.

TABLE I.E.1. Subassembly Coolant-outlet Temperatures

Core Position	Power, MWt	Calculated Temperature, $^{\circ}F$		Measured Temperature, $^{\circ}F$	
		Top of Core[a]	Top of Shield[a]	Thermocouple[a]	Melt Wire
1A1	50	835	834	838	>845 <890
2A1	50	830	829	813	>845 <890
2C1	50	836	835	829	>845 <890
3B1	50	844	845	849	>845 <890
3E1	50	842	844	858	>845 <890
4B1	50	879	880	875	>890 <926
4B1	62.5	925	921	891	>926[b]
5A4	50	895	894	888	>926[b]
6D1	50	873	865	None	>890 <926
6E4	50	893	886	907[c]	>890 <926
6F5	50	882	878	None	>890 <926
7A3	45	783	799	842	>813 <845
7D4	45	774	790	820	>813 <845
8E3	45	761	d	None	>813 <845
9E4	45	731	d	830	>813 <845
Nickel-materials Test					
7E3	50	d	885	None	>890 <926
7F5	50	d	885	None	>926[b]

[a] Subassemblies remained in the reactor for several runs (at full burnup); highest values are given.

[b] Melt wire installed at highest outlet temperature (926°F) was partially melted.

[c] Temperature measured at comparable core position 6C4.

[d] Not calculated.

Calculated values for temperatures cited in Table I.E.1 were derived with the COOLTEMP code (except for blanket subassemblies and nickel-material tests). Weights of fissionable and gamma-absorbing materials for each subassembly, and the experimentally determined flux distribution, were used to determine relative power in each subassembly. Rows 1 through 6 produce 86-89% of the power, Row 7 produces 5-6%, and Rows 8 through 16 produce the remainder. The variations in power division from run to run are determined by the BURNUP code. From these data, the power per subassembly is calculated.

Values for temperatures at the top of the core were established from subassembly power and coolant flow rate. Flow-rate values used were calibrated values for each subassembly, corrected by the ratio of total measured flow to Rows 1 through 7 to the total calibrated flow for these rows. Top-of-shield temperatures take into account radial heat transfer in the region from the top of the core to the top of the shield.

Thermocouple-measured temperatures are those established with thermocouples in the subassembly outlet. Thermocouples are not located above core positions 6D1, 6E4, and 6F5. The only Row-6 thermocouple is above position 6C4. Because positions 6E4 and 6C4 are the same distance from core center, the thermocouple reading for 6C4 is shown with that of 6E4. Although the thermocouples are 1/4 in. above the subassembly outlet, they are near the edge of the subassembly. Mixing of coolant flows from adjacent subassemblies is believed to be the cause for temperatures measured by thermocouples being lower than those measured by melt-wire monitors.

Temperatures measured with melt wires are shown by using the symbol $>$ (greater than) for the wire melted and $<$ (less than) for the wire not melted, meaning that the actual temperature lies between these values. For positions 5A4 and 4B1 (62.5 MWt), i.e., those positions with the highest outlet temperature, the wires had a melting point of 926°F. One of the two wires installed indicated partial melting; thus the actual temperature is believed to have been very near 926°F.

The temperature measurements with the melt wire are believed to be reliable. Samples of the wire mounted in the same manner as in the final elements were tested in an electrically heated furnace to establish the melting temperature.

Two other types of detectors were used in an attempt to measure outlet coolant temperatures in subassemblies.

The silicon carbide monitors have not shown sufficient accuracy when the technique of measuring changes in their length to indicate temperature was used. X-ray diffraction studies of lattice parameters of

silicon carbide are expected to yield better results. However, this approach will not be implemented until its accuracy and reliability are demonstrated.

Sodium-filled maximum-temperature indicators (sodium thermometers) from three subassemblies indicated temperatures far above reasonable values (greater than 1300°F). Results of later tests with electrical heating on detectors of the same design indicate that design modifications can make this method successful.

    c.   Computational Methods and Data Development

Last Reported: ANL-7737, pp. 74-87 (Aug 1970).

    (i) Activation Rates for the EBR-II Heat Exchanger and Sodium Pump (L. B. Miller and F. S. Kirn)

A method has been developed for calculating neutron-induced activity in reactor components located in the primary-sodium tank outside of the reactor vessel. The method was verified by comparing calculated and measured values for the activity of the secondary sodium and the transfer arm. The method was then applied to calculate the activity induced in the cobalt bearings in the sodium pump and in the lower ellipsoidal head of the heat exchanger. The calculated value in both components is 1 mR/hr at 1 ft.

    (ii) Fission Rates Computed by DOT; Listing by Subassembly Position and Plotting on the IBM-360/75 Computer (L. B. Miller and R. H. Rempert)

Extensive modifications have been made in the ACTIVITY subroutine of DOT to provide for automatic graphing on the IBM-360 computer of the rates for total fission, isotopic fission, absorption, gamma heating, etc. Modifications have also been completed to provide for the automatic tabulation of these activities as a function of subassembly position in XY problems. The plots may be either linear or semilogarithmic.

For example, automatic tabulation of total fission rate permits an improvement in the calculation of EBR-II power distributions, because, previously, neutron-source rate from DOT on punched cards, together with the POWER code, listed the average neutron source rate (which was assumed to be proportional to the power).

    (iii) Neutron Streaming through Subassemblies Containing Inert Gas (L. B. Miller, R. E. Jarka, and P. Fullerton)

Results of neutron-transport calculations of neutron streaming from the EBR-II core region to the reactor cover through experimental

subassemblies with no significant amount of stainless steel above the core region were reported in ANL-7753, pp. 71-73. The high-energy neutron flux (E > 3.68 MeV) incident on the reactor cover was increased by 6% above an experimental subassembly that contained only sodium above the core region. This change is small compared with the 60% reduction of the high-energy neutron flux incident on the reactor cover that resulted from replacing the depleted-uranium axial blanket with stainless steel.

Additional calculations have been made to determine the increase in neutron flux at the center of the reactor cover that would result from the insertion into EBR-II of one or a cluster of experiments containing 50 vol % gas and no stainless steel in the region above the top of the core. These cases are described in Table I.E.2. Case A represents the EBR-II reactor with the stainless steel axial reflector in Rows 2-6 and a fueled experimental subassembly containing 50% stainless steel above the core in Row 1. Case E represents the insertion into the central grid position of a single subassembly with 50 vol % gas above the core region. Case F represents the insertion of a cluster of seven such experimental subassemblies into the center of the reactor.

TABLE I.E.2. Configurations Analyzed

| Case | Regional Composition | | Size of Regions I & II | k_{eff} |
	I & II[a]	III[b]		
A	50% sodium 50% SS	SS reflector	1 row	1.00000
E	50% sodium 50% gas	SS reflector	1 row	0.99889
F	50% sodium 50% gas	SS reflector	2 rows	0.99144

[a] From top of core to bottom of upper plenum.
[b] Upper reflector.

Table I.E.3 compares the flux incident on the reactor cover that results from these substitutions with the flux in the reference case (Case A). The high-energy flux (E > 3.68 MeV) is increased by 10% for Case E and by 260% for Case F. The flux with energy greater than 1.35 MeV is increased by 6 and 245% for the same two cases, but the total flux is increased by only 3 and 34%, respectively. For Case F, the high-energy flux incident on the reactor cover above the seven subassemblies would still be only 22% greater at a given reactor power than with the depleted-uranium axial blanket in place.

TABLE I.E.3. Flux Incident at the Center of the
Reactor-cover Thermal Shield

Energy Group	Energy[a], eV	Flux, 10^{10} nvt		
		Case A	Case E	Case F
1	3.68×10^6	0.122	0.135	0.441
2	2.23×10^6	0.447	0.536	1.98
3	1.35×10^6	2.67	2.79	8.81
4	8.21×10^5	7.87	6.70	19.1
5	4.98×10^5	20.3	21.4	41.8
6	3.02×10^5	52.1	52.4	90.0
7	1.83×10^5	138.8	143.5	217.3
8	1.11×10^5	137.0	141.3	203.0
9	6.74×10^4	160.1	164.8	227.4
10	4.09×10^4	204.7	211.0	281.3
11	2.48×10^4	133.7	137.7	180.8
12	1.50×10^4	317.3	326.8	412.7
13	9.12×10^3	148.2	152.3	191.4
14	4.31×10^3	82.4	84.3	106.1
15	2.62×10^3	11.4	12.8	16.8
16	2.03×10^3	57.2	57.9	72.0
17	1.23×10^3	181.5	185.9	228.8
18	9.61×10^2	77.6	79.6	97.3
19	5.83×10^2	137.4	140.8	170.8
20	2.75×10^2	168.1	172.2	206.7
21	1.01×10^2	174.9	178.9	212.4
22	2.9×10^1	161.3	164.7	192.2
Total		2375.3	2438.4	3179.1
1 + 2 + 3	1.35×10^6	3.245	3.451	11.231

[a] Lower energy limit.

2. Operation with Failed Fuel (189a 02-148)

a. Experiments in EBR-II

Last Reported: ANL-7753, pp. 83-89 (Oct 1970).

(i) Study of Deterioration of Cladding for Driver Fuel
(P. B. Henault and R. V. Strain)

Interim postirradiation examination of Element BF-11,
the test element of the experiment in Subassembly X078 on limitations on
cladding for driver fuel, has been completed (see Progress Report for
November 1970, ANL-7758, Table I.D.10). The element has been assembled
in a new Mark-E subassembly for reinsertion in a Row-6 position for
62.5-MWt operation. The previous power and flow conditions in Row 4 for
50-MWt operation are being simulated.

Element BF-11 was irradiated to 2.73 at. % burnup as an encapsulated element in Subassemblies X017 and X052. It was then removed from its capsule, cleaned, examined, and stored in the argon cell for about one year. The element was reexamined in March 1970, then placed in the center position of Mark-E61 Subassembly X078 and irradiated an additional 1.65 at. % to a total calculated burnup of 4.38 at. % (peak fluence > 0.1 MeV of 4.8 x 10^{22} nvt).

After irradiation, Subassembly X078 was subjected to the standard sodium-removal operation for experiments. It was then subjected to: (1) visual examination and photography (both through the window and under a periscope); (2) eddy-current bond testing; (3) a diameter survey by a DR-25 gauge; (4) weighing; and (5) length measurement. The results of these examinations are as follows:

(a) Visual examination of the fuel-element bundle before disassembly revealed that BF-11 had grown about 0.1 in. during irradiation. Later measurement revealed a length of 18.211 in. Original as-built length was not measured, but two nominal as-fabricated elements were measured at 18.108 and 18.110 in. A 0.10-in. growth, therefore, probably is fairly accurate. The WADCO equation for stainless steel swelling was used to estimate the length change due to such swelling by using the calculated fluence for 1-in. segments. This estimate indicated a length change of 0.096 in.

(b) Visual examination of the element at a magnification of about two diameters (under the periscope) revealed that the element was clean, with only a few minor surface defects. These defects had been observed during the examination of BF-11 before its irradiation in X078.

(c) The results of eddy-current bond tests indicate that the fuel pin was 13.80 in. long; it was 13.72 in. long before irradiation in X078. The bond test results also indicate that the fuel pin is against the cladding more tightly near the ends of the pin than it was before irradiation in X078. No determination could be made on the sodium level.

(d) The maximum diameter increased from 0.17612 to 0.1796 in. for an increase of 3.48 mils, or 2.00%. The peak swelling shifted upward from the 6.5-in. level to 9.0 in. The measured diameter of 0.1796 at 9.0 in. represented an increase of 3.6 mils, or 2.05%. (Diameter at 2.73 at. % burnup was 0.17600 in.) Total increase at the 9.0-in. level over the original measured value is 5.1 mils, or 2.92%.

Calculations of the stainless steel swelling with the WADCO equation indicate a maximum $\Delta D/D_0$ of ~1.0%, if a maximum fluence of >0.1 MeV of 4.8 x 10^{22} nvt and an average cladding temperature of 950°F are assumed. Diameters before and after irradiation in X078 are plotted in Fig. I.E.2.
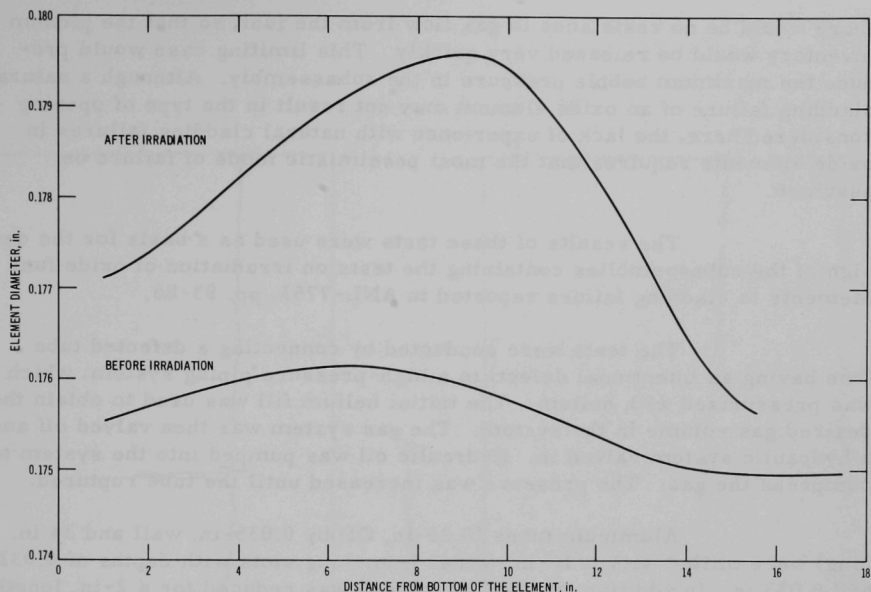
Fig. I.E.2. Diameter Profile of Element BF-11 before and after Irradiation in Subassembly X078

The weight of Element BF-11 after irradiation in X078 was 80.4 g; before this irradiation, it was 80.9 g. The difference of 0.5 g is not considered to indicate a true weight loss because the balance is only accurate to about ±0.5 g under the in-cell weighing conditions.

This examination revealed no evidence that the cladding had fractured, even though appreciable (~1.9%) diametral strain had occurred.

Because the purpose of the irradiation experiment is to cause the cladding to fracture naturally as a result of high burnup, the element has been reassembled for further irradiation.

(ii) Tube-rupture Tests in an EBR-II Hexagonal Can
(J. F. Koenig)

Tests have been conducted in which a limited volume of high-pressure gas was released in a standard EBR-II hexagonal can by rupture of a tube within the can. Room-temperature tests were run to obtain a better understanding of the change in diameter of the can that could result when the cladding of a high-burnup oxide fuel element fails and releases the fission gases stored in the plenum. For this study, the cladding failure was assumed to produce a large opening. Also assumed was that

there would be no resistance to gas flow from the fuel, so that the plenum inventory would be released very quickly. This limiting case would produce the maximum bubble pressure in the subassembly. Although a natural cladding failure of an oxide element may not result in the type of opening considered here, the lack of experience with natural cladding failures in oxide elements requires that the most pessimistic mode of failure be assumed.

The results of these tests were used as a basis for the design of the subassemblies containing the tests on irradiation of oxide fuel elements to cladding failure reported in ANL-7753, pp. 83-88.

The tests were conducted by connecting a defected tube (one having an intentional defect) to a high-pressure piping system, which was pressurized with helium. The initial helium fill was used to obtain the desired gas volume in the system. The gas system was then valved off and a hydraulic system valved in. Hydraulic oil was pumped into the system to compress the gas. The pressure was increased until the tube ruptured.

Aluminum tubes (0.25-in. OD by 0.035-in. wall and 24 in. long) were milled with 1/16-in.-wide, 1-in.-long slots with depths of 0.032 and 0.033 in. In addition, the wall thickness was reduced for a 2-in. length to obtain a large opening on rupture. The tube was in the center of a standard EBR-II hexagonal can (2.21-in. ID by 0.040-in. wall), with the defect centered axially in the $16\frac{1}{2}$-in. length of the can. A pressure transducer was adjacent to the wall inside the can, with the transducer face at the top of the defect and perpendicular to the axis of the tube. This transducer was used to measure the bubble pressure inside the can. For some tests, a second transducer was outside the can, with the transducer face parallel to the hexagonal flat, centered on the flat, and about 1/8 in. away from the surface. The transducer was at the same elevation as the other transducer and was used to measure the back pressure transmitted through the can wall. A third pressure transducer, on the tube, measured the plenum pressure for some of the tests. The outputs of the transducers were recorded on a tape recorder. The tube and hexagonal can were in the center of a 55-gal drum and submerged in water, with the defect submerged by 8-10 in. of water.

For a typical test (No. 10), the defected tube was surrounded in the can by $33\frac{1}{4}$-in.-OD tubes. The system was pressurized to 2080 psi, at which pressure the defect ruptured to form a large opening (about 3/16 in. wide for the 1-in. length) and released 5.3 cm^3 of gas. The decay of plenum pressure is shown in Fig. I.E.3. The pressure drops to 10% of its value about 1.6 msec after the start of decay. The bubble pressure inside the hexagonal can is shown in Fig. I.E.4. The pressure reached 350 psi, which would be above the pressure that would cause yielding (100 psi) (see Progress Report for August 1970, ANL-7737, p. 69) for about 2.3 msec. The
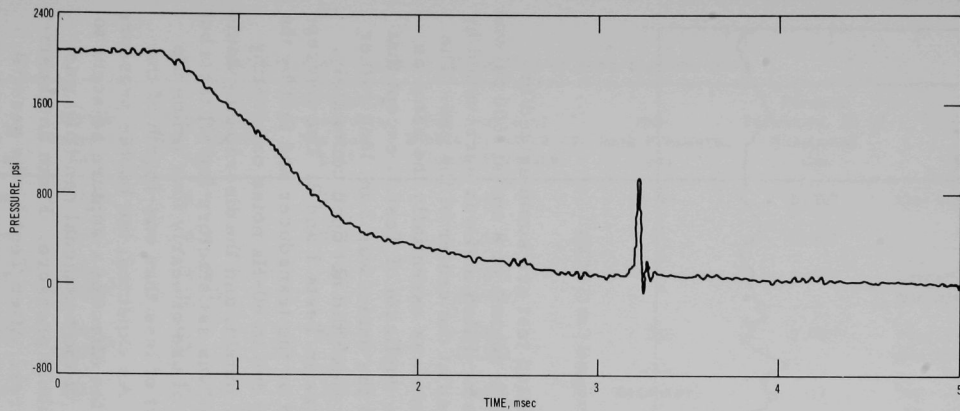
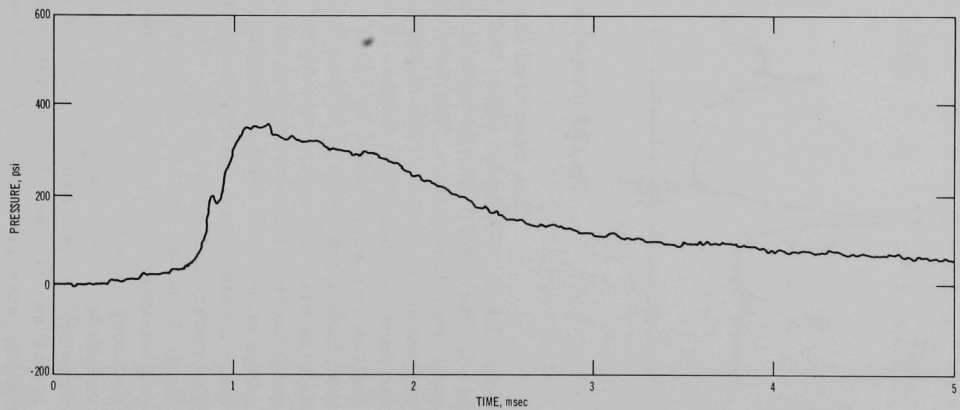Fig. I.E.3. Decay of Plenum Pressure (Test 10)

Fig. I.E.4. Gas–bubble Pressure inside Hexagonal Can (Test 10)

maximum gas-bubble pressure was 17% of the plenum pressure. The back pressure outside the can is shown in Fig. I.E.5. The pressure pulse outside the can did not last as long as the gas bubble inside the can.
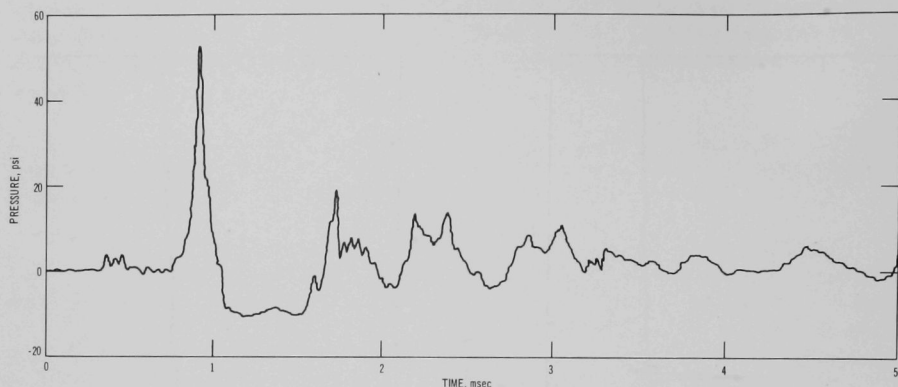

Fig. I.E.5. Back Pressure outside Hexagonal Can (Test 10)

The results of the instrumented test are summarized in Table I.E.4. For most of the test, a reference volume of 8 cm^3 at 1500 psi was used. For Test 1, the hexagonal can was water-filled, but was surrounded by air rather than water. The tube was ruptured at the center of the can. The permanent increase in the diameter of the can was essentially the same as for cans surrounded by water. Test 2 was a duplicate of Test 1, except that the can was surrounded by water. In Test 3 the defect was 2 in. long rather than having the 1-in. reference length. The notch did not open completely, and the area of rupture was about the same as in Tests 1 and 2. The discrepancy between the plenum pressure recorded by the transducer and that by the gauge on the hydraulic system was probably due to 60-Hz noise originating from a voltmeter attached to the transducer output, and the discrepancy would be present in Tests 3 and 8. The agreement was satisfactory for all tests but Tests 3 and 6. Test 6 illustrates the effect of use of nearly four times the gas volume, and Test 7 illustrates the effect of less than one-fourth of the reference gas volume of 8 cm^3 at 1500 psi. As expected, the bubble pressure varies with the volume. Test 8 illustrates the effect of a rupture adjacent to the wall; the permanent change in diameter of the hexagonal can (ΔD) was less than that expected for the measured bubble pressure. From an experimental standpoint, Tests 4 and 5 were failures. After Test 5, the gas-fill valve was found to be shut off and, judging from the results, it probably was closed for Test 4. Tests 4, 5, 9, and 10 simulated a loaded subassembly with 33 additional 1/4-in.-OD tubes added to the can. In Test 9, the data were not recorded. In Test 10, the bubble pressure was about 17% of the plenum pressure and thus higher than the 12% in the empty hexagonal can (e.g., Test 1).

TABLE I.E.4.   Summary of Results of Tube-rupture Tests

Test	Tube Opening	Plenum Pressure, psi	Compressed Gas Volume, cm^3	Max. Bubble Pressure in Hex Can, psi	Max. Ratio of Bubble Pressure to Plenum Pressure	Max. Back Pressure, psi	Maximum Permanent ΔD of Hexagonal Can	Comments
1	Large	2240	4.9	260	0.12	a	0.017	Can surrounded by air
2	Large	1880	5.8	220	0.12	a	0.012	
3	Large	2720 (4000)[b]	4.0 (2.7)	90	0.033 (0.020)	a	0.008	Larger notch did not open completely
6	Large	1600 (2000)[b]	27 (22)	410	0.26 (0.20)	250	0.063	Four times normal gas volume
7	Large	2250	1.5	100	0.044	84(spike)	nil	One-fourth normal gas volume
8	Small	290 (calc)	38	210	0.72	70	∿0.003	Defect next to wall
4	Very small	1720	6.4	28	0.016	a	nil	In Tests 4,5,9, and 10,33 additional tubes in can; fill gas prob. not added
5	Very small	3190	0.14	22	0.007	a	nil	Fill gas not added
9	Large	1700	6.4	b		a	0.032	Data not recorded
10	Large	2080	5.3	350	0.17	53(spike)	a	Can growth not measured
A	Small	(1250)[b]	14	190	0.15	a	0.026	Strain gauges on can prevented measuring max. ΔD
B	Large	(3000)[b]	6.0	360	0.12	a	0.061	Growth of hex can total of Tests A and B

[a] Not measured.

[b] Pressure from hydraulic-pump gauge.

Tests A and B, conducted before the tests discussed above, did not include the plenum- or back-pressure transducers. Strain gauges were attached to the hexagonal can that was used for both tests, and a reference volume of 8 cm^3 at 2250 psi was used. For Test A, the maximum bubble pressure was 190 psi and the circumferential strain gauge opposite the rupture indicated a strain of 2800 $\mu\epsilon$, with a permanent offset of 2300 $\mu\epsilon$. The gauge located two flats from the first set of gauges indicated a peak strain of 2600 $\mu\epsilon$ and an offset of 500 $\mu\epsilon$. No significant strain was seen on the axial gauges. The maximum measured ΔD of the hexagonal can was 0.026 in. The location of the strain gauges, however, prevented measuring the ΔD on the face directly opposite the rupture. Test B was conducted in the same can, with 36 additional 1/4-in.-OD tubes added to simulate a loaded subassembly. The circumferential strain gauges saturated during this test. After the strain gauges were removed, the maximum ΔD was 0.061 in., which was the total for both tests.

In additional uninstrumented tests in which the bursting pressure and permanent can deformation were measured, a tube was pressurized to 4000 psi, at which pressure it ruptured and released 4.5 cm^3 of high-pressure gas in the center of an empty hexagonal can. The measured permanent ΔD of the can was 0.031 in.

An additional test was made to determine the effect of the liners of a Mark-E37B subassembly on the ΔD of the hexagonal can. Three 120° filler strips of 1/32-in. 6061-T6 aluminum and three inner shields of 1/8-in. 6061-T6 aluminum were loaded into a hexagonal can. Ten-mil shim stock was used at the top and bottom to provide an annulus between the can, filler strips, and inner shield. A tube was pressurized. It ruptured at 3400 psi, releasing 5.7 cm^3 of gas and causing a maximum ΔD of 0.050 in. in the can. Thus, the liners did not prevent the change in diameter.

A test was made to determine the effect of hexagonal cans surrounding one containing a defected tube. The nominal initial spacing between the cans is 30 mils, with a 2-mil spacing at the spacer buttons. Swelling during irradiation will decrease the initial spacing and eventually close the gap if the fluence is high enough. For the first test, a central hexagonal can was surrounded by six hexagonal cans and separated from them by a 2-mil gap obtained by inserting shim stock at the tops and bottoms of the cans. The tube ruptured at 2700 psi, releasing 6.7 cm^3 of gas and causing a maximum ΔD of the can of 0.053 in. The maximum decrease in diameter of the surrounding cans was 14 mils. In the second test, the spacing was maintained at 30 mils. The tube ruptured at 2500 psi and released 7.2 cm^3 of gas. The maximum ΔD of the hexagonal can was 53 mils.

The increase in diameter of the hexagonal can might be prevented by introducing a cylinder between the inner liner and the outer wall of the can. If the diameter increase is caused by shock-wave transmission, however, the diameter could still increase. To determine whether

the diameter change is due to the shock or bubble pressure, a test was conducted with a 2-in.-OD by 1/16-in.-wall cylinder inside a standard hexagonal can. Rupture of a tube within the cylinder at 2900 psi and release of 6.2 cm³ of gas at the center of the cylinder caused no measurable growth of the hexagonal can or cylinder. This information indicates that a subassembly design that incorporates a cylinder will eliminate the changes in diameter of hexagonal cans of subassemblies that accompany a fast gas release due to a failure of fuel-element cladding.

These tests were conducted to determine the order of magnitude of the change in diameter of a hexagonal can that would result from a rapid pressure load from an expanding gas bubble. The tests were initially conducted for the program for irradiation of oxide fuel to cladding failure, in which very high burnups in the elements could result. Conservatively high simulated pressures were used in the tests, because gas pressures in elements at cladding failure cannot be predicted. Also, the pressures were required: (a) to account for the lower yield strength at 800°F (19,000 psi) than at 70°F (35,000 psi); (b) to simulate the higher shock pressure in sodium than in water;* and (c) because the milled-tube rupture technique did not produce reproducible ruptures at low pressures, and thus considerable variation occurred in the rupture pressure. Although these variations cloud the data, the following points can be drawn:

(a) Some diameter changes in hexagonal cans will occur for the reference volumes and pressures used in the tests (8 cm³ at 1500 or 2250 psi).

(b) For a tube that ruptures at the center of the hexagonal can, the bubble pressure is 12-17% of the plenum pressure.

(c) For a tube that ruptures adjacent to the hexagonal-can wall, the bubble pressure may be much higher than when the tube is in the center of the can. The ΔD of the hexagonal can, however, was small.

(d) The pressure transmitted through the hexagonal can to the water behind the can (back pressure) is lower and of much shorter duration than the bubble pressure in the hexagonal can. This difference indicates that the back pressure is not significant in limiting the growth for a single can.

3. <u>Characterization of Irradiation Environment</u> (189a 02-151)

Last Reported: ANL-7753, pp. 89-95 (Oct 1970).

(Experimental results for the EBR-II experiments on ZPR-3 discussed here are reported in Sect. I.B.4, "ZPPR and ZPR-3 Operations and Analysis.")

---

*G. A. V. Drevon, M. F. G. Falgayrettes, and W. F. Walford, "Comparison of Pressure Loading Produced by Contained Explosions in Water and Sodium," Proceedings of the Conference on Safety, Fuels, and Core Design in Large Fast Power Reactors: October 11-14, 1965, ANL-7120, pp. 720-733.

a. Axial Reaction-rate Traverses in ZPR-3 Assembly 62
    (D. Meneghetti, K. E. Phillips, and D. G. Stenstrom)

Axial reaction-rate traverses for ZPR-3 Assembly 62 have been calculated based on the flux solutions of a two-dimensional, RZ-geometry, S_4 approximation. A 29-group cross-section set derived from ENDF/B (Version I) was used.

Figures I.E.6-I.E.8 compare the calculated axial and experimental traverses through the core center for $^{235}U_f$, $^{238}U_f$, and $^{10}B_c$, respectively. Figures I.E.9-I.E.11 make analogous comparisons for axial traverses located about one-half core drawer in from the radial interface of the core and reflector. The experimental values were reported by the ZPR-3 experimental group in the Progress Report for September 1970, ANL-7742, pp. 17-21.

b. Central Fission Ratios for ZPR-3 Assembly 62
    (D. Meneghetti and K. E. Phillips)

Calculated values of fission ratios at the core center for ZPR-3 Assembly 62 are compared in Table I.E.5 with the experimental values
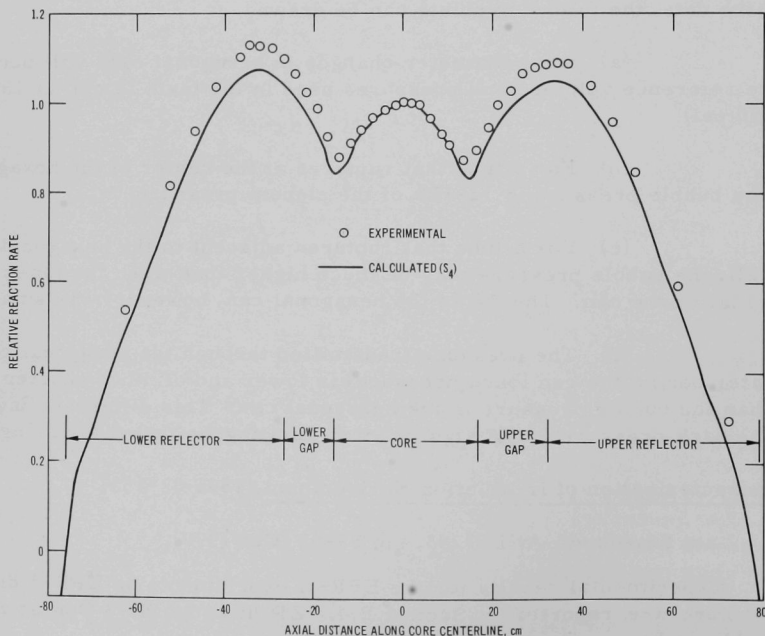

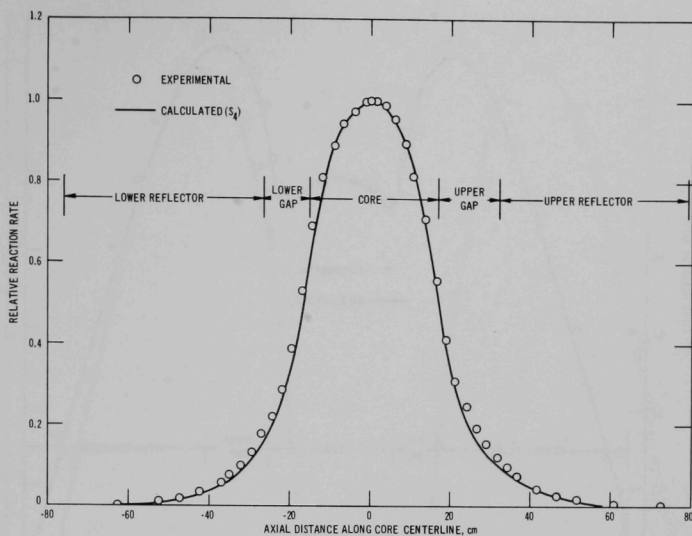Fig. I.E.6. $^{235}U_f$ Axial Traverse through the Core Center of ZPR-3 Assembly 62

Fig. I.E.7. $^{238}U_f$ Axial Traverse through the Core Center of ZPR-3 Assembly 62
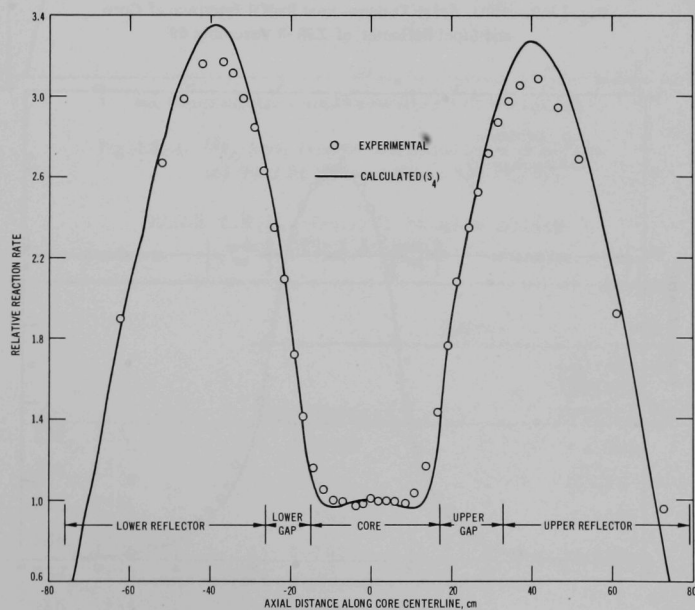

Fig. I.E.8. $^{10}B_c$ Axial Traverse through the Core Center of ZPR-3 Assembly 62

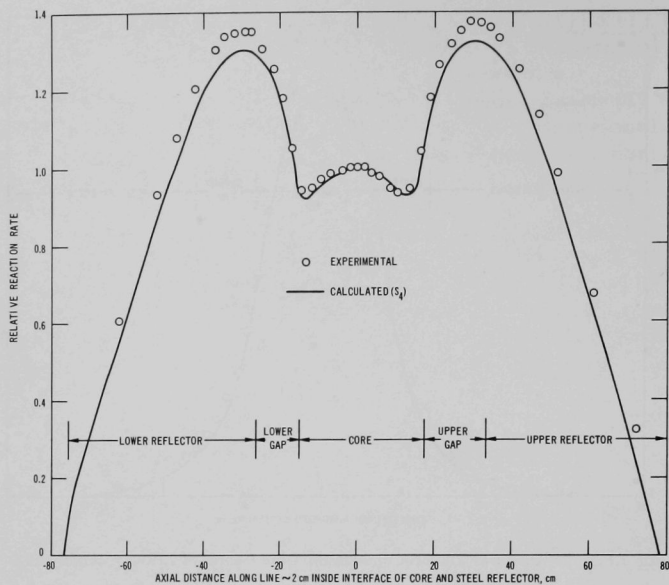Fig. I.E.9. $^{235}U_f$ Axial Traverse near Radial Interface of Core
and Steel Reflector of ZPR-3 Assembly 62
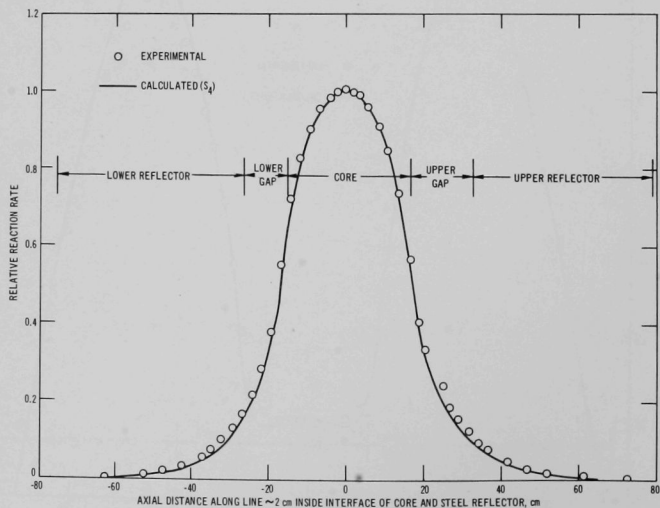
Fig. I.E.10. $^{238}U_f$ Axial Traverse near Radial Interface of Core
and Steel Reflector of ZPR-3 Assembly 62
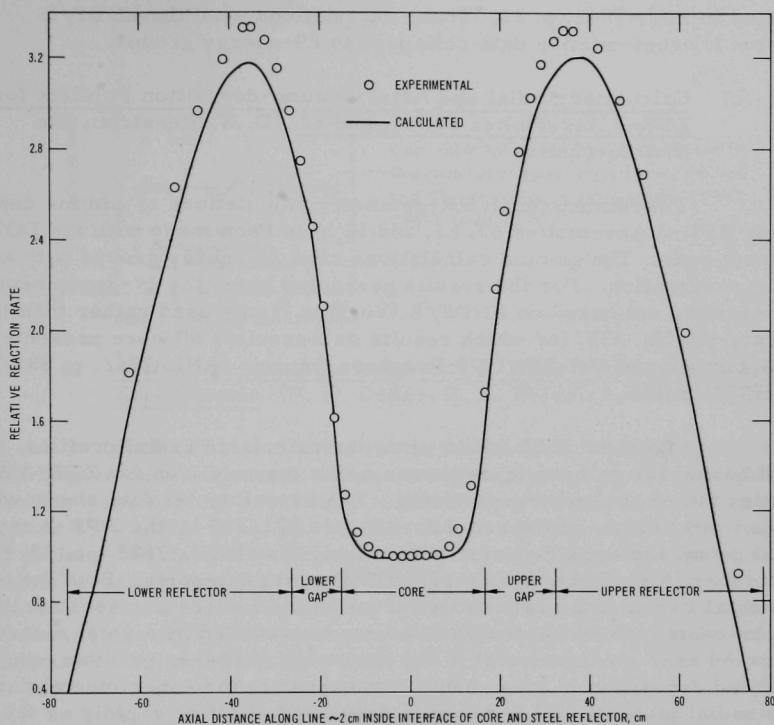
Fig. I.E.11. $^{10}B_C$ Axial Traverse near Radial Interface of Core
and Steel Reflector of ZPR-3 Assembly 62

TABLE I.E.5. Central Fission Ratios
for ZPR-3 Assembly 62

	Ratios	
	Experimental	Calculated (ENDF/B, Version I)
$^{238}U/^{235}U$	0.0677	0.0642
$^{234}U/^{235}U$	0.429	0.417
$^{233}U/^{235}U$	1.583	1.508
$^{236}U/^{235}U$	0.146	0.142
$^{239}Pu/^{235}U$	1.222	1.171
$^{240}Pu/^{235}U$	0.459	0.460

reported in ANL-7742, p. 21. These calculations used the ENDF/B (Version I) cross-section data collapsed to 29-energy groups.

   c.   Calculated Radial and Axial Gamma-deposition Profiles for ZPR-3 Assemblies 60, 61, and 62 (D. G. Stenstrom and D. Meneghetti)

        Two-dimensional, RZ-geometry calculations of gamma deposition for ZPR-3 Assemblies 60, 61, and 62 have been made with the DOT transport code. The gamma calculations used 20 energy groups with an S_8P_3 approximation. For the results presented here, the 29-group neutron cross-section set based on ENDF/B (Version I) was used rather than the 22-group set No. 238, for which results on Assembly 60 were presented in the September and October 1970 Progress Reports (ANL-7742, p. 88; ANL-7753, p. 90).

        Figures I.E.12-I.E.14 show the calculated radial profiles, in the midplane, for gamma deposition in a unit mass of iron for ZPR-3 Assemblies 60, 61, and 62, respectively. The experimental data shown were obtained with thermoluminescent dosimeters (TLD's) by the ZPR-3 experimental group and were reported in the April-May (ANL-7688, pp. 35-42) and October (ANL-7753, pp. 23-24) 1970 Progress Reports. Both the experimental data and the calculated curves in the figures are set to unity at the core center. Because the TLD's were surrounded by a steel sleeve and placed near steel material in the assembly whenever possible, the calculated deposition in iron should correspond to the experimental data. In the radial plots, the TLD traverse does not fall off as rapidly as the calculated ones in the nickel reflector and in ^{238}U-rich blanket regions.

Fig. I.E.12

Calculated Radial Gamma-deposition Profile Compared with Experimental Values Obtained with Thermoluminescent Dosimeters (TLD's): ZPR-3 Assembly 60

Fig. I.E.13

Calculated Radial Gamma-deposition Profile Compared with Experimental Values Obtained with Thermoluminescent Dosimeters (TLD's): ZPR-3 Assembly 61
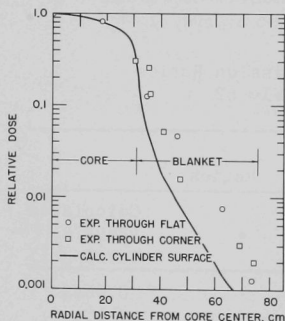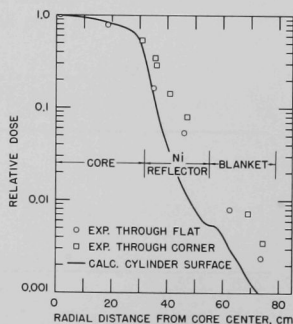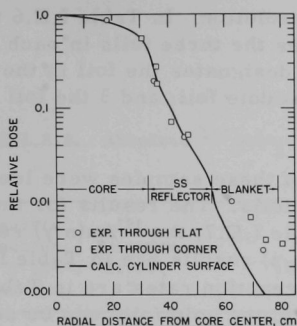
Fig. I.E.14

Calculated Radial Gamma-deposition Profile
Compared with Experimental Values Obtained
with Thermoluminescent Dosimeters (TLD's):
ZPR-3 Assembly 62

d. Activation-rate Measurements in ZPR-3 Assembly 61 Mockup
Experiments (N. D. Dudey, R. R. Heinrich, and R. J. Popek)

Foil-activation rates in Assembly 61 of the ZPR-3 mockups of
EBR-II have been measured. These measurements are similar to the re-
sults for Assembly 60 previously reported (see Progress Report for
October 1970, ANL-7753, pp. 92-95), with two important differences. The
foil packets for Assembly 61 contained aluminum foils for measuring the
$^{27}Al(n,\alpha)$ reaction in addition to ^{235}U, ^{238}U, nickel, and gold foils; and three
gold foils were irradiated together in the interface and reflector packets,
to examine the effects of resonance self-absorption in the gold foils. Each
gold foil was 0.1 mil thick.

As in the Assembly-60 irradiations, the foil packets were ir-
radiated in three positions: near the core center, on the core side of the
core-reflector interface, and in the radial reflector. These positions are
drawer numbers O-15, O-11, and O-8, respectively. The foil packets were
positioned perpendicular to the fuel plates and irradiated for a nominal
exposure of 600 W-hr. The foils were irradiated as 2 x 2-in. squares and
cut into smaller pieces for counting. The cutting patterns were selected to
optimize the sensitivity to heterogeneity effects due to the drawer-plate
structure of the assembly. Table I.E.6 summarizes the number of pieces

TABLE I.E.6. Number of Pieces Cut from Each 2 in. x 2 in.
Foil at Each Irradiation Location

Foil	Core (C)	Interface (I)	Reflector (R)
^{235}U	8	8	4
^{238}U	8	8	4
1 Au	24	8	12
2 Au	–	8	12
3 Au	–	8	12
Ni	24	24	12
Al	24	–	–

cut from each 2 x 2-in. foil for spatial resolution. In Table I.E.6 the number preceding the symbol Au differentiates the three foils in each packet of the self-absorption tests. The number 1 designates the foil in the packet closest to core center, 2 designates the middle foil, and 3 the foil farthest from core center.

Counting and data reduction of these samples were identical with those reported for the Assembly-60 foils. The results for the fission-rate determinations are presented in Table I.E.7, the $^{197}Au(n,\gamma)$ reaction-rate results are in Table I.E.8, the $^{58}Ni(n,p)$ results are in Table I.E.9, and the results for the $^{27}Al(n,\alpha)$ and $^{238}U(n,\gamma)$ reaction rates are in Table I.E.10. The effects of resonance self-absorption in the gold foils can be seen from the data in Table I.E.8. The reaction rate in the middle gold foil is reduced about 10% in the reflector packet and about 5% in the interface packet, about as expected. The surprising observation is that the reaction rate in foil 3 (farthest from core center; 3R and 3I samples) is higher than the rate in foil 1 (1R and 1I samples) for both the interface and reflector packets. This difference may indicate a reverse gradient of neutrons of very low energy, back-scattered from the nickel-reflector region.

TABLE I.E.7. Fission Rates for ^{235}U and ^{238}U Samples Irradiated in ZPR-3 Assembly 61

Sample	^{235}U Relative Fission Rate x 10^{15}, sec^{-1}	Relative Error, %	Absolute Fission Rate x 10^{15}, sec^{-1}	^{238}U Relative Fission Rate x 10^{15}, sec^{-1}	Relative Error, %	Absolute Fission Rate x 10^{15}, sec^{-1}	$^{238}U/^{235}U$
Blanket							
1	16.2	1.8	45.9	0.089	1.9	0.240	0.0052
2	16.3	1.9	46.1	0.105	1.9	0.284	0.0062
3	16.3	1.8	46.3	0.112	2.0	0.357	0.0077
4	17.2	2.0	48.6	0.150	2.3	0.408	0.0084
Interface							
1	13.6	2.0	38.6	0.556	2.2	1.51	0.0391
2	13.6	2.0	38.6	0.587	2.0	1.60	0.0413
3	12.6	2.2	35.6	0.632	1.8	1.72	0.0483
4	12.4	2.0	35.1	0.644	2.1	1.75	0.0499
5	12.4	2.0	35.2	0.726	1.9	1.97	0.0561
6	13.0	1.8	36.9	0.792	2.3	2.15	0.0583
7	13.3	2.2	37.7	0.828	1.9	2.25	0.0597
8	13.0	2.0	36.8	0.788	1.9	2.14	0.0582
Core							
1	16.0	2.0	45.4	1.14	2.1	3.09	0.0682
2	16.0	1.7	45.4	1.14	2.0	3.11	0.0685
3	16.1	1.9	45.6	1.14	1.9	3.11	0.0682
4	16.3	1.9	46.1	1.09	2.0	2.97	0.0645
5	16.0	1.9	45.4	1.13	1.8	3.08	0.0678
6	16.4	1.7	46.5	1.20	1.8	3.25	0.0699
7	17.1	2.0	48.3	1.17	1.9	3.19	0.0661
8	16.4	1.9	46.5	1.16	1.9	3.16	0.0680

TABLE I.E.8. Absolute ^{197}Au$(n,\gamma)^{198}$Au Reaction Rates in ZPR-3 Assembly 61

Sample	Absolute Reaction Rate x 10^{16}, sec^{-1}	Relative Error, %		Absolute Reaction Rate x 10^{16}, sec^{-1}	Relative Error, %		Absolute Reaction Rate x 10^{16}, sec^{-1}	Relative Error, %
1R-1	610	0.10	2R-1	553	0.15	3R-1	638	0.84
2	593	0.31	2	531	0.35	2	615	0.19
3	596	0.53	3	537	0.28	3	616	0.47
4	566	0.72	4	512	0.35	4	578	0.40
11	602	0.24	11	539	0.24	11	617	0.27
12	570	1.1	12	513	0.34	12	579	0.17
13	576	0.43	13	519	0.10	13	593	0.30
14	541	0.30	14	485	0.24	14	560	0.46
21	649	0.21	21	554	0.79	21	642	0.10
22	595	0.67	22	549	0.43	22	610	0.21
23	595	0.53	23	539	0.29	23	615	0.25
24	562	0.22	24	505	0.33	24	579	0.29
1I-1	160	0.10	2I-1	155	0.28	3I-1	168	0.82
2	149	0.25	2	142	0.10	2	153	0.29
3	114	0.38	3	109	0.40	3	114	1.34
4	93.8	0.35	4	91.7	0.64	4	94.3	0.24
5	84.3	0.71	5	83.5	0.25	5	85.3	0.23
6	80.5	0.22	6	78.3	0.55	6	78.7	0.44
7	75.8	0.54	7	73.0	0.80	7	75.8	0.45
8	75.4	0.76	8	74.5	1.0	8	76.0	0.16
C-1	73.0	0.35	C-11	76.4	0.40	C-21	76.3	0.70
2	76.2	1.02	12	76.8	0.40	22	75.4	0.23
3	74.1	0.19	13	73.6	0.10	23	74.6	0.16
4	76.3	0.29	14	76.3	0.34	24	76.6	0.29
5	76.3	0.56	15	76.5	0.44	25	76.1	0.20
6	76.1	0.52	16	74.7	0.33	26	76.5	0.10
7	75.2	0.45	17	76.0	0.84	27	75.4	0.53
8	75.8	0.36	18	75.8	0.54	28	76.7	0.81

TABLE I.E.9. Absolute ^{58}Ni(n,p)^{58}Co Reaction Rates in ZPR-3 Assembly 61

Sample	Absolute Reaction Rate $\times 10^{16}$, $\sec^{-1}$	Relative Error, %	Absolute Error, %	Sample	Absolute Reaction Rate $\times 10^{16}$, $\sec^{-1}$	Relative Error, %	Absolute Error, %
Reflector				Interface			
1	0.514	0.70	5.9	23	5.07	0.62	5.9
2	0.640	0.10	5.8	24	5.24	0.10	5.8
3	0.764	0.60	5.9	25	5.75	0.15	5.8
4	0.943	0.15	5.8	26	6.29	0.10	5.8
11	0.546	1.4	6.0	27	6.58	0.71	5.9
12	0.667	0.83	5.9	28	6.30	0.63	5.9
13	0.803	1.0	5.9	Core	9.19	0.65	5.9
14	0.987	0.30	5.8	1	9.29	0.22	5.8
21	0.531	0.86	5.9	2	9.66	1.1	5.9
22	0.661	0.85	5.9	3	9.35	0.31	5.8
23	0.804	0.46	5.9	4	9.59	0.42	5.8
24	0.976	0.30	5.8	5	10.0	0.43	5.8
Interface				6	10.1	0.28	5.8
1	4.21	0.53	5.9	7	9.62	0.10	5.8
2	4.26	0.10	5.8	8	9.43	0.23	5.9
3	4.91	0.13	5.8	11	9.45	1.7	6.1
4	5.07	0.10	5.8	12	10.0	0.14	5.8
5	5.21	0.58	5.9	13	9.54	0.10	5.9
6	6.11	0.94	5.9	14	9.72	0.21	5.8
7	6.45	0.26	5.8	15	10.2	0.14	5.8
8	6.10	0.11	5.8	16	10.2	0.78	5.9
11	4.19	0.36	5.8	17	9.88	0.13	5.8
12	4.40	0.95	5.9	18	9.36	0.46	5.9
13	5.08	0.73	5.9	21	9.53	0.59	5.9
14	5.22	0.10	5.8	22	9.70	0.10	5.8
15	5.78	0.49	5.9	23	9.50	0.13	5.8
16	6.26	0.32	5.8	24	9.72	0.29	5.8
17	6.64	0.17	5.8	25	10.2	0.10	5.8
18	6.31	0.10	5.8	26	10.4	0.57	5.9
21	4.20	0.42	5.8	27	9.73	0.10	5.8
22	4.39	1.2	6.0	28			

TABLE I.E.10. Absolute $^{27}Al(n,\alpha)^{24}Na$ and $^{238}U(n,\gamma)^{239}U$ Reaction Rates in ZPR-3 Assembly 61

	$^{27}Al(n,\alpha)^{24}Na$				$^{238}U(n,\gamma)^{239}U$		
Sample	Absolute Reaction Rate x 10^{14}, sec^{-1}	Relative Error, %	Absolute Error, %	Sample	Absolute Reaction Rate x 10^{15}, sec^{-1}	Relative Error, %	Absolute Error, %
Core				Blanket			
1	6.32	0.73	7.1	1	0.102	2.2	7.5
2	6.24	1.3	7.2	2	0.101	1.5	7.2
3	6.64	0.33	7.1	3	0.092	0.85	7.2
4	6.24	1.3	7.2	4	0.099	0.87	7.2
5	6.47	1.0	7.1	Interface			
6	6.69	0.41	7.1	1	5.83	1.3	6.1
7	6.98	1.4	7.2	2	5.46	1.6	6.1
8	6.51	0.75	7.1	3	4.50	2.5	6.4
11	6.37	1.0	7.1	4	4.05	1.4	6.1
12	6.36	1.0	7.1	5	4.02	1.6	6.1
13	6.94	1.1	7.2	6	3.93	2.3	6.4
14	6.72	2.3	7.4	7	4.14	1.8	6.2
15	6.68	2.9	7.6	8	4.24	1.5	6.1
16	6.85	0.68	7.1	Core			
17	7.23	0.73	7.1	1	4.87	0.95	6.7
18	6.65	0.75	7.1	2	4.80	1.3	6.8
21	6.41	2.9	7.6	3	4.66	2.4	7.0
22	6.50	1.1	7.2	4	4.63	2.7	7.2
23	6.77	1.6	7.2	5	4.89	1.5	6.8
24	6.53	0.27	7.1	6	4.92	1.1	6.7
25	6.56	0.68	7.1	7	5.01	1.2	6.7
26	6.93	0.99	7.1	8	5.10	1.9	6.9
27	7.04	2.1	7.4				
28	6.64	0.67	7.1				

PUBLICATIONS

EBR-II Fuel Handling System
  B. C. Cerutti, G. E. Deegan, E. Hutter, and J. B. Waldo
    Sodium-Cooled Fast Reactor Engineering, Proc. IAEA Symp.,
    Monaco, March 23-27, 1970. Int. Atomic Energy Agency, Vienna,
    1970, pp. 739-755

New Etchants for Irradiated Uranium Alloys
  D. M. Cheney
    Metallography 3(3), 371-374 (Sept 1970)

Symptoms and Detection of a Fission-product Release from an EBR-II
Fuel Element. Case 2. Defect below Fuel Elevation
  R. M. Fryer, R. R. Smith, E. R. Ebersole, and R. V. Strain
    ANL-7676 (June 1970)

Experiments with a Series of Small, Pu-plus-U-fueled Fast-reactor
Criticals (FARET Mockup--ZPR-3 Assembly 46)
  A. L. Hess, W. P. Keeney, and R. L. McVean
    ANL-7215 (Jan 1970)

An Extended Equivalence Relation
  C. N. Kelber
    Nucl. Sci. Eng. 42, 257-259 (Dec 1970)

EBR-II Codes for Processing Reactivity Data at Full and Reduced Coolant
Flows
  J. K. Long and E. M. Dean
    ANL/EBR-020 (May 1970)

II. GENERAL REACTOR TECHNOLOGY

A. Applied and Reactor Physics Development

1. Nuclear Data

    a. Cross-section Measurements (C. E. Crouthamel and N. D. Dudey) (189a 02-082)

    (i) Spectrum-averaged Measurements

    Last Reported: ANL-7737, pp. 105-108 (Aug 1970).

    Determination of capture-to-fission ratios (alpha) for samples of fissile and fertile materials irradiated in EBR-II are nearing completion. Preliminary results for ^{233}U, ^{235}U, ^{238}U, ^{239}Pu, and ^{240}Pu have been previously reported. (See Progress Reports for October 1969 and August 1970, ANL-7632, p. 100, and ANL-7737, p. 108.) Minor corrections of the fission rates for contributions from isotopic impurities have now been made, and the errors associated with each sample have been evaluated. These calculations complete the determinations of alpha for ^{233}U, ^{235}U, ^{238}U, ^{239}Pu, and ^{240}Pu.

    The analytical problems associated with the determination of the capture rates of the ^{242}Pu samples were discussed previously (see ANL-7737), and a possible method for circumventing these problems was outlined. This procedure involved (1) chemically separating americium and allowing ^{243}Am (the daughter product of neutron capture by ^{242}Pu) to reach equilibrium with its daughter product, ^{239}Np; and (2) radiochemically separating the neptunium and determining the amount of ^{239}Np by gamma counting. By this procedure, we were able to measure sufficient amounts of ^{239}Np to determine the capture cross sections for each ^{242}Pu sample. The final ^{242}Pu alpha results, as well as the uncertainties associated with each measurement, are now being computed. An ANL topical report is being prepared which will summarize all the alpha results and will give a detailed description of the experimental procedures.

    Foil-activation-rate measurements of six nuclear reactions have been completed for various locations in four critical-assembly mockups in ZPR-3 (Assemblies 60-63). Because the experimental determinations are largely in support of the EBR-II Project, these data are being reported under 189a 02-151. (See, for example, Progress Report for October 1970, ANL-7753, p. 92.) The scope of our program (189a 02-082) includes the analysis of the ZPR-3 activation-rate data in terms of spectrum-averaged cross sections and experimentally derived flux and spectral quantities, and this work has been started. As these results become available, they will be reported under this program. The fission-yield data obtained in the ZPR-3 experiments will continue to be reported under 189a 02-083.

(ii) Yields of Low-Mass Fission Products

Last Reported: ANL-7742, p. 96 (Sept 1970).

Tests of the radiochemical procedure for separating tritium from all other fission products are continuing. The procedure involves exchanging the tritium with hydrogen carrier gas in a closed gas-handling system, pumping the tritium and hydrogen through a silver-palladium valve, and collecting and counting the tritium in an internal gas proportional counter. The testing has involved separation of tritium from thermally irradiated samples of ^{235}U, for which the tritium yield is known. Evaluation of these tests indicate that all the tritium is being removed from the samples and exchanged with the carrier gas; however, difficulty has been experienced in pumping the tritium quantitatively through the valve. In an attempt to solve this problem, the system is being modified to trap on charcoal all the gas that passes through the valve. The greatly decreased pressure behind the valve should, in principle, increase the transmission rate and thus the efficiency of the separation.

The samples of ^{233}U, ^{235}U, and ^{239}Pu previously irradiated in the Dynamitron (see Progress Report for September 1970, ANL-7742) will not be analyzed for tritium until the problems associated with the gas-handling system have been resolved. However, the monoenergetic neutron irradiations of fissile material are continuing so that samples will be available when the equipment is fully prooftested.

A second irradiation of ^{233}U, ^{235}U, and ^{239}Pu samples is currently scheduled in the Applied Physics FNG accelerator. The neutron flux obtainable on the FNG is only about one-fifth that of the flux obtained in the previous Dynamitron irradiation; however, by irradiating for a longer period of time (approximately 150 hr), it is estimated that 1-2 dpm of tritium will be produced in each sample. (The change in arrangements for the irradiations was brought about by budgetary considerations.) In the FNG irradiation, as in the Dynamitron irradiation, gram quantities of each of the three fissile materials will be irradiated simultaneously, together with gold monitor foils and fission-track recorders, at three different neutron energies (620, 700, and 760 keV).

Before the samples are analyzed for tritium, they will be counted on Ge(Li) detectors to measure the fast-fission yields of the more abundant short-lived fission products such as ^{140}Ba, ^{95}Zr, ^{103}Ru, ^{131}I, and ^{132}Te. The yields of longer-lived fission products such as ^{137}Cs may be obtainable after radiochemical separations; these analyses will be performed after the tritium separations are completed. The fission-yield work is being done in cooperation with the fast-neutron fission-yield program (189a 02-083).

B. Reactor Fuels and Materials Development

1. Fuels and Claddings

    a.   <u>Chemistry of Irradiated Fuel Materials</u> (C. E. Crouthamel and C. E. Johnson) (189a 02-087)

    (i)   <u>Post-irradiation Studies of Reactor Fuels and Cladding</u>

        Last Reported: ANL-7753, pp. 118-120 (Oct 1970).

Because molybdenum has been found in a variety of locations in irradiated fuels, its behavior is of particular interest in studies of the changes that occur in a fuel during irradiation. Electron-microprobe analyses of the radial distribution of molybdenum in metallic inclusions in an oxide fuel were reported previously (see ANL-7753). The fuel specimen studied (F2R) was a pellet fuel of UO_2-20 wt % PuO_2 (95% of theoretical density) that had been irradiated to 6.5 at. % burnup.

Recent studies have been directed toward examining the radial distribution of molybdenum in the oxide matrix of this same fuel specimen (F2R) and in the oxide matrix of a vibrapacked UO_2-20 wt % PuO_2 fuel. The latter fuel (SOV-1) had a smear density of 80% and a burnup of 5 at. %. Measurements of molybdenum were made in contiguous areas (80 by 80 μm) of the matrix across the radius of each fuel. These data are given in Fig. II.B.1, where the relative molybdenum concentrations are plotted against fractional radius of the fuel. Attempts were made to exclude all metallic inclusions from analysis, but this was virtually impossible for F2R. In Fig. II.B.1, the peak at 0.4 fractional radius is due to the large number of metallic inclusions found at this radial position in the fuel cross section. In SOV-1, the inclusions were more widely dispersed and, in general, could be excluded from the analysis.
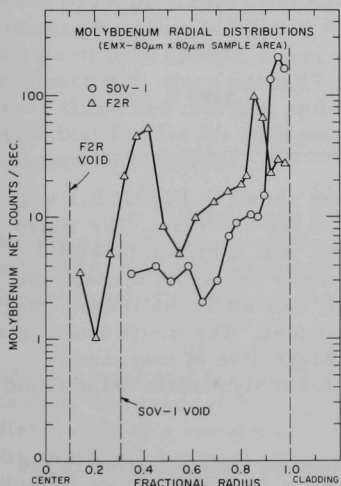

Fig. II.B.1

Radial Distribution of Molybdenum Oxide in the Matrix of UO_2-20 wt % PuO_2 Fuels (F2R and SOV-1). (The peak at 0.4 fractional radius for the F2R fuel is due to metallic inclusions.)

The presence of molybdenum in the oxide matrix has prompted an investigation of the species that could contribute to the vapor transport of molybdenum through the matrix. Initially, consideration has been given only to simple oxide species.

Calculations were made of the vapor pressures of these species using (1) oxygen-activity data for a 5 at. % burnup fuel derived from a model by Rand and Markin and (2) data on the free energy of formation of the various molybdenum species.* The following reaction was considered:

$$Mo(s) + xO_2(g) \rightleftharpoons MoO_{2x}(g).$$
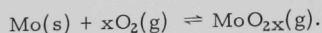
Calculations of vapor pressure were made at 3000 and 2300°K, the estimated temperatures for the hot and cold ends, respectively, of the columnar grain region. These data, given in Table II.B.1, indicate that MoO_2 has the greatest vapor pressure at both temperatures, thus indicating the potential for vapor phase transport of MoO_2 in the fuel.

TABLE II.B.1. Vapor Pressure of Molybdenum Species

Molybdenum Species	Vapor Pressure (atm) at Indicated Temperature	
	3000°K	2300°K
Mo	1.00×10^{-4}	4.68×10^{-8}
MoO	2.25×10^{-5}	1.05×10^{-9}
MoO_2	2.28×10^{-4}	3.78×10^{-7}
MoO_3	6.41×10^{-6}	1.93×10^{-8}

The distribution of molybdenum shown in Fig. II.B.1 suggests a vapor phase transport of molybdenum to the cladding. The sharp peak at 0.83 fractional radius for F2R coincides with a circumferential crack found at this location. The blocking of vapor transport through the unrestructured zone to the cladding is probably caused by the lesser interconnected porosity of this higher-density pellet fuel. The molybdenum distribution for the lower-density SOV-1 fuel is suggestive of increased interconnected porosity, which would account for molybdenum being found in large concentrations near the cladding wall.

The large increases in molybdenum concentration in the peripheral areas of the fuel may also indicate a corresponding change in the oxidizing potential in these fuels, which may reflect the nonequilibrium state that exists between the fuel center and the peripheral regions of the fuels. This nonequilibrium state would result from vapor transport that occurred predominantly toward the cooler end of the thermal gradient.

---

*JANAF Thermochemical Tables, Dow Chemical Co., Midland, Mich. (1965).

2. Coolants, Moderators, and Control Materials

    a. Sodium Impurity Analysis and Control (189a 02-156)

        (i) Establishment and Operation of a Sampling and Analytical Standards Program (R. J. Meyer, F. A. Cafasso, M. H. Barsky, H. S. Edwards, L. E. Ross, S. B. Skladzien, and M. D. Adams)

Argonne National Laboratory has the responsibility of certifying sampling and analytical methods for use throughout the sodium-technology program. The short-range goal is a set of interim standard methods, selected from existing technology, which will be uniformly applied at all sites participating in the program. To this end, an Analytical Standards Laboratory has been established, whose function is to manage the analytical standards program, as well as to participate in it. Plans for standardizing methods for FFTF and EBR-II and for nonreactor laboratories are being implemented.

To aid ANL in implementing the standards program, two advisory groups--representing the reactor and the nonreactor laboratories--were organized, and meetings of each group were held. As a result of the meetings, it was concluded that many of the same methods met the requirements of both groups, although additional methods, e.g., determination of radioactivity, were needed by the reactor laboratories. The two groups were therefore merged, and a manual of methods is now being prepared by ANL that fulfills the current analytical needs of both the reactor and nonreactor laboratories.

Plans are proceeding for a sample-interchange program among participants from the reactor group. Arrangements have been made with EBR-II to supply samples of sodium for oxygen, carbon, hydrogen, and trace-metal analyses for the sample-interchange tests.

Recent laboratory work has been directed primarily toward procurement and assembly of apparatus for determining oxygen, hydrogen, carbon, and trace metals. The procedure for trace-metal analysis involves distillation of a sample of sodium and emission-spectrographic analysis of the residue. A test of the procedure using a sample of EBR-II sodium showed good agreement between the emission-spectrographic analysis and results of atomic-absorption spectrographic analyses reported by EBR-II.

Work has also begun to establish a procedure for characterizing particulate matter in sodium. Filters from operating sodium loops are being used to test the procedure, which involves distillation of excess sodium from the filter and subsequent examination of the particulate matter by microscopic and X-ray diffraction techniques.

64

(ii) Characterization of Cold-Trapped Sodium (J. T. Holmes and C. C. McPheeters)

Last Reported: ANL-7742, p. 107 (Sept 1970).

The primary goal of this work is the determination and interpretation of nonmetallic impurity levels in cold-trapped sodium as a function of cold-trap operating parameters and procedures. The methods for determining the impurities (O, C, H, and N) in the sodium will be on-line impurity monitoring, and sampling and analysis. Experimental work will be carried on in a pumped-sodium apparatus that will provide stable but adjustable impurity levels in the sodium fed to the test cold trap. A work plan has been approved and is being implemented for the design and construction of the Apparatus for Monitoring and Purifying Sodium (AMPS). Target date for startup of AMPS is mid FY 1972. Data for both transient and steady-state operation of the test trap will be correlated with cold-trap parameters and the feed composition.

A detailed equipment layout has been prepared for installing two oxygen meters and one hydrogen meter on the outlet of the EBR-II primary cold trap. These meters will be used in conjunction with meters to be installed on the Radioactive Sodium Chemistry Loop (RSCL) of EBR-II for characterizing the operation and efficiency of the primary cold trap.

(iii) Method for the Determination of Metal and Halide Impurities in Sodium (R. J. Meyer and H. S. Edwards)

Last Reported: ANL-7742, pp. 107-108 (Sept 1970).

A survey method is needed for the rapid and routine determination of changes in metallic impurity levels in sodium. The method selected for further evaluation was emission spectrocopy using induction-coupled plasma excitation of a metal-dust aerosol formed by ultrasonic nebulization of molten sodium. Recent work has involved testing of components and assembly of an integrated setup for performing the necessary experimental measurements. Further work on this method has been deferred, however, because of budgetary limitations.

(iv) Reference Methods for the Determination of Oxygen, Carbon, and Nitrogen in Sodium (R. J. Meyer, M. D. Roche, and L. E. Ross)

Last Reported: ANL-7742, p. 108 (Sept 1970).

Several experiments have been conducted to provide data for further evaluation of proton-activation analysis for the determination of total oxygen in sodium. A combined sampling and irradiation cell has

been used to obtain two samples from a sodium loop and to irradiate them in a well-stirred molten state. Results indicated that interference from other induced activities could be either adequately controlled or circumvented and that the sensitivity for oxygen attainable in this cell approaches 1 ppm. A new cell has been designed to provide an improvement in the signal-to-background ratio and in the counting geometry; this cell is expected to increase the sensitivity of the oxygen analysis to 0.1 ppm. Further work on proton-activation analysis is being deferred because of budgetary limitations.

3. Radiation Damage on Structural Materials

    a. In-reactor Creep Studies (189a 02-091)

        (i) A Simulation of In-reactor Test Conditions Using Cyclotron Bombardment (S. D. Harkness, F. L. Yaggee, and J. Styles)

        Last Reported: ANL-7758, pp. 74-75 (Nov 1970).

A uniaxial creep test has been performed during 22-MeV-deuteron bombardment on a sample of Type 304 stainless steel previously irradiated in EBR-II to a total dose of 8×10^{21} n/cm^2 at 460°C. The purpose of the test was to determine the effect of fluence on the in-reactor creep properties. The conditions of the test were designed to duplicate those used for a previously unirradiated (virgin) sample, as reported in ANL-7758, pp. 74-75. As shown in Table II.B.2, irradiation in EBR-II reduced the creep rate from 2.5×10^{-4} to 1.1×10^{-5} hr^{-1}. This reduction is apparently due to the hardening of the microstructure by the radiation-produced voids and dislocation loops.

TABLE II.B.2. Results of Simulation of In-pile Creep of Type 304
Stainless Steel using 22-MeV-deuteron Bombardment

EBR-II Dose, 10^{21} n/cm^2	Deuteron Current, μA	Stress, psi	Temperature, °C	Length of Test, hr	Correlation Parameter	Strain Rate, hr^{-1}
0	2.2 ± 0.1	66,400	372 ± 5	13.2	0.96	2.5×10^{-4}
8	2.25 ± 0.05	65,700	390 ± 3	21.8	0.98	1.1×10^{-5}

The stress level used in the test (~66,000 psi) is well above the yield stress of the virgin sample but below the yield stress (75,000 psi) of the EBR-II irradiated specimen.

4. Techniques of Fabrication and Testing

a. Nondestructive Testing Research and Development (189a 02-092)

(i) Development of High-temperature, Radiation-resistant Ultrasonic Transducers (K. J. Reimann)

Last Reported: ANL-7742, pp. 111-112 (Sept 1970).

Although the experiments previously suggested in ANL-7742, pp. 111-112, to improve the brazing characteristics of lithium-niobate piezo-electric crystals were unsuccessful, good brazes have been achieved with an air-braze technique. Air brazing is a logical consequence of the concept of increasing the oxygen pressure to avoid outdiffusion of oxygen from the crystal. A repeatable procedure for the air-brazing operation has been established. The bonding material on the crystal surfaces consists of two baked-on layers of a palladium-platinum-gold paste, subsequently cleaned to remove the organic residue of the vehicle. The baking temperature is kept slightly above the melting point of the brazing material to prevent outgassing during the brazing operation. In a single operation, the lead wire is air-brazed to the crystal and the crystal to the supporting structure.

Several experimental transducers were constructed and are ready for evaluation. Of special interest are the frequency response, the effects of brazing on the frequency response, and changes occurring at elevated temperatures. A special capacitive probe, with air as the dielectric, will serve as reference receiver in the calibration procedure and at the same time be evaluated as an alternate approach to the high-temperature concept. Preliminary results confirmed that the sensitivity to periodically pulsed ultrasonic waves with time and constant supply voltage did not change, as was observed in capacitive transducers with solid dielectrics. The use of Teflon insulators will lower the high-temperature limit of this special probe.

To evaluate the feasibility of failure prediction by means of acoustic emission, a brazed, lithium-niobate transducer is being mounted by means of an extension rod to a stainless steel tension specimen that will be subjected to stresses at 593°C.

(ii) Proton Radiography (H. Berger and N. P. Lapinski)

Not previously reported.

An investigation of proton radiography has been initiated with 11-MeV protons from the ANL cyclotron. The attenuation characteristics of monoenergetic charged particles provide a potential advantage to radiography because most of the attenuation of the charged-particle beam occurs in the small increment of thickness near the end of the particle range.

Transmission characteristics of monoenergetic protons offer the potential to observe appreciably smaller variations of thickness than can be observed by X-radiography.

Initial experiments have been concerned with an evaluation of several image-detection methods, including Polaroid film, X-ray and color film, plastic track-etch materials, activation autoradiography, and phosphor screen-television. Detector-evaluation studies have yielded useful approximations of the proton exposure required for an observable image. These data are now being refined, and contrast measurements are being studied. Contrast evaluations have been hampered by the nonuniform beam area (now about 5-cm diameter), which makes measurements of density and calculations of ultimate contrast difficult. Attempts are being made to improve beam uniformity.

5. <u>Engineering Properties of Reactor Materials</u>

    a. <u>High-temperature Properties of Ceramic Fuels</u> (189a 02-094)

       (i) <u>Plastic Yielding and Fracture of Mixed Oxides</u>
          (J. T. A. Roberts and B. J. Wrona)

Last Reported: ANL-7753, pp. 126-128 (Oct 1970).

A number of UO_2-20 wt % PuO_2 bars (96% TD, grain size $\approx 2\ \mu$, O/M = 1.97 ± 0.005) were tested in four-point bending at strain rates of 0.085-0.75 hr^{-1}. The influence of strain rate on the strength 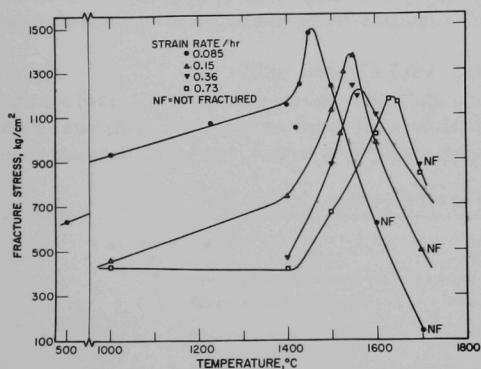and brittle-to-ductile transition T_c is shown in Fig. II.B.2. T_c coincides with the temperature at which maximum strength is measured, and increases as the strain rate increases.

Above T_c, the strength decreases continuously, and at $\sim T_c + 100°C$, the specimens are fully plastic and deform to the limit of the extensometer arrangement (3-5% outer fiber strain) without fracturing.

Fig. II.B.2. Influence of Temperature and Strain Rate on Fracture Stress. Neg. No. 53744.

Increasing the strain rate reduces fracture toughness below T_c (see Fig. II.B.3). Crack nucleation, therefore, plays no part in the fracture; the important process is crack propagation, presumably from preexisting surface flaws. The hardening
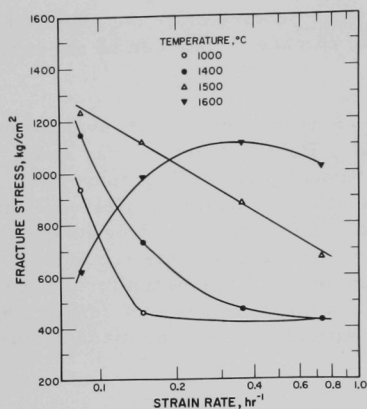
Fig. II.B.3. Influence of Strain Rate on Fracture Stress. Neg. No. 53743.

effect of strain rate observed at $\geq 1600°C$ is not physically significant, because it corresponds to a temperature region where the specimen tested at the low strain rate is fully plastic; the specimen tested at the highest strain rate is brittle.

The increase in strength with an increase in temperature, particularly in the temperature region 1400°C to T_c, cannot be explained by the Griffith criterion for fracture. Congleton et al.* have demonstrated that a similar large temperature dependence of strength in Al_2O_3 was due to crack propagation by means of plastic deformation. Although no obvious signs of plastic deformation (river lines) appeared on the fracture surfaces of UO_2-20 wt % PuO_2 (see Progress Report for September 1970, ANL-7742, p. 114), it is possible that plastic blunting of cracks does occur. In material with "ultrafine" grain size, however, one alternative to "dislocation blunting" is "grain-boundary blunting." A crack moves only a short distance $(1-2 \mu)$ before reaching a grain boundary. In the temperature region where grain-boundary weakness begins, localized grain-boundary sliding could impede fracture and result in material strengthening.

---

*J. Congleton, N. J. Petch, and S. A. Shiels, Phil. Mag. 19(8), 795 (1969).

C. Engineering Development

1. <u>Instrumentation and Control</u> (T. P. Mulcahey) (189a 02-096)

New and unique instrumentation is being developed to diagnose performance and detect abnormalities in LMFBR cores. Included are sensors and techniques for acoustical detection of sodium-coolant boiling, monitoring of flow-rate-related phenomena that could detect imbalances between cooling and power, and the measurement of vibrations that might disturb overall reactor stability.

a. <u>Boiling Detector</u> (T. T. Anderson)

(i) <u>Acoustic Method</u>

(a) <u>Irradiation and Resistance Tests on Piezoelectric and Insulator Materials</u> (T. A. Mayer)

Last Reported: ANL-7758, p. 82 (Nov 1970).

Preparations are being made to irradiate lithium niobate crystals in the CP-5 reactor. Because ^6Li offers a large cross section to thermal and epithermal neutron flux, neutron damage can vary with variations of isotopic abundance in the crystal. Accordingly, sample boules of lithium niobate were procured from commercial vendors for determination of the ratio of $^6Li/^7Li$ isotopic composition. Chemical procedures for converting niobate for analysis were established, and the ratio was determined by mass spectrometry in the ANL Chemistry Division.

The results (see Table II.C.1) show that the samples have close to naturally occurring isotopic abundance; however, they offer no assurance that future feedstock of lithium carbonate to produce the niobate will have the same isotopic composition.

TABLE II.C.1. Isotopic Ratio in Commercial Lithium Niobate

Vendor	Sample Boule No.	$^6Li/^7Li$ Ratio
Crystal Technology, Inc.	4-104	0.0817
Crystal Technology, Inc.	9-137H	0.0821
Clevite	571-979	0.084
Union Carbide	None Supplied	0.085
Isomet Corp.	RB-225	0.0809
Isomet Corp.	R228-68	0.082
Isomet Corp.	R228-68	0.082
Harshaw	863-302-90	0.0819
Normal Li Std.		0.0809

(b) Development of High-temperature Detector
(A. P. Gavin)

Last Reported: ANL-7753, p. 128 (Oct 1970).

High-temperature acoustic pressure sensors fabricated and tested to date have exhibited a decrease in electrical resistivity with increasing temperature, which is in excess of predictions from published values of resistivity of lithium niobate. This reflects difficulties in measuring sensor output at temperatures above 1000°F.

Three possible causes of the decrease in resistivity are being investigated. The first is the type of high-temperature coaxial cable used. Electrical leads for all sensors fabricated thus far have consisted of 3-ft lengths cut from a single piece of MgO-insulated coaxial cable. Therefore, a 3-ft length of this cable and a similar length of high-quality Al_2O_3-insulated cable were vacuum-dried in an oven and then placed in a calibration furnace. At room temperature, the resistance of the Al_2O_3-insulated cable was 10^{10} Ω, compared to 10^{13} Ω for the MgO-insulated cable. At 1200°F, both cables had the same resistance, 1.2×10^8 Ω. Since the resistance of the experimental sensors is less than 10^6 Ω at 1200°F, the cable is not considered a major contributor to the problem.

The second possible cause for decreased resistance is breakdown of the cable insulation at the housing-to-sheath weld. This region has been redesigned, and a housing-cable assembly incorporating the new design has been furnace-tested. At 1200°F, the resistance was 2.6×10^7 Ω, which should be sufficient for good sensor operation.

The third possible cause for decreased sensor resistance is an abnormal change in resistivity of the lithium niobate crystal. To check this possibility, an apparatus was designed and constructed to measure crystal resistance in the furnace. The first set of measurements was made on crystals from sensor HT 5-1. This sensor had been previously cycled several times to temperatures above 1000°F, and the crystals exhibited a brownish discoloration. At room temperature, the resistance was 3×10^8 Ω, compared to 2×10^{14} Ω for a control crystal from the same lot.

To determine if this loss of resistance was due to oxygen depletion, one of the crystals from sensor HT 5-1 was installed in the apparatus and heated in air to 1200°F. At that temperature, the resistance was 4×10^5 Ω. When the crystal cooled to room temperature, the resistance was 20 times that of the other crystal from sensor HT 5-1. Also, most of the brownish discoloration was no longer visible.

A new sensor has been fabricated and will be tested in an atmosphere of pure oxygen at a pressure of 150 mm Hg.

2. Heat Transfer and Fluid Flow (M. Petrick and R. P. Stein)
   (189a 02-097)

Analytical and experimental investigations of liquid-metal heat transfer and fluid flow in components and systems are conducted to provide information of immediate interest to the FFTF and LMFBR Programs. Fundamental studies in heat transfer and fluid flow also are conducted to improve current, or to devise new, engineering prediction methods essential to the advancement of reactor technology in general.

a.   LMFBR Flow Stability Studies (M. Petrick and R. Rohde)

This activity covers (1) the acquisition and analysis of experimental data on the vaporization and superheating of sodium in operating ranges (pressures, flow rates, temperatures, and equivalent diameters) and flow circuits of interest to the LMFBR Program; and (2) the determination, by both experiment and analysis, of two-phase flow phenomena related to flow stability. An LMFBR Simulation Heat Transfer Loop is being constructed for the experiments.

(i)   Preparation of Apparatus

Last Reported: ANL-7758, pp. 83-84 (Nov 1970).

The status of construction of the LMFBR Simulation Heat Transfer Loop is as follows: Leak-detection material, insulation, and thermocouples have been installed on the piping between the preheater and upper portion of the plenum.

Racks for loop control instrumentation were assembled and installed, with flexible conduit to facilitate access to the loop enclosure. Panel meters, switches, warning lights, and other equipment controls are being installed. Wiring for the high-voltage ammeter in the electron-bombardment circuit has been installed in conduit.

b.   Electron Bombardment Heater (EBH) Development
     (R. D. Carlson)

Electron-bombardment (EB) heaters are being developed to supply heat fluxes greater than 1.5×10^6 Btu/(hr)(ft^2) to liquid metals. Current effort is directed toward EB pin-type heaters that are prototypical of reactor fuel pins and that can be used to simulate these pins in various heat-transfer and reactor-safety experiments. Such heaters ($1/4$-in. OD x 24 in. long) have supplied heat fluxes up to 2.3×10^6 Btu/(hr)(ft^2) to water.

(i) Preparation of Single Pin (1/4-in. OD x 36 in.)
(J. J. Carey)

Analytical techniques have been applied to determine the proper cathode diameter, tension, and unsupported length for a 1/4-in.-OD x 36-in.-long EB-heated pin. These analy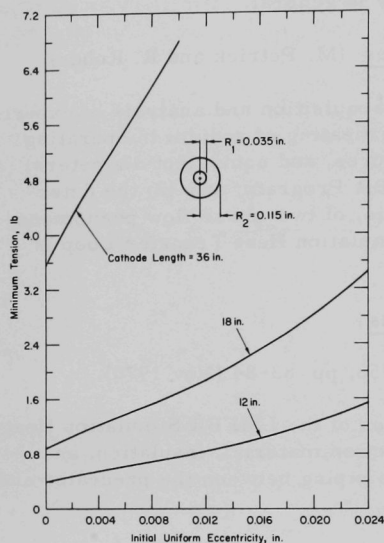ses show that for a cathode of a given diameter and length under some applied voltage, a minimum tension $(T_0)_{min}$ is required to maintain stability. This minimum tension (in pounds) corresponds to the applied tensile load T_0 at which the cathode becomes unstable due to some small disturbance. For $T_0 \leq (T_0)_{max}$, a small disturbance will lead to oscillations of increasing amplitude and eventual contact with the anode. Therefore, in practice, the applied tensile load must be greater than the minimum load. Figure II.C.1 shows a typical plot of $(T_0)_{min}$ versus initial eccentricity for a 0.070-in.-dia cathode at 6 kV.

Fig. II.C.1. Maximum Tension vs Initial Uniform Eccentricity for 12-, 18-, and 36-in.-long Cathodes

Creep-rupture data for tungsten was used to determine $(T_0)_{max}$, the maximum tensile load which will give a time to rupture of 10,000 hr, or a useful life of 1000 hr at 2250°C. At that temperature, the applied tensile load T_0 must satisfy $(T_0)_{min} < T_0 < (T_0)_{max}$. Table II.C.2 shows maximum and minimum tensile loads for various cathodes at 4 and 6 kV. These values were determined by treating the cathode as a cable. In each case, it was assumed that the cathode was perfectly centered (i.e., no initial eccentricity). The effect of initial eccentricity can be determined from Fig. II.C.1.

Table II.C.2 shows the dependence of $(T_0)_{min}$ on the unsupported length of the cathode. For the 36-in.-long, unsupported cathodes operating at 6 kV, $(T_0)_{min}$ exceeds $(T_0)_{max}$. Thus, if the minimum tension values are applied to provide stability, the cathodes probably will fail due to creep before the useful life of 1000 hr is reached. However, if each cathode is supported in the center, yielding two 18-in.-long cathodes, then $(T_0)_{min}$ is much less than $(T_0)_{max}$, which is the condition required for a successful cathode.

TABLE II.C.2. Tension Requirements for Cathodes
Treated as Cables

D, in.:	0.060			0.070			0.080		
L, in.:	12	18	36	12	18	36	12	18	36

Operating Voltage: 4 kV

$(T_o)_{min}$	0.13	0.30	1.18	0.17	0.39	1.55	0.39	0.88	3.52
$(T_o)_{max}$	2.42	2.42	2.42	3.38	3.38	3.38	4.32	4.32	4.32

Operating Voltage: 6 kV

$(T_o)_{min}$	0.30	0.66	2.65	0.39	0.87	3.48	0.51	1.14	4.55
$(T_o)_{max}$	2.42	2.42	2.42	3.38	3.38	3.38	4.32	4.32	4.32

Cathodes with diameters and lengths considered here have considerable stiffness; therefore, a beam model provides more accurate results than the cable model. Table II.C.3 shows the corresponding values for a perfectly centered, simply supported beam. Where appearing, a negative value indicates that the wire is sufficiently stiff and requires no tensile load for stability. The values for an operating voltage of 6 kV indicate that an unsupported, 36-in.-long cathode has little chance for success; however, a cathode of shorter length should be successful. Accordingly, effort is being made to perfect a 36-in.-long, 0.070-in.-dia cathode which is supported in the center, and which the analysis predicts should be a mechanically stable configuration.

TABLE II.C.3. Tension Requirements for Cathodes
Treated as Beams

D, in.:	0.060			0.070			0.080		
L, in.:	12	18	36	12	18	36	12	18	36

Operating Voltage: 4 kV

$(T_o)_{min}$	-0.572	0.272	2.55	-1.226	0.152	3.30	-2.25	-0.085	4.24
$(T_o)_{max}$	2.42	2.42	2.42	3.38	3.38	3.38	4.32	4.32	4.32

Operating Voltage: 6 kV

$(T_o)_{min}$	-0.742	-0.088	1.083	-1.446	-0.328	1.37	-2.37	-0.345	3.21
$(T_o)_{max}$	2.42	2.42	2.42	3.38	3.38	3.38	4.32	4.32	4.32

3. Engineering Mechanics (G. S. Rosenberg) (189a 02-099)

Stress-analysis methods based on various continuum theories are developed to resolve reactor design problems that are not amenable to conventional engineering approximations or direct numerical computations employing general-purpose computer programs. Studies of structure-fluid interaction dynamics also are conducted to develop new methods of analysis and testing that can be used by designers to minimize the potential of detrimental flow-induced vibration of reactor components.

a. Structure-fluid Dynamics (M. W. Wambsganss, Jr.)

(i) Effect of Initial Curvature on Response of Tube in Parallel Flow (S. S. Chen)

Last Reported: ANL-7632, p. 122 (Oct 1969).

Analysis of the response of curved tubes to parallel flow has been completed;* however, the results are limited to tubes with small curvature. Since segments of tubes in advanced heat-exchanger designs will consist of U-bends with relatively large curvature, a more precise treatment of these segments is necessary. To the writer's knowledge, the only study of vibration and stability of a large, curved tube conveying fluid was published recently by Unny et al.** Unfortunately, the equation of motion derived is incomplete, and the results for fixed-fixed end conditions are erroneous.

The model studied here consisted of a curved circular tube of radius R, total angle ψ, mass per unit length m, effective flexural rigidity EI, and internal cross-sectional area A, conveying fluid of mass per unit length M, flowing at a constant velocity V and constant fluid pressure p. The equation of motion was derived to account for the fluid pressure, which was neglected in the paper by Unny et al. Tube stability was studied for fixed-fixed, hinged-hinged, and fixed-hinged end conditions.

It was observed that when the pressure or the flow velocity exceeded a certain value, the tube was subject to a buckling-type instability. The dimensionless generalized load was defined by

$$v = \frac{R^2}{EI}(MV^2 + pA).$$

The value of v that makes the system unstable was designated the generalized dimensionless critical load v_c.

---

*S. S. Chen and G. S. Rosenberg, Vibrations and Stability of a Tube Conveying Fluid, ANL-7762 (to be published).
**T. E. Unny, E. L. Martin, and R. N. Dubey, Hydroelastic Instability of Uniformly Curved Pipe-Fluid System, J. Appl. Mech. 37(3), 817-822 (Sept 1970).

Figure II.C.2 is a plot of v_c for fixed-fixed end conditions where $K = \psi/2\pi$. The mode shapes at instability for $K = 0.8$ are shown in Fig. II.C.3. Tube instability occurs in both symmetric and asymmetric modes. Also, the critical load decreases as the value of K increases. In the range $N < K < N + 0.44$ (N = positive integer), the critical loads for symmetric modes are lower than those for asymmetric modes. For other values of K, the loads for symmetric modes are higher. As K increases, the difference in magnitude of the loads for both modes becomes smaller.

Similar results were obtained for fixed-hinged, and hinged-hinged end conditions.
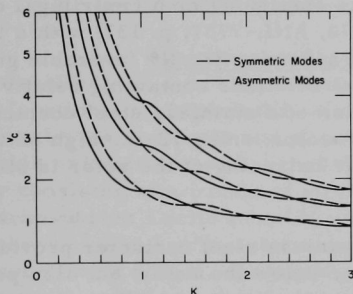
Fig. II.C.2

Generalized Dimensionless Critical Loads (v_c) under Fixed-Fixed End Conditions for Various Values of K
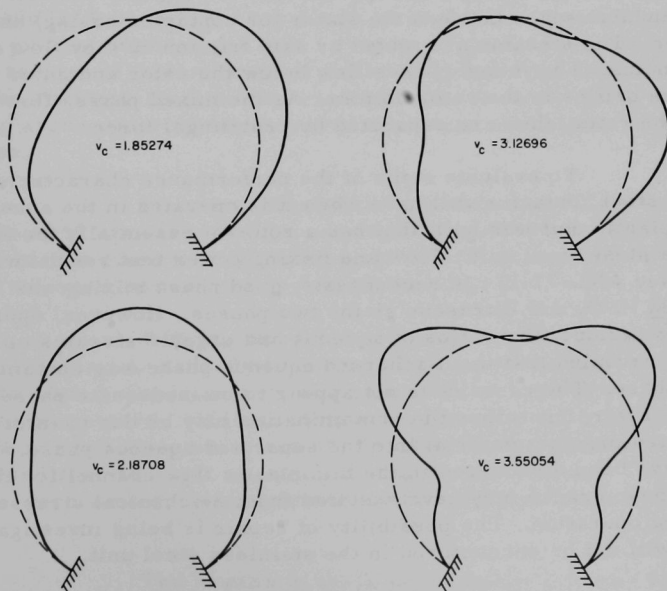

Fig. II.C.3. First and Second Asymmetric and Symmetric Mode Shapes for K = 0.8

D. Chemistry and Chemical Separations

1. Fuel Cycle Technology

a. LMFBR Reprocessing--Plutonium Isolation (D. S. Webster, A. A. Jonke, and G. J. Bernstein) (189a 02-159)

(i) Centrifugal Contactors for Plutonium Handling

Last Reported: ANL-7742, pp. 117-118 (Sept 1970).

Development work is continuing on a centrifugal contactor (see Progress Report for August 1970, ANL-7737, p. 137) with a large length-to-diameter ratio, which will have a critically favorable geometry for solvent extraction of LMFBR-fuel solutions containing relatively high plutonium concentrations. Fabrication of a stainless steel contactor with a 4-in.-ID hollow rotor, a $4\frac{3}{4}$-in.-ID stator, and a 12-in.-high settling zone is nearing completion. Dynamic balancing of the rotor is still to be done.

The design of the stainless steel contactor provides for mixing of phases in a mixing chamber below the rotor, but also permits the contactor to be modified by removal of the mixing paddle and mixing chamber. In the modified design, an aqueous- and an organic-feed stream flow into the annular space between the stator (or contactor casing) and the spinning rotor. The streams are mixed by skin friction as they flow downward in the annulus. The mixed phases flow below the rotor and enter the rotor through an orifice in the rotor bottom. As the mixed phases flow upward through the rotor, they are separated by centrifugal force.

To evaluate some of the performance characteristics the stainless steel contactor will have when it is operated in the annular mixing mode, a plastic unit was built that has a rotor of essentially the same size as the stainless steel unit. Flow and mixing power test results were reported earlier (see ANL-7742). In recent tests, good phase mixing was observed using $0.1\underline{M}$ HNO_3 and Ultrasene as the two phases. However, operation of the unit at various flow ratios of aqueous and organic streams up to 5 gpm total flow revealed that the discharged aqueous phase was contaminated with organic phase. The cause does not appear to be inadequate phase separation within the rotor, but rather the contamination may be due to internal leakage of separated organic material into the separated aqueous phase. Hairline cracks have been discovered in the thin plastic flow channel for the organic phase. These cracks may have resulted from mechanical stresses during high-speed operation. The possibility of repair is being investigated. This problem will not be encountered in the stainless steel unit.

b. <u>Molten Metal Decladding of LMFBR Fuels</u> (D. S. Webster)
(189a 02-173)

Laboratory and engineering work is being done to develop concepts for decladding stainless steel-clad LMFBR fuel elements and subsequently reducing the fuel to metal. The concepts are expected to be applicable also to the removal of Zircaloy cladding from light-water-reactor fuels.

(i) <u>Engineering Developments</u> (R. D. Pierce)

Last Reported: ANL-7758, p. 86 (Nov 1970).

(a) <u>Gas-release Experiments</u>. Experiments were made to observe the effects of a sudden release of gas under pressure from tubes at different locations in a simulated subassembly immersed in a liquid. The choice of water as the liquid and of some transparent components allowed the behavior of liquid to be observed during these experiments. The subassembly consisted of a bundle of simulated LMFBR fuel elements fastened inside a transparent Lucite tube ($2\frac{1}{2}$-in. OD, $1\frac{15}{16}$-in. ID, $37\frac{1}{8}$ in. long) simulating a shroud. The Lucite tube was open at the top, and its bottom was closed except for a $5/8$-in.-dia opening at the center. The simulated fuel elements consisted of two stainless steel tubes ($1/4$-in. OD by 37 in. long) crimped on the lower end (leaving an opening of about 0.004 in.^{2}), surrounded with 15 rods ($1/4$-in. OD by 37 in. long), each of which was wound with 48-mil wire at a pitch of one turn per foot. Venting of gas from the two tubes simulated the release of fission-product gas during zinc decladding. The upper ends of the stainless steel tubes were connected through valves to a manifold containing argon under pressure and having twice the volume of the stainless steel tubes.

In an experiment, the manifold was filled with argon at a pressure of 52 atm. The bottom end of the assembly was immersed 4 in. into a $4\frac{1}{2}$-in.-dia glass tank of water, and ~50 cm^3 of argon at 52-atm pressure was released through one or both of the tubes.

With the two tubes located over the opening in the bottom of the shroud, 2 in. of water was blown out of the tank when two tubes were vented simultaneously and 1 in. of water was blown out when a single tube was vented. When gas was vented from tubes located near the wall of the shroud, little water was blown from the tank, but the water level in the shroud rose to 31 in. when one tube was vented, and to 37 in. when both tubes were vented. Less displacement would be expected in a run with zinc.

The results of these experiments indicate that the height to which zinc will be forced up into a fuel subassembly or splashed inside a

decladding vessel during decladding will depend on the location of the ruptured fuel element in the subassembly and, to a large extent, on the rate at which fission gases are released from the fuel elements. No further experiments on the effects of gas release from mock fuel elements are planned.

(b) Reduction of UO_2 Pellets. Separation of fuel oxide from stainless steel cladding by a liquid-metal decladding step followed by reduction of the oxide to metal in the decladding vessel has been proposed. An advantage of this procedure would be that all volatile fission products would be released inside the decladding vessel and could be collected for storage undiluted by other gases.

In the proposed reduction step, fuel oxide pellets in a crucible are contacted with a liquid-salt phase and a molten-metal phase containing a reductant. With adequate mixing of the fuel oxide, salt, and metal, the uranium oxide and plutonium oxide are converted to metal and extracted into the molten-metal phase, which may then be pressure-siphoned out of the crucible. Alternatively, a salt-metal system may be used that causes the uranium to precipitate while the plutonium goes into solution. (See Progress Report for September 1968, ANL-7500, pp. 113-114.) In this case, an additional uranium dissolution step is required (e.g., by forming a liquid U-Fe alloy).

After the fuel (in solution in a large quantity of alloy) is removed from the crucible, it is dissolved in nitric acid for aqueous solvent-extraction processing. However, prior to acid dissolution, if the alloy contains volatile metals (e.g., magnesium and zinc), the alloy may be retorted to remove these volatile metals, which would then be recycled through the process.

It had been shown during development of the Salt Transport Process that a system consisting of calcium dissolved in Mg-42 at. % Cu and a $CaCl_2$-CaF_2 salt results in excellent reductions and would be feasible. Two Zn-Mg alloys are being evaluated as alternatives to this system in a limited number of runs: Zn-30 at. % Mg, which would give a product solution containing reduced uranium and plutonium; and Mg-20 at. % Zn, which would give a product solution containing only the reduced plutonium. Runs are being made with and without calcium added to the alloy to determine which systems would be acceptable alternatives to Mg-Cu-Ca.

Six experiments (Mg-Zn-R1 through Mg-Zn-R6) have been performed, using UO_2 pellets (0.21-in. diameter, 0.25 in. long) to study the reduction of UO_2. In Mg-Zn-R1, the charge was 1 kg of pellets, and the reduction step was performed in a baffled tungsten crucible ($10\frac{5}{8}$-in. ID and 19 in. high) equipped with an agitator. The charge for each of the experiments Mg-Zn-R2 to -R6 was 200 g of UO_2. Experiments Mg-Zn-R2 through -R6 were performed in an inductively heated tilt-pour furnace using a baffled

tungsten crucible ($5\frac{3}{4}$-in. OD, $5\frac{1}{2}$-in. ID, $13\frac{7}{8}$ in. high). A Mo-30 wt % W agitator (3-in. diameter, $1\frac{1}{4}$-in.-wide blade pitched 30° from horizontal, deflecting downward) was used to mix the melts at 900 rpm during reduction of UO_2, and at 600 rpm during dissolution of precipitated uranium. The reduction temperature was 800°C in all six experiments. Run durations were 5, 5, 1, 1, 5, and 6 hr for experiments Mg-Zn-R1 through Mg-Zn-R6, respectively.

The alloy charged in experiments Mg-Zn-R1 to -R3 was Mg-20 at. % Zn, and the salt was $MgCl_2$-47.5 mol % $CaCl_2$-5 mol % CaF_2. Reduction to uranium metal was nearly complete in these three experiments, although results of Mg-Zn-R3 indicate the possibility that unreduced UO_2 particles were sheathed in precipitated uranium metal.

In Runs Mg-Zn-R4 and Mg-Zn-R5, calcium was added to the Mg-Zn alloy and $CaCl_2$-20 mol % CaF_2 was used as the salt phase. This metal-salt system was selected to increase the reduction rate and to improve the efficiency of plutonium extraction in runs in which plutonium will be present. In Mg-Zn-R4, 3.39 kg of Mg-17 at. % Zn-4 at. % Ca alloy and 1.08 kg of the salt were charged; in Mg-Zn-R5, the charge was 3.55 kg of Zn-29 at. % Mg-6.6 at. % Ca and 1.08 kg of salt. In Mg-Zn-R6, $CaCl_2$-20 mol % CaF_2 was used as the salt and calcium was omitted from the alloy (Zn-30 at. % Mg).

The preliminary results now available indicate that good reductions of UO_2 pellets were obtained with Mg-17 at. % Zn-4 at. % Ca/$CaCl_2$-20 mol % CaF_2 and with Zn-29 at. % Mg-6.6 at. % Ca/$CaCl_2$-20 mol % CaF_2. However, in the final run, in which calcium was omitted, reduction of the UO_2 was unsatisfactory. Two to five more runs are planned to verify the good preliminary results obtained.

(c) Melt Decladding. A series of experiments has been started to investigate the separation of fuel oxide pellets and fines from stainless steel cladding by melt decladding (i.e., heating until the cladding melts and drains away from the fuel). The feasibility of this procedure depends upon sufficient exposure of oxide surface and sufficient draining of the stainless steel so that in the next step the oxide could be completely separated by either acid dissolution or voloxidation.

In each experiment, the charge was melted in a ceramic crucible held in a NRC high-vacuum induction furnace. A preliminary experiment was performed at 1600°C under vacuum (14 μm of Hg) with a 523-g charge of stainless steel. The product was a bright ingot that released easily from the crucible.

Five melt decladding experiments (SSMD-1 to -5) were performed with simulated LMFBR fuel elements. In SSMD-1 and -2, stainless steel tubes (0.25-in. diameter, 10-mil wall, 3-in. length) crimped closed

at one end were charged with UO_2 pellets (0.21-in. diameter, 0.25-in. length) and crushed UO_2 pellets (+14 mesh). A bundle of these UO_2-containing tubes was wrapped in 10-mil-thick stainless steel, which simulated a fuel sub-assembly shroud. The charges to the other three experiments were similar, except that oxide fines were omitted. In all experiments, the weight ratio of UO_2 to stainless steel was about 2 to 1.

The crucible used in SSMD-1 had six 1/16-in.-dia holes in its base and was positioned above a second magnesia crucible. Heating of the charge for 1.5 hr at 1460-1608°C under vacuum caused only 12% of the stainless steel to flow into the lower receiver. In this experiment and in subsequent experiments, the stainless steel wet the UO_2.

In SSMD-2 to -5, the furnace contained a single magnesia or Alundum crucible tilted at a 10° slope so that the molten steel would flow down the side to the bottom of the crucible and the pellets would remain on the wall above the steel. An argon atmosphere at an absolute pressure of ~630 Torr was maintained inside the furnace. Temperatures were ~1400 to 1650°C, and run times were 1 hr. Inspection of the contents of the crucibles after the experiments showed that flow of stainless steel was greater in magnesia crucibles and at higher temperatures. In all experiments, stainless steel had adhered to the oxide.

Experiments are planned in which the effects of a 20° slope of the crucible wall and of an Ar-4% H_2 atmosphere will be evaluated.

(ii) Process Demonstration Experiments (R. D. Pierce)

Last Reported: ANL-7753, p. 137 (Oct 1970).

(a) Irradiated Fuel Experiments. The first practice zinc-decladding run with the experimental equipment that will be used for demonstration of decladding and reduction of irradiated fuel has been completed, using nonirradiated stainless steel tubes containing UO_2 pellets. Steel was dissolved satisfactorily; however, observations made during this experiment suggested a few minor equipment modifications, which will simplify remote operation and which are now being made. A second practice run incorporating decladding and reduction steps is planned. If no serious operational problems are encountered in this run, the experimental apparatus will be installed in the Senior Cave, where one and possibly two cold experiments will be made before undertaking experiments with radioactive fuel.

A 2-in. section of stainless steel-clad irradiated UO_2-PuO_2 and several sections of highly irradiated stainless steel rods have been obtained for use in the hot experiments.

c.   <u>LMFBR Fuel Materials Preparation--U/Pu Nitrates to Oxides</u>
(A. A. Jonke and N. M. Levitz) (189a 02-157)

Last Reported: ANL-7758, pp. 87-88 (Nov 1970).

A continuous fluid-bed process for converting solutions of uranium-plutonium nitrate to oxide suitable for the fabrication of fuel shapes is being developed.

(i)   <u>Preparation of UO_2-PuO_2 Pellets.</u> Four $(U,Pu)O_2$ pellets (0.25-in. diameter, 0.1 to 0.3 in. long) were fabricated to explore briefly the effects of fabrication conditions on pellet density. The -100 mesh UO_2- 20% PuO_2 powder from which these pellets were made was prepared by drop denitration at 300°C (simulating the fluid-bed process) and hydrogen reduction of UO_3-PuO_2 to UO_2-PuO_2 at 500°C, as opposed to 550°C in earlier work (see ANL-7758). Two pellets were prepared by pressing at 87,000 psi; the other two pellets were first pressed at low pressures (~1500 psi), then granulated through a 45-mesh sieve, and finally pressed at 87,000 psi. Next, one pellet from each of the above pairs was sintered at 1650°C for 4 hr, and the other two pellets were sintered at 1750°C for 90 min; an argon atmosphere was used in all tests. Pellet densities ranged from 83 to 89% of theoretical. The pellet that had been prepressed, granulated, pressed at 87,000 psi, and sintered at 1750°C gave the highest density. Material reduced at the two different temperatures (500 and 550°C) and otherwise treated identically had the same final density (84% of theoretical). The results of these preliminary tests suggest that satisfactory $(U,Pu)O_2$ fuel pellets can be prepared by appropriate selection of pelletizing and sintering conditions.

(ii)   <u>Examination of UO_2-PuO_2 Pellets.</u> UO_2-PuO_2 pellets with a density 84% of theoretical, prepared as described above, were chemically analyzed, and were also physically examined with an electron microprobe (for homogeneity) and by X-ray diffraction. In the chemical analysis, oxygen content was determined by vacuum fusion, and the uranium and plutonium concentrations were determined amperometrically. The uranium, plutonium, and oxygen concentrations were 70.70, 17.60, and 11.75 wt %. The oxygen-to-metal atom ratio was 1.98, and the uranium-to-plutonium atom ratio was 4.0.

A pellet sample was examined by counting characteristic X-rays of uranium and plutonium with an electron microprobe. Counting data obtained for two different scanning procedures and by scanning several different areas of the pellet appeared to indicate good homogeneity. Trace stainless steel constituents that may have been picked up during sintering were identified in the pellet.

A lattice parameter of 5.4602 Å for the oxide was measured. Only a single set of diffraction lines was in evidence, indicating the presence of a single oxide phase. The measured lattice parameter was compared with the lattice parameter predicted from an earlier observed relationship between oxygen-to-metal ratio and lattice parameter at a stated plutonium content. (See Progress Report for April-May 1970, ANL-7688, pp. 214-215.) The value for a_0 predicted by that relationship is 5.4610 Å, which compares favorably with the experimental value.

(iii) Phase Stability of $UO_2(NO_3)_2$-$Pu(NO_3)_4$ Solutions. To increase the throughput of fluidized-bed reactors, the feed solution should be as concentrated as possible. In handling plutonium solutions, criticality considerations require an experimenter to avoid inadvertent precipitation of plutonium salts. Because of these requirements, it is necessary to know the cosolubility of $UO_2(NO_3)_2$ and $Pu(NO_3)_4$ in dilute nitric acid solution in order to choose a feed-solution composition with confidence that the solution is stable and is not unnecessarily dilute.

Little crystallization data are available in the literature for uranyl nitrate-plutonium nitrate solutions containing 20% plutonium. Cooling curves will therefore be used to determine the temperatures at which given solutions begin to crystallize, and from this information the practical limits of concentration of U/Pu nitrate solutions for feeds to the denitration process will be selected. Also, materials that crystallize from solutions of interest will be identified.

Standard equipment has been assembled that provides cooling of a stirred solution at a steady rate, while its temperature is measured with a thermocouple and recorded on a strip-chart recorder. Preliminary cooling-curve data obtained with this apparatus with uranyl nitrate solutions show good agreement with published data.

2. General Chemistry and Chemical Engineering

    a. Physical and Chemical Studies--Molten fuel, Cladding, and Coolant (A. D. Tevebaugh and M. G. Chasanov) (189a 02-175)

Last Reported: ANL-7742, pp. 123-125 (Sept 1970).

    (i) Reactor Materials--Fuel Phase Studies at High Temperature: Investigation of the Distribution of Fission Products among Molten Fuel and Reactor Phases (M. G. Chasanov)

Experiments are being carried out to determine the distribution of major heat-producing fission products among the various phases that would result from a meltdown of an LMFBR core.

A series of experiments is being continued in the arc-melting furnace and is designed to determine the distribution of La, Mo, Nb, Pr, Ru, and Y between molten iron and UO_2.

Distribution experiments are starting in a resistance-heated furnace to determine the distribution of La, Mo, Nb, Ru, and Zr between iron and a mixture of simulated fused concrete and UO_2. Zircon crucibles are satisfactory containers for these experiments at a temperature of 1550° C, and the experiments can be carried out in open containers under an atmosphere of helium in the resistance-heated furnace. One aspect of these experiments will be to estimate the solubility of UO_2 in fused concrete having a composition similar to that which will be used as a reactor liner in the FFTF.

3. Sodium Chemistry

    a. Sodium Chemistry and Radioactive Contaminant Behavior (189a 02-509)

    (i) Studies of the Sodium-Sodium Hydroxide, Sodium-Sodium Hydride, and Sodium-H_2O Systems (F. A. Cafasso and K. M. Myles)

Last Reported: ANL-7742, pp. 125-126 (Sept 1970).

This investigation seeks to understand the behavior of oxygen- and hydrogen-bearing species in liquid sodium. The results will be useful in developing and evaluating analytical methods for oxygen and hydrogen impurities in sodium. The effort to date has been directed toward the elucidation of the phase relations in the Na-Na_2O-NaOH-NaH system. Two tentative phase diagrams have been constructed.

Experimental verification and refinement of the actual diagram are under way. Room-temperature X-ray studies of carefully heat-treated alloys are expected to reveal the basic construction of the diagram. The required laboratory equipment for this work has been set up, and suitable techniques have been developed. A high-temperature Knudsen cell is being designed for the measurement of vapor species at elevated temperatures. The activities of oxygen and hydrogen in the various phase fields will be determined by the use of appropriate meters.

    (ii) Characterization of Carbon- and Nitrogen-bearing Impurities in Sodium (F. A. Cafasso and A. K. Fischer)

Last Reported: ANL-7742, p. 126 (Sept 1970).

Information on the existence, identification, and behavior of nitrogenous species in liquid sodium is needed to further the development of

methods for analyzing reactor sodium for nonmetallic species. The current experiments in this study involve (1) nitrogen absorption at 590°C by sodium and by Na-1 at. % Ca solutions in contact with Type 304 stainless steel and (2) nitridation of the stainless steel.

The results indicated that when sodium is present nitrogen uptake by Type 304 stainless steel occurs at the intersection of the liquid surface with the container wall and that the rate of nitrogen uptake is the same whether or not calcium is initially present in the sodium. The results also indicated that nitrogen is absorbed by sodium-calcium solutions and, to a lesser extent, by sodium with no added calcium; in the latter case, absorption is attributed to interaction of nitrogen with impurities in the sodium. The stoichiometry of the interaction of nitrogen with calcium was calculated to be $Ca_{1.78}N$.

Further experimental work in this program has been deferred because of budgetary limitations.

(iii) Solubility of Xenon in Liquid Sodium (F. A. Cafasso and E. Veleckis)

Last Reported: ANL-7742, p. 126 (Sept 1970).

The solubility of xenon in liquid sodium has been determined as a function of both temperature (350-600°C) and pressure (2-10 atm). This information will aid the implementation of current programs for the detection and location of fuel-element failures in future LMFBR systems. A total of 47 solubility determinations have been made at six temperatures. The mean Henry's law constants for the xenon solubility, expressed in ppb/atm (grams of gas dissolved in 10^9 g of sodium per atmosphere of gas pressure), are 90.0 (600°C), 37.9 (550°C), 17.4 (500°C), 6.56 (450°C), 3.06 (400°C), and 0.799 (350°C). The value calculated for the heat of solution of xenon in liquid sodium is 19.4 ± 0.8 kcal/mol. The results are in good agreement with those predicted by a theoretical model developed at ANL.*

No further work in this program is planned.

(iv) Evaluation and Control of Sodium Aerosol Problems (W. E. Miller and R. W. Kessie)

Last Reported: ANL-7742, p. 127 (Sept 1970).

The presence of sodium aerosol in the cover gas is expected to create problems at the higher operating temperature projected for future reactors. An assessment of these problems and a study of the properties of sodium aerosols are the goals of this program.

---

*H. C. Schnyders and H. M. Feder, Argonne National Laboratory, private communication.

Preliminary measurements have been made of the particle-size distribution of sodium aerosol in argon cover gas over sodium at 400°C. The measurements were made with a Casalla jet impactor. The amounts of sodium collected in the individual stages of the jet impactor were measured, and the mass mean diameter of the aerosol was determined to be ~4 μm; i.e., 50 wt % of the aerosol was present as particles having diameters less than 4 μm.

A calculational study has also been performed, in which the theory of nucleation has been applied to the tendency of sodium vapor to condense on nonsodium nuclei and ions, and to homogeneous nucleation. This study will aid in the understanding of sodium aerosol formation under various conditions.

Work on this program has been deferred because of budget limitations.

(v) Studies of Carbon Transport in Sodium-Steel Systems
     (K. Natesan, J. Y. N. Wang, T. F. Kassner, and
     C. A. Youngdahl)

Last Reported: ANL-7742, pp. 127-128 (Sept 1970).

An experimental program to elucidate reactions involving carbon transfer in ferritic and austenitic steels has proceeded in a number of areas. Additional information has been obtained on the distribution of carbon between sodium and iron-base alloy (viz., Type 304 SS, Fe-18 wt % Cr-8 wt % Ni, Fe-8 wt % Ni, and Fe-16 wt % Ni) foil specimens at 650 and 750°C. The results showed that the concentration of carbon in Type 304 SS is about a factor of 10 greater than that in the Fe-18 wt % Cr-8 wt % Ni alloy. The order-of-magnitude difference between the carbon concentrations in the two alloys has also been observed in equilibration studies conducted in Vycor capsules at 800°C. Minor alloying elements (e.g., Mn) and metallic impurities (e.g., Si, Ti, and Zr) in the commercial alloy apparently have an important effect on the total carbon content of these alloys at low carbon activities.

The activity of carbon in liquid sodium is being determined by equilibrating carbon in sodium with α-iron at temperatures below 723°C. Since carbon activity values in sodium-steel systems generally range between 0.01 and 0.1 (with graphite as the standard state), the carbon concentrations in α-iron are typically below 10 ppm. Internal-friction methods have been shown to be useful in determining the carbon concentration of iron-wire specimens at these low carbon levels.

Successful prediction of carburization-decarburization rates of materials in a reactor system will require the development of calculational methods as well as the determination of diffusion coefficients of carbon as

a function of alloy composition and temperature. An experiment to determine the diffusivity of carbon in an Fe-2.25 wt % Cr-1 wt % Mo alloy at 700° C by a steady-state method is in progress to obtain data on the diffusion coefficient as a function of carbon level in the alloy.

An investigation of the carburization and nitridation of steels by cyanide in sodium at 800° C has been completed. The distribution of carbon and nitrogen between an Fe-18 wt % Cr-8 wt % Ni alloy and sodium containing cyanide concentrations up to 37 ppm was determined. The results indicate that the nitridation potential of cyanide in sodium is about a factor of 10 greater than that for carburization at 800° C.

(vi) Definition of Radioisotope Problem Areas (W. E. Miller and W. J. Mecham)

Last Reported: ANL-7742, p. 128 (Sept 1970).

Program plans have been issued by Atomics International, General Electric, and Westinghouse for developing the technology required to solve the radioactivity problems associated with maintenance of LMFBRs. A similar program plan, "National Program for LMFBR Radioactive Repair Engineering," was issued by ANL in November 1970. The ANL plan emphasizes utilization of EBR-II. As a first step in the program, means must be found for measuring system contamination. This can probably best be done by insertion in the primary sodium system of removable surfaces, e.g., tabs, which would be examined for activity buildup during experiments in which activity is released. The feasibility of conducting suitable experiments is being evaluated.

(vii) Development of Radioisotope-Monitoring Methods (W. E. Miller and N. R. Chellew)

Last Reported: ANL-7742, p. 128 (Sept 1970).

Work is under way on three new concepts for monitoring the primary coolant of an LMFBR to yield information regarding the condition of fuel failures. These concepts are (1) on-line distillation of sodium to permit analysis of volatilized cesium and rubidium isotopes, (2) determination of ^{131}I in sodium by separating and counting its daughter ^{135m}Xe, and (3) determination of nonvolatile activities in sodium by assaying them after they are extracted into a lithium phase from which the sodium is continuously removed by distillation. The key problem in all three monitoring concepts is the separation of the activities to be monitored from the sodium activation product ^{24}Na, which is present at high levels in reactor sodium.

The current effort is directed primarily at obtaining information important to the successful operation of the second monitoring method. Equipment is being designed to obtain kinetic data on the removal of xenon activity (in this test, ^{133}Xe) from molten sodium.

PUBLICATIONS

Radioisotope Sources and Neutron Radiography
    J. P. Barton
        Chem. Eng. Prog. Symp. Ser. 66(106), 91-106 (1970)

Consideration of Standards for Neutron Radiography
    John P. Barton and M. F. Klozar
        Official Program, Am. Soc. Nondestructive Testing 1970 Fall Conf.,
        Cleveland, October 19-22, 1970; Mater. Eval. 28(9), 28A (Sept 1970)

Nuclear Physics and Nondestructive Testing: Some Applications and
Challenges
    H. Berger
        Bull. Am. Phys. Soc. 15, 1655 (Dec 1970)   Abstract

Vibration of a Beam with Motion-constraint Stops
    S. S. Chen, G. S. Rosenberg, and M. W. Wambsganss
        ANL-7619 (Mar 1970)

Ionizing Radiation Effects in Lithium Niobate
    W. Primak, T. T. Anderson, and S. L. Halverson
        Nucl. Appl. Technol. 10, 76-84 (Jan 1971)

A Modified Target Current Display System for the Electron Probe
Microanalyzer
    J. E. Sanecki and D. R. O'Boyle
        Rev. Sci. Instr. 41, 1621-1622 (Nov 1970)

The Role of Theory in Eddy Current Testing
    Donald L. Waidelich
        Mater. Eval. 28, 262-266 (Dec 1970)

III. NUCLEAR SAFETY

A. LMFBR Safety

1. Accident Analysis and Safety Evaluation (G. J. Fischer) (189a 02-112)

    a. Initiating Accident Code Development (F. E. Dunn)

        Last Reported: ANL-7742, pp. 132-133 (Sept 1970).

        (i) Incorporation of Slug-ejection Coolant Model into SAS1A Code. Coolant voiding results have been obtained for a flow-coastdown accident in the FFTF using the previously described multiple-bubble slug-ejection coolant voiding routine in SAS1A. A series of calculations were made using different values for the superheat and for the initial thickness of the liquid-coolant film left on the cladding and structure when voiding occurs. The superheat was varied from 0 to 70°C, and the initial film thickness was varied from 0.015 to 0.03 cm.

        Figure III.A.1 shows some of the results for the initial phase of voiding for 30°C superheat with an initial film thickness of 0.03 cm.
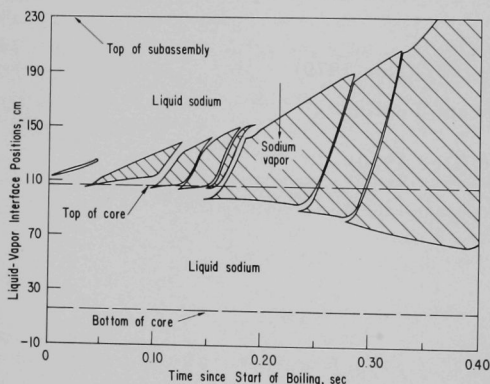

Fig. III.A.1

Sodium-voiding Dynamics during Initial Phase. Coastdown conditions, no fission-product gas.

        The initial vapor bubble is formed near the top of the fuel. The initial momentum of the coolant carries the first bubble upward into the cooler reflector and fission-gas plenum regions. A second vapor bubble is formed below the first one, creating an intermediate liquid slug between the two vapor bubbles. The vapor pressure in the lower vapor bubble exceeds that in the upper bubble, so the intermediate liquid slug is accelerated upward until the upper bubble collapses.

        The coolant continues to heat up, forming new vapor bubbles further into the core and expanding the size of the vapor region. The lower

liquid column is driven downward by the vapor pressure. Eventually, 0.36 sec after the start of boiling, the upper liquid slug is blown out of the top of the subassembly, and the vapor pressure is dropped to the pressure of the upper coolant plenum.

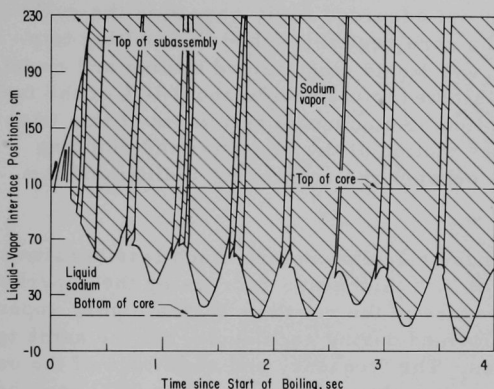Figure III.A.2 shows some of the details of the later stages of voiding. After the upper liquid slug is blown out the top, the momentum of the lower liquid slug carries it downward initially. Because of the depressurization of the voided region, the lower liquid slug eventually reverses flow when the core is about half voided, and the lower liquid slug starts to reenter the voided region. The main force driving the reentry is the gravity head due to the weight of the displaced liquid sodium.

Fig. III.A.2. Sodium-voiding Dynamics during Later Stages. Coastdown conditions, no fission-product gas.

As the lower liquid slug reenters the hot upper part of the core, the liquid is heated until vaporization occurs. Then vapor bubbles are formed and liquid slugs are driven up the channel. The pressure in the vapor bubbles eventually reverses the flow in the lower liquid slug and drives it downward again. Boiling then stops for a while, both because the hottest liquid has boiled off and because the lower liquid slug moves down into cooler regions near the bottom of the core. Depressurization of the channel again leads to flow reversal and reentry of the lower liquid slug to start the cycle again.

The lower liquid slug continues to oscillate. The general trend is for each oscillation to void more of the core than the previous one.

The routine calculates the thickness of the liquid-sodium film left on the cladding after voiding occurs, accounting for both vaporization and condensation. With an initial film thickness of 0.03 cm, film dryout in the middle and upper parts of the core occurs only for short times during the reentry phase of the later cycles just before the lower liquid slug starts boiling. Boiling in the lower liquid slug sends small liquid slugs up the channel, and the liquid slugs are assumed to rewet the cladding to its initial film thickness.

As long as the cladding is wetted, heat removal by vaporization of the liquid film holds the cladding temperature down to the range of

950-1000°C. Because film dryout only occurred for short intervals in the 0.03-cm initial-film-thickness case, the cladding temperature did not exceed 1100°C at any point, even after 4 sec of voiding.

The consequences of the accident depend strongly on the initial film thickness. When the initial film thickness was cut from 0.03 to 0.015 cm, film dryout occurred earlier and lasted longer. About 2 sec after the start of boiling, film dryout occurred early enough in the cycle so that the cladding in much of the core region reached the melting temperature before the reentering lower liquid slug started boiling and rewet the cladding. When the cladding started to melt, only about 10% of the fuel at the middle of the core was molten. An adequate treatment of this case would require consideration of the motion of the fuel after the cladding melts, as well as the interaction between the reentering sodium and the fuel and molten cladding.

The results of these calculations are much less sensitive to the superheat than to the initial film thickness. Increasing the superheat from 30 to 70°C made little difference in the results. With a higher superheat, fewer vapor bubbles were formed during each cycle, but the same type of cyclical behavior was observed. The frequency and amplitude of the oscillations of the lower liquid slug were about the same in the 70°C case as in the 30°C case, and the film dryout results were about the same.

Reducing the superheat to zero had more effect than increasing it to 70°C. With no superheat, many more vapor bubbles were formed in each oscillation and the period of the oscillations was reduced about 30%. The shorter period resulted in less film dryout. Even with the 0.015-cm initial film thickness, cladding melting did not occur in 2.5 sec of boiling.

These results are only preliminary, but they indicate the type of results to be expected from this model. A number of aspects of the model still need to be investigated. At present, the vapor pressure in a given vapor bubble is assumed to be spatially uniform, although different vapor bubbles can have different pressures. The high vapor flow rates that can occur, especially after the upper liquid slug has been blown out and the voided region has depressurized, might cause a significant pressure variation due to friction. This aspect is being investigated.

b. Analysis of Fuel Behavior (A. M. Judd)

(i) Analysis of Fuel Behavior up to Gross Cladding Failure

Last Reported: ANL-7737, pp. 152-153 (Aug 1970).

The new fuel-deformation module, TSDEF, for the SAS code is nearing completion. One of the main problems of the numerical treatment

was to find a method of calculating the plastic deformation, and especially the transition from elastic to plastic deformation, which was stable and needed only a few iterations. This has been accomplished, as shown in Fig. III.A.3, which shows the equivalent stress and strain at the inner surface of the fuel (i.e., the surface of the central void) as it is subjected to a temperature transient. The details of the calculation (dimensions, temperatures, etc.) are not supposed to represent a real reactor situation, but were chosen to make a severe test of the algorithm. In addition, a strongly temperature-dependent yield surface was used, for the same reason.

The points on the curve represent time steps in the calculation. From an initial stress-free (and strain-free) state, up to Step 7, the strain is elastic, while Steps 8 to 12 involve plastic strain. The algorithm is such that, in the plastic regime, at most four iterations were required for convergence.
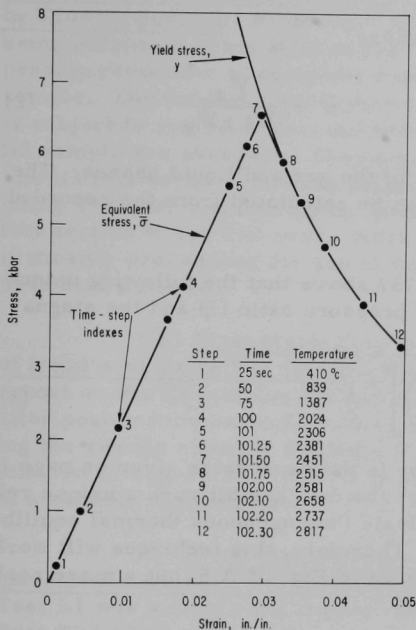
2. Coolant Dynamics (H. K. Fauske)
(189a 02-114)

a. Liquid-Vapor Dynamics (M. A. Grolmes and H. K. Fauske)

Last Reported: ANL-7737, pp. 154-155 (Aug 1970).

Step	Time	Temperature
1	25 sec	410 °C
2	50	839
3	75	1387
4	100	2024
5	101	2306
6	101.25	2381
7	101.50	2451
8	101.75	2515
9	102.00	2581
10	102.10	2658
11	102.20	2737
12	102.30	2817

Fig. III.A.3. Transition from Elastic to Plastic Deformation

(i) Acoustic Detection of Entrained Gas. In ANL-7737, a two-phase, choked-nozzle gas-detection technique was proposed and a preliminary analysis was presented to illustrate the feasibility of the method. The sensitivity and simplicity of the technique make it attractive as a gas detector on current liquid-metal experimental facilities.

To investigate the experimental difficulties associated with the nozzle and also to study the applicability of the preliminary analysis, the nozzle shown in Fig. III.A.4 was constructed of Lucite. A two-phase mixture, obtained by injecting gaseous nitrogen into water, was accelerated through the nozzle, and the stagnation and throat pressures (P_0 and P_t, respectively) were recorded along with the stagnation temperature (T_0) and the liquid and gas flow rates (W_ℓ and W_g). For homogeneous flows
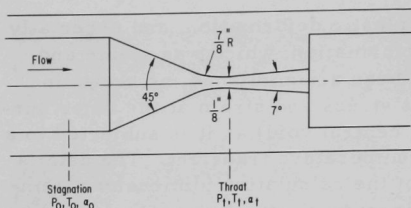
Fig. III.A.4. Lucite Nozzle for Tests to Study Acoustic Detection of Entrained Gas

(velocities of the phases are equal), the stagnation void fraction (α_0) can be expressed as

$$\alpha_0 = \frac{xv_{g0}}{(1-x)\,v_\ell + xv_{g0}}, \quad (1)$$

where

$$x = \frac{W_g}{W_\ell + W_g} \quad (2)$$

and v_{g0} and v_ℓ are the specific volumes of the gas and liquid phases. The homogeneous stagnation void fraction can be calculated from the recorded parameters.

The analysis in ANL-7737 shows that the following unique relationship exists between the critical pressure ratio (η) and the stagnation void fraction:

$$\ln \eta = \frac{1-\alpha_0}{\alpha_0}\left[(1-2\eta) - \frac{\eta^2}{2}\left(\frac{1-\alpha_0}{\alpha_0}\right)\right] - \frac{1}{2}. \quad (3)$$

(Note that there is a typographical error in the expression given on page 155 of ANL-7737.) Figure III.A.5 shows that the data exhibit such a unique relationship; however, the preliminary analysis (homogeneous thermal equilibrium) does not agree with the results. Therefore, this technique will work quite well in the void-fraction range shown in Fig. III.A.5, but a more realistic mathematical description is needed.

Fig. III.A.5

Relationship between Critical Pressure Ratio and Stagnation Void Fraction
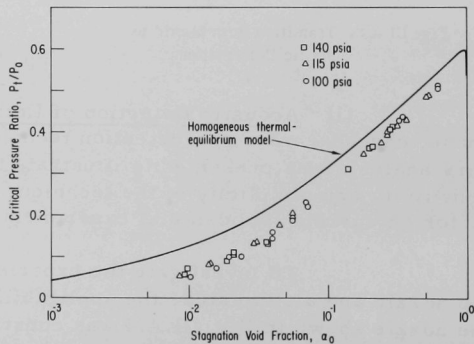
3. Fuel Dynamics Studies in TREAT (C. E. Dickerman) (189a 02-117)

a. Transient In-pile Tests with Ceramic Fuel (C. E. Dickerman)

Last Reported: ANL-7758, pp. 101-110 (Nov 1970).

(i) <u>High-specific-energy Mark-II-loop Checkout Test (E2) on Fuel Movement during a Power Excursion.</u> A limited-distribution report summarizing the results of Tests E1 and E2 is being prepared.

(ii) <u>First Two Mark-II-loop Tests (H1 and H2) on Transient Failure Threshold of Mixed-oxide Fuel Element with Axial Heat Transport by Flowing Sodium.</u> A limited-distribution Division report on Test H1 is being prepared; completion of the final report on Test H1 has been delayed pending resolution of questions raised by the postmortem inspection of the sample. The limited-distribution report on Test H2 has been finished; it is subject to revision when the results of the posttest examination of the H2 sample are available. Shipping-permit questions have been clarified. The H2 test section has been shipped to the hot laboratories using the existing T-2 cask and a shipping liner built for use in shipping a Mark-II-loop test section in the T-2 cask. Work will begin on the test section as soon as criticality procedures for use of the Mark-II loop glovebox for the sample have been satisfied.

(iii) <u>First Mark-II-loop Tests (E3) on Fuel-movement Failure of Irradiated Oxide Pin during a Power Excursion.</u> A limited-distribution report on the E3 test has been prepared; this report is subject to revision after postmortem examinations of the sample remains. The loop containing the sample remains (believed to be extensively fragmented and distributed throughout the loop) is in storage at TREAT pending availability of a suitable shipping cask.

(iv) <u>First Mark-II-loop Experiments (L1 and L2) on Fuel-movement Failure of Unirradiated Fuel during a Loss-of-flow Accident.</u> Test L1 was a single-pin loss-of-flow simulation experiment. It was the first TREAT-loop flat-top test simulating a loss-of-flow incident. The results are being analyzed to guide planning of the first loss-of-flow loop simulation with a cluster of pins. The data obtained from the three L1 flat-top transients (1336, 1337, and 1338) have been plotted and are being analyzed.

The objective of approaching but not crossing the threshold of cladding integrity by reducing sodium flow was attained. The lowest sodium velocity was 1.35 m/sec for 14 sec. The shape of the power transient was roughly the same in all three transients. The nominal flat-top power was about 21 MW, and the reactor was scrammed to give 305 MW-sec in each transient.

The three transients had certain phenomena in common. First, the sodium flow as measured by both the inlet and exit electromagnetic flowmeters was the same (within a few percent) at the beginning and end of each transient, but during the transient there were large fluctuations in flow. In each test, the lower or inlet flowmeter showed a sharp

drop to a low-level value during the power pulse; the top, or exit flowmeter, showed flow fluctuations that damped out about 5 sec after the transient. Second, during the transient, the thermocouple alongside the fuel pin and about 2.5 cm below its top end always read higher than the thermocouple measuring the bulk sodium temperature leaving the test section. The temperature fluctuated during the transient, reaching a peak near the end of the transient, which then rapidly damped out. The thermocouple measuring the inlet bulk temperature did not oscillate and rose smoothly a few degrees during each transient. Third, heat balances based on the flow (as measured by the inlet flowmeter and on the temperature difference between the inlet and outlet bulk sodium) are reasonable, agreeing within about 10%.

The radiograph of the L1 pin before the tests showed it to be straight, centered, and with no gaps between oxide pellets. After the tests, the L1 pin was warped and there was a gap between the top pellet and the column of pellets, indicating that the column had expanded appreciably.

The bulk-sodium velocity of 1.35 m/sec along the L1 pin did not cause it to fail in any respect, but the pin obviously became hot enough to warp and cause the 34.44-cm column of oxide pellets to separate.

We are investigating the cause of the oscillations in flow and temperature, and the difference between the thermocouples and flowmeters that occurred at the initiation of the transient and damped out a few seconds after TREAT was scrammed.

It appears from the oscillatory nature of the flow and temperatures that there is some film boiling on the cladding. Provisionally, this is all related to the vicinity of the spacer wire, which touched the single-channel flow tube in a line contact.

(v) First Mark-II-loop Experiments (E4 and E5) on Fuel-movement Failure of Mixed-oxide Fuel during a Power-excursion Accident. The E4 transient experiment on a prototypical FFTF mixed-oxide fuel element was performed on November 17th. The preexperiment specification called for an integrated TREAT power of 545 MW-sec to provide an estimated 1800 J/g of oxide total energy in the fuel pin. With a sodium coolant flowrate of 4 m/sec, this was sufficient input energy to go significantly past the failure threshold.

Preliminary data from the experiment indicate that the energy input specification was satisfactorily met by a value of approximately 2050 J/g and the initial flowrates were close to 4 m/sec. A peak reactor power of 2500 MW was reached at a relative clock time of 1.89 sec, and failure events began at 1.95 sec (estimated 1420 J/g). Some 15 msec later, evidence of violent failure occurred. Both the outlet-flow and fuel-pin-temperature data channels became saturated at full scale. The outlet-pressure

data show a 1-msec spike of about 300 psi; 3 msec later these effects were seen at the inlet, where the flow rapidly reverses to -20 m/sec and a series of three pressure spikes (300, 500, and 200 psi) occur at about 1.5-msec intervals. At about 1.99 sec relative time, a series of pressure pulses spaced about 25 msec apart occurred at the outlet and at relative time 2.04 sec. A similar series of somewhat wider but smaller-amplitude pulses spaced about 3 msec apart were observed at the inlet. In this test, the full width of the reactor power transient was 400 msec and the time-integrated power up to relative time of 2.10 sec (when most of the action was over) was 600 MW-sec (estimated 1980 J/g total input energy to fuel pin). Further detailed analysis of the data will be performed by further study of the information on the magnetic tape.

A comparison of pre- and posttest neutron radiographs indicates substantial fuel movement with extensive melting and slumping in the lower regions of the fuel pin. Both radiographs were taken with the B_6Si loop thermal-neutron sleeve in place, so estimates of approximate quantities of fuel movement are difficult.

(vi) First Mark-II-loop Experiments (D1 and D2) on Effects of Release of a Small Amount of Molten Fuel, Using Pins with Local High-enrichment Sections. A power-calibration run for experiment D1 was conducted in TREAT on November 20, using a seven-pin cluster in the prototype Mark-II loop. Radiochemical and gamma-counting analyses of the pellets from three of the seven pins, and of foils attached to the outside of the pins, have been completed. Preliminary analysis of the data indicates that the power distribution in the cluster is in good agreement with SNARG-2D calculations. The power-calibration factor appears to be about 15% higher than calculated. Further results will be reported when analysis of the data is completed.

Fabrication of two test sections for seven-pin clusters is nearly complete. One of these test sections will be used for Test D1; the other will be used for backup and development of remote assembly tooling and techniques.

b.   Experimental Support (L. E. Robinson)

Last Reported: ANL-7753, pp. 151-152 (Oct 1970).

(i) Cask Fabrication. AEC certification of the cask design was supplied by the Chicago Operations Office, procurement was authorized, the Department of Transportation Permit No. 6345 was issued, and a vendor order was placed for fabrication of two Mark-II-loop shipping casks. The UF_4 required is scheduled to be sent to the vendor in two shipments during the latter half of December. Some long-lead-time steel items are on hand; the remainder are on order by the vendor. The detailed vendor

quality control plan is scheduled to be available by January 10 for review and approval. Scheduled delivery of the first cask is May 1971, the second following about two months later.

(ii) Preparation of Last Six Mark-II Loops from FY 1970 Stocks. The six Mark-II loops to be constructed from FY 1970 stocks are loops A1 through A6. A1 has been completely outfitted and run in preliminary tests in preparation for the high-pressure loop prooftest at design temperature. Difficulty was encountered during this test with the valves of the loop fill and overflow lines. These valves are mechanical remotely-operated valves that back up the freeze plugs in these two lines; the valves were primarily intended for operations with preirradiated samples and are not required for the next loop test, D1. Accordingly, to minimize schedule delays, the mechanical valves are to be cut out, and high-pressure closure fittings are to be welded in their places using the same techniques used previously for the closures on the prototype loop. The A2 pump has been delivered and installed in the A2 loop. Outfitting will proceed on this loop as progress on the A1 loop permits.

The A3 loop-body weldment was successfully heat-treated; shop assembly is under way. The A4 loop-body weldment will be heat-treated soon.

(iii) Preparation of Handling Equipment for Routine Alpha-cave Operations on Mark-II Loops. Two items are being fabricated: a transfer port and a table to support the loop in the unloading position while it is attached to the transfer port. They will be installed on an FEF argon glovebox to permit the handling of Mark-II sodium loops at that facility.

c. Analytical Support (A. B. Rothman)

Last Reported: ANL-7758, pp. 110-116 (Nov 1970).

(i) TREAT Converter for Future Tests on Clusters of Mixed-oxide LMFBR Fuel. Over a period of time, work was done on preliminary design and on performance analyses of a fast-neutron converter for use in TREAT experiments on clusters of mixed-oxide fuel pins. For a cluster of seven highly enriched prototypical mixed-oxide fuel pins, such a converter would provide an improvement over a thermal-neutron flux filter in both radial power profile and ratio of sample centerline power to TREAT power. For a cluster of 19 pins, the converter appears to be necessary. A limited-distribution report describing this preliminary work is being modified for issuance as a topical report. Future effort on the converter will be carried out under TREAT Improvement Studies (189a 02-197).

4. Fuel-Coolant Interactions (R. W. Wright) (189a 02-164)

a.   In-pile Simulation Tests: Pressure and Work Energy
(J. J. Barghusen)

Last Reported: ANL-7753, pp. 158-159 (Oct 1970).

(i) Medium-energy Power-excursion Experiment with UO_2
Pins in FFTF Simulation (S6). Test S6, the initial piston-autoclave test
using a seven-pin wire-wrap fuel bundle in simulation of FFTF geometry,
was performed in TREAT with a transient equivalent to a total average
fission-energy input to the fuel of about 493 cal/g of UO_2. The fuel-pin
configuration was described in ANL-7753. The outer six pins in the seven-
pin array contained 10%-enriched UO_2; the center pin contained 13%-
enriched UO_2 to compensate for the average flux depression in the center
pin (that it compensated was confirmed in a calibration test). This was
the first of the S-series TREAT tests in which the neutron hodoscope
was used.

The power-excursion test resulted in the complete destruc-
tion of all the fuel pins, as determined by neutron radiography of the auto-
clave after the test. The radiographs also showed the presence of fragmented
oxide fuel in the piston cavity. Preliminary analysis of the pressure-
response data indicates that three separate sets of pulses occurred during
the experiment. The first set contained six pulses. The initial pulse in
this set occurred at about 69 msec after peak power at a fission-energy
input of 383 cal/g of UO_2; the amplitude of the largest pulse in this set of
pulses was 1900 psi. The second set consisted of three small pulses; the
amplitude of the largest pulse was 180 psi. The third set of pulses con-
sisted of 19 pulses in a train of damped oscillations. The amplitude of the
largest pulse in this set was 2170 psi. The neutron-hodoscope results are
not yet available. Analysis of the data is proceeding.

B. Operations

1. TREAT Operations (J. F. Boland) (189a 02-122)

Last Reported: ANL-7758, pp. 123-124 (Nov 1970).

a.   Operations

Experiment HEDL-PNL-1-8, containing a fuel element pre-
viously irradiated in EBR-II, was subjected to a transient irradiation de-
signed to cause incipient melting of the annular fuel pellets.

Experiment RAS S-6, containing a seven-pin cluster of stainless
steel-clad UO_2 fuel rods, was subjected to a transient irradiation that caused

extensive failure of the fuel rods. This experiment received an energy release similar to experiment S-5 and was designed to investigate effects of changing from a five-pin cluster without spacer wires to a seven-pin cluster with spacer wires.

Neutron radiographs were made of EBR-II driver fuel, meltwire-temperature indicators, and experimental capsules from Subassembly XX01. Neutron radiographs were also made of TREAT experiments RAS S-6 and HEDL-PNL-1-8. Two groups of irradiation samples were neutron-radiographed for INC.

Last month, one of the two reactor-cooling-system compressors developed a noisy bearing and was overhauled; this month, the other compressor developed a noisy bearing and was removed from service while the bearings were replaced, the motor reconditioned, and the impellers dynamically balanced. Reactor operations were continued using the compressor that had been reconditioned last month.

(i) Automatic Power Level Control System. Installation and testing of the automatic control system are still awaiting AEC approval for operation with digital-computer control.

PUBLICATIONS

Effects of Thermal Discharges on the Mass/Energy Balance of Lake Michigan
  J. G. Asbury
    ANL/ES-1 (July 1970)

Equation of State for Fast Reactor Safety Studies. Part 1. Theoretical Relations
  D. Miller
    Nucl. Safety $\underline{11}$(6), 450-463 (Nov-Dec 1970)

An Experimental Demonstration of Inert Gas Effects upon the Incipient Pool Boiling of Sodium
  R. M. Singer
    Nucl. Sci. Eng. $\underline{42}$, 427-428 (Dec 1970)

PUBLICATION--General

Guidelines for Sodium Fire Prevention, Detection, and Control: Report of the Ad Hoc Committee on Sodium Fires
  D. W. Cissel, L. F. Coleman, F. O. Pancner, F. A. Smith, and
  A. D. Tevebaugh
    ANL-7691 (June 1970)

X

B